UNIVERSIDAD COMPLUTENSE DE MADRID

FACULTAD DE CIENCIAS FÍSICAS

TESIS DOCTORAL

Studies beyond the neutron dripline using quasifree (p,2p) reactions: the case of ^{13}Be

Estudios más allá de la línea de goteo de neutrones usando reacciones (p,2p) cuasi-libres: el caso del ^{13}Be

MEMORIA PARA OPTAR AL GRADO DE DOCTOR

PRESENTADA POR

Guillermo Ribeiro Jiménez

Directores

Olof Tengblad
Enrique Nacher González

Madrid, 2015

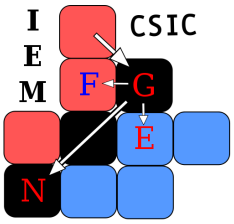

Grupo de Física
Nuclear Experimental

Studies beyond the neutron dripline using Quasifree (p,2p) reactions: The case of ^{13}Be

Estudios más allá de la línea de goteo de neutrones usando reacciones (p,2p) cuasi-libres: El caso del ^{13}Be

Guillermo Ribeiro Jiménez

TESIS PRESENTADA PARA LA OBTENCIÓN DEL
TÍTULO DE DOCTOR EN FÍSICA POR LA U.C.M.

Mayo 2015

Directores:

Profesor Olof Tengblad
Instituto de Estructura de la Materia(CSIC)

Doctor Enrique Nácher González
Instituto de Estructura de la Materia(CSIC)

A mis padres, Jose y Rocío.

Contents

List of Figures

List of Tables

Acknowledgements/Agradecimientos

Son las 3 de la madrugada del día 4 de Mayo de 2015, apunto la fecha porque estoy seguro de que querré recordarla, hoy a una hora razonable, entrego *la tesis*. Parece que fue ayer cuando entré en el grupo de Física Nuclear Experimental del IEM-CSIC, pero no, he estado trabajando ahí desde el 1 de Septiembre de 2010, es decir, casi cinco años. Este texto es la conclusión de varios años de trabajo, aprendizaje, buenos y malos ratos, cambios y muchos viajes. Muy poco de lo que ha sido este tiempo está realmente condensando en este documento, sólo se refleja una parte. De entre todas las cosas que se podrían quedar fuera hay una en concreto que no debe hacerlo: Las personas que me han ayudado, que son muchas. Que menos que dedicar un rato a agradecerlo.

It is 3 in the morning of May 4, 2015, I write down the date because I am sure I will want to remember, today at a reasonable hour, I am handing in *the thesis*. It seems like yesterday when I started at the group of Experimental Nuclear Physics IEM-CSIC, but I have been working there since September 1, 2010, almost five years. This text is the conclusion of several years of work, learning, good and bad times, changes, and many travels. Very little of what has been this time is actually condensed in this document, only a portion is reflected. Of all the things that could be left out there is one in particular that should not: People who have helped me, which are many. This is time to be grateful.

La primera persona a la que tengo que agradecerle su contribución, es sin duda, mi director de tesis, Olof Tengblad. Desde el momento en que me escogiste para la beca FPI, hasta el último e-mail con correcciones sobre la tesis (aunque siempre sean parcos en palabras), por todas la discusiones que acaban bien y por supuesto por toda la oportunidad, los consejos y las historias. También estoy muy agradecido a María Jose y a Andrea, por ayudarme siempre que lo he necesitado.

Por supuesto, una de las mejores cosas que me han dado estos años en la física nuclear es conocer a los que han sido todos mis compañeros en el grupo, ahora amigos, sin los que estos años valdrían bastante menos.

A Kike, por haber sido un amigo además de un director de tesis, por responder siempre a cualquier problema y poder hablar contigo de cualquier cosa. A Mariano, por toda la ayuda que has sido, tanto en lo personal como en lo profesional, por las gilipolleces que me dijiste el día de la fiesta de la cerveza y por supuesto, por las discusiones, tan inacabales como inmejorables. A Vicente, por hablar de todo y no cortarte un pelo (sobretodo del bigote) y por las discusiones inmejorables (pero acabables). A Briz, por el buen rollo SIEMPRE y por los triples. A Andrés, por todo el azúcar, por ayudar siempre que puede y por Gallagher y Jäckel. A Jose, por ser el primero en echarme una mano ahí en GSI en 2010, por que una noche (o un día) contigo es una montaña rusa y por que pidas los cafés. A Riccardo, por ser la alegría del grupo durante mucho tiempo y por supuesto también por las discusiones. A Alejandro porque parece que llevas con nosotros desde que empecé y eso es dificil. A Jan, por aguantar nuestras discusiones en castellano y ser siempre un gran tio. A Ángel, por todas las discusiones en los viaje, impagables y tener siempre otro punto de vista. A Mario, por aquel ron en tu casa, por tu vehemencia y por estar algo en la parra. A Irene, por venir con tanta energía. A Jorge, por los FIFA y haberme acogido siempre genial en Darmstadt. A Ana, porque fue una pena que sólo estuvieras un año aquí, por el buenisimo tequila que nos diste, y por el experimento del CERN, que en el fondo lo pasamos bien. A Carlos y a Ricardo, por ser los primeros en echarme una mano en todo cuando entré en el grupo.

These last years have involved a lot of traveling and people from GSI, Santiago, Chalmers, AArhus and plenty of other places have been a major support, help and fun in this years.

I have to be very grateful to the people of Chalmers and Göteborg which spent their time helping me in my first long-time staying abroad. Anna for helping so much with the renting and living, Björn, Goran, Ronja and Andreas for their help with the physics, Hakan for the same and the pizzas and specially Thomas for everything. I would also like to say thank you to Jim, for all the talks and beers.

I also spent three intense months at GSI, Darmstadt. There were so many people that I will forget some of them for sure, thank you all in advance. First I have to say thank you to Tom, Konstanze and Haik, for always helping a lot when I have been able to find them, to Ralf, for the same and answering my annoying e-mails, to Valerii for the travels, the beers, the discussions and the strange Ukrainian tale that you told me at Dresden, to Igor for the beers and the talks, to all the other guys like Christoph, Felix, Alina, Leyla, Dominic, Togano or Sebastian for the coffees and all the good times. I have to specially be grateful to my office mates at GSI for welcoming me so easily, being friends and for the gummy bears, thanks Phillip for the fun, the discussions and being with me in the cave my first month there, thanks Marcel for all the trips, the strange stories and the barbecues, thanks Matthias for ALWAYS helping , the fun and for always have good conversations. I cannot avoid to mention my Steinhaus colleague those months, Antonio, for all the fun.

There is also a lot of people from the R3B Collaboration that I have to mention here. Like before I will probably forget a lot of them, I am sorry, not be mad to me! This work would have been very much harder without Paloma, which helped more than anyone when I started, thank you for that and for all the other talks(Dexter obviously) and good times. Thanks to Magdalena for all the time at Darmstadt, trying to help each other and having fun. Thanks to Tobi for the beers and thanks to Lola, Hector, Dani, Matthew, Simon, Ana and Paulo for always being nice and helpful.

From Aarhus I have to be specially grateful to Karsten, for taking very seriously helping, the jokes and all the interesting discussions. Thanks to Oliver,Jonas, Gunvor, Kasper, Morten, Hans, Oleksandr, Aksel and Dmitry for discussions, beers, and all my time there.

There are other people from elsewhere that I also need to mention without any special order. AJ for the really good time and beers at Berkeley, Diego for being tireless at Zakopane. I have to give very special thanks to Nara Singh for being always so nice and helpful with me. Thank you to Franco for the great times in Madrid. To Carlos for the good time at Italy. A Bruno, Jacobo y Lay, por todos los buenos ratos.

Hay mucha gente de Madrid (bueno, muchos ya no), a los que quiero agradecer por estos años de apoyo, diversión y de aguantarme.

Quiero empezar agradeciendo su contribución a mis tres compañeros *originales* de piso y amigos, puesto que no puedo separar mis inicios en la física nuclear con entrar con ellos en La Mansión en Diciembre 2011. Gracias a los tres por animaros a dar el salto. Gracias a Álvaro, por intentar ser comprensivo, por salir de la ducha y por el viaje a EEUU, increible. Gracias a Pablo por los 2K, por los FIFA y sobretodo porque gracias a la casa volvemos a ser muy buenos amigos. Gracias a Toni por aguantarme cosas, por no morirse por su intestino, por el viaje a Alemania y por las cervezas siempre.

Los compañeros de piso se han cambiado por otros y ya hace más de un año de eso! Muchas gracias a los dos por imponer las cenas comunes, de lo mejor que le ha pasado al piso. A Alvarito por haber estado siempre disponible, por los juegos a medias, por que hay pan con hostias y queda poco pan, por tantos años. A Tati por animar el cotarro, por intentar ser siempre la alegria en el día a día, que al menos para mi, es imposible, por la fruta gratis y sobretodo por las inexistentes paellas.

A Rorro, por ser amigo desde siempre en todas partes, por haber estado cuando lo he necesitado, por todas las charlas de absolutamente cualquier cosa, por la ansiedad y por que viajes algo menos y nos veamos más. A Javi, por todos los años de la carrera y muchos más, por venir a Gothenburg y a Suiza, por ser comprensivo, por las discusiones y por los personajes chungos de rol. A Gabo, porque montamos un equipo juntos, por dejarme participar tanto en la boda(y a Haizea), que fue genial, por que aunque hablemos poco, al final sacamos un rato. A Edu por hablar de cosas raras, porque cuando vienes parece que no ha pasado el tiempo, por la ayuda con la fisica hace años y mira ahora y porque feliz navidad. A Toño por el oso maloso, por acogerme en San Francisco y porque le he echado mucho de menos estos años. A Paula porque se duerme y haberme ayudado siempre que se lo he pedido. A Susana porque siempre quiere salir y que la liemos y porque estemos de acuerdo a donde. A Inés por el cariño y por llegar tarde. A Lara por que quiero verla más días que en nuestro cumple. A Javi por la gran acogida en Londres y por los años buenos incluso antes de que yo llegase a Pozuelo.

A María, porque siempre ha estado ahí a pesar de todo, por la sal, los buenos ratos y el teatro. A Santi y Auro porque es dificil separarlos, por Sherlock Holmes, por la comida India, por las charlas en serio y por el oso panda que me ha acompañado en este ultimo tramo de escritura. A Emilio por haberme echado una mano a retomar el rol, por los cochinillos y por las charlas molonas. A Isa por ser inescrutable y por lo del CERN. A Artemi y a Ali por tantos años.

A Jorge-Cels, por los geniales emails largos derrepente y por hablar más.

No quiero olvidarme de agradecer la contribución de Javier Coronas, Javier Cansado y Pepe Colubi que con mi reciente descubrimiento de *Ilustres Ignorantes* me han acompañado estos últimos meses de encierro y escritura.

This is a thesis about Nuclear physics, therefore I would like to say thank you to Alexei Ananenko, Valeri Bezpalov and Boris Baranov. They gave it all, to thank from here is the least I can do.

A la cafeína, que sin ella tampoco habría podido acabar.

Por supuesto tengo que acabar dando las gracias a toda mi familia, que siempre ha estado conmigo estos años. A mi padre, Jose, por venir siempre a comer al VIPS durante casi cinco años, por ser tan generoso y por enseñarme a ser tan crítico. A mi madre,Rocío, por comprenderme, por todo el cariño y por haber confiado siempre en mi. A Ana y a Luis, por tantas cosas, por las charlas, por el apoyo continuo que tanto se nota y por la comida genial,claro. A Marisa por que siempre me ha apoyado, a David y Julie (y Lea) por esperarme siempre con los brazos abiertos, a los cuatro por el recibimiento en Bruselas en 2012 y por vernos más. A Claire, por las peleas de antaño, por el buen rollo, porque siento mucho no haber ido a Granada y también por vernos más. A Álvaro Y Mariluz, por la ensalada de salsa rosa, por el día 6 de Enero que montáis en vuestra casa y siempre por el afecto . A Julía, María, Inés y Sara, porque ya ninguna sois mis primas pequeñas, por el video, por el buen rollo y para/por lo que queráis. A Ricardo y Paula, por las enormes cenas en su casa, por la moneda esa que me quede y de la que todavia me acuerdo y por todo el afecto. A Chity y Carmen, por los regalos geniales, y por toda la ayuda cuando la he necesitado.

Sólo me queda una persona por agradecer, Natalia, gracias por todo, por la ayuda con algunos dibujos, por las comidas y cenas que he necesitado, por llevarme en coche, por tanta comprensión, por los silencios, por despreocuparme y por preocuparme y por todo el cariño día a día.

Por último, todo este trabajo no habría sido posible sin la ayuda y la necesaria financiación y apoyo del Ministerio de Ciencia e Innovación así como el Ministerio de Economía a través de los proyectos FPA2009-07387 y FPA2012-32443, asi como la beca FPI que disfruté entre Septiembre 2010 y Agosto 2014 BES-2010-042262.

"- Algebra forces your mind to solve problems logically. It's one of the only perfect sciences...
- You think the world runs on logic? Come on. Open your eyes"
1x07 Brotherhood, Six Feet Under

1 Introduction

1.1 The Nuclear Physics through a telescope

In the late nineteenth century scientists were looking for new elements to add to the 83 at this time known; 50 of these had only been found in the last hundred years [1]. The atom was defined as the most basic form of matter and every element was regarded as a completely different particle. The elements were classified just following their atomic mass, but Dmitri Mendeleev (1834-1907) noted that certain chemical properties emerged with fixed periodicity which led him to postulate the periodic table in his textbook Principles of Chemistry (1869). In 1815 William Prout (1785-1850) has published the hypothesis that all the atomic weights were integer multiple of the Hydrogen weight, considering it as the basic compound of all the elements. Despite the fact that this idea was very close to reality, it was wrongly discarded as soon as it was obvious that several atoms did not follow that trend. The atom was considered as a particle impossible to break or divide.

The discovery of radioactivity revealed that atoms were not just a simple particle but they were compound of several smaller pieces. In November 1895 Wilhelm Conrad Röntgen discovered the X-rays as a result of the fluorescence produced by cathode rays in a cathode ray tube. Henri Becquerel (1852 - 1908) heard about these results in a conference, and wondered if luminescence was a precondition for the observation of X-rays. He performed several experiments illuminating Uranium salts with sunlight causing the material to glow by phosphorescence, but he ends up realizing that Uranium emits certain rays with similar penetration power to the X-rays naturally without previous exposure to sunlight. This conclusion is the discovery of radioactivity by Becquerel in 1896. Marie Skłodowska-Curie (1867 - 1934) and her husband Pierre Curie (1859 - 1906) thought that these rays might be coming from a new element within the Uranium salts different from the compounds Thorium and Uranium. As a result of their work to isolate the source of the rays they discovered two new elements: Polonium and Radium.

Whom would become the father of Nuclear Physics was Ernest Rutherford (1871-1937), he was working at McGill University in Montreal (Canada) when he discovered the alpha (α) and beta (β) radiation [2]. The rays emitted by the Uranium salts had different penetration powers, thus working with different materials to measure the penetration as well as with magnetic fields in order to bend them, led him to discover the difference between two types of rays to which he assigned the Greek letters α and β in 1899. Almost at the same time, Paul Villard (1860-1934) at France studied the emitted radiation from Radium, a different kind of radioactivity more powerful that ended up named by Rutherford in 1903 [3] as gamma (γ) rays. Years later in 1908, Rutherford in collaboration with Thomas Royds (1884-1955) at Manchester (United Kingdom) found that the alpha particles were indeed helium nuclei [4].

In 1901 William Thomson, Lord Kelvin (1824-1907) proposed the first model of the atom structure. It was known as the "Plum pudding model" because it consists in a sphere of positive charge with the electrons embedded like plums in a pudding, where the total charge was cancel out (see figure 1.1). The model was improved by J.J Thomson (1856-1940) in 1904, making the electrons move in concentric circles in the sphere.

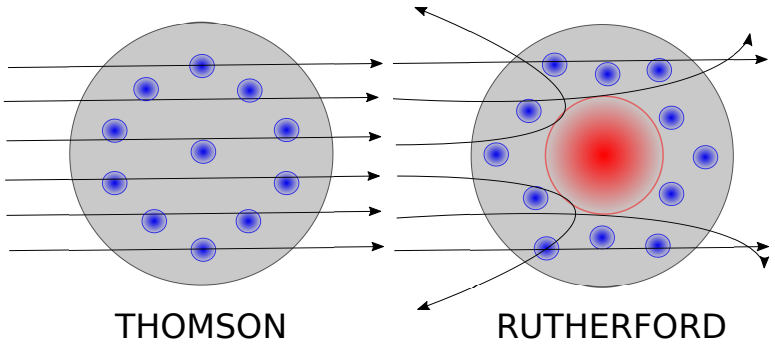

Figure 1.1: Basic atom model schemes with their expected behaviour against the Geiger and Marsden experiment. *Left:* The "Plum pudding model" of Thomson. The blue dots are electrons within a positive charged sphere-like structure. In such a case, the alpha particles would go through straight, just deflected by a very small degree because of the electric field. *Right:* The Rutherford model, a nucleus with high density and positive charge surrounded by electrons in circular orbits. In such a case, the alpha particles would be scattered strongly whenever they interact with the heavy nucleus, which happens seldom due to the small size of it.

Rutherford in 1911, in contrast to the Thomson model, postulated that the positive charge was concentrated in the center of system in a very small nucleus, while the electrons where orbiting the nucleus in a similar

way of planets orbiting around the Sun [5] (see figure 1.1). His idea was supported by an experiment performed in 1913 [6] by Geiger (1882-1945) and Marsden (1889-1970) where a thin gold foil was hit by alpha particles from a Polonium source. If the Rutherford model was correct, most of the particles must go through the gold foil while some of them would be scattered even to the opposite direction. This contribution started within the science of Physics a new field to study the nucleus inside the atom: Nuclear Physics.

Proposing the nucleus was not the last important contribution of Rutherford to this new field of science. In 1919 he reported about an experiment where an alpha particle was projected against Nitrogen, one Hydrogen nucleus was knocked out and an Oxygen-17 was produced in the reaction $^{14}N + \alpha \rightarrow ^{17} O + ^{1} H$. The obvious conclusion was that the Hydrogen nucleus was a component of the Nitrogen nucleus. Hence this result validated the William Proud hypothesis that the Hydrogen nucleus was the mass unit that form all nuclei. Rutherford named the Hydrogen nucleus, proton.

The Rutherford model was afterwards extended by Bohr and Sommerfeld, solving some of the problems that the atom model had. Still, there was a big problem in the structure of the nucleus, how could that positive charge be held together in such a small area? Rutherford himself proposed another particle composed by an electron and a proton together in 1920. Years later (1932), James Chadwick (1891-1974) found the neutron, a particle with the same mass as the proton but without any charge. This discovery allowed to explain the difference between the mass and the atomic number.

Nevertheless the new particle did not explain why the nucleus was compact and did not break-up due to the Coulomb repulsion, especially in the case of the heavier nuclei. In 1935 Hideki Yukawa (1907-1981) proposed a new force 100 times stronger than the Electromagnetic Force that only acted at very small distances of 10^{-12} cm: The Nuclear Strong Force. He proposed that in the same way the photons are exchanged in the Electromagnetic Force, the strong force exchange a heavy particle called meson with a mass between the proton and the electron. Years later in 1936 and 1947 the muon (μ) and pion (π) mesons were found in cosmic ray research, the latter is the primary force carrier for the nuclei force in atomic nuclei.

In 1933, Enrico Fermi (1901-1954) proposed an explanation to the beta decay, following the previous ideas from Heisenberg presenting this decay as transformation from a neutron to a proton, emitting an electron. This process was better clarified by Fermi, introducing the neutrino (ν_e), in order to conserve the spin within the decay. A new force, called Weak Force was introduced, 10,000 times weaker than the Electromagnetic force and responsible to keep these particles together before decaying by emitting an electron.

The basic foundations of Nuclear Physics appeared at the beginning of the XX century, although they continue to be developed fast through the later years. It was boosted by the funding related to the new energy production opportunities and unfortunately, to the different conflicts of the same century.

1.2 Going beyond the stability line to the dripline

Since the 1920s a new tool to further study the sub-atomic particle properties has been in constant development: The Particle Accelerators. These devices allow to accelerate charged particles for colliding against another particles or a certain target, in order to produce a nuclear reaction or break up in order to probe the structure of the involved particles and nuclei.

There are two main types of accelerators:

- Electrostatic accelerators, using static electrical fields like the Cockcroft-Walton and Van de Graaff
- Oscillating field accelerators, which use radio frequency electromagnetic fields.

The latter is the main method used by the current large-scale particle accelerators like the LHC or the accelerators at GSI. Throughout the XX century all stable or long-lived isotopes have been accelerated and used in hundreds of experiments. Such a scientific work has allowed developing new applications for these machines like implanting ions for material modification, carbon dating, cancer treatment or medical imaging.

Not many years ago, in the 1980s, new nuclei production methods were developed opening a new landscape of nuclei available to accelerate, therefore giving the opportunity to reach certain isotopes that were out of range before, plenty of unstable nuclei called exotic nuclei close to the limits of the nuclear force.

On the one hand, the first way to reach exotic nuclei is the ISOL method (Isotope Separation On Line). The process start with a previous acceleration of protons or heavy ions which are let to impinge on a thick target where the radioactive nuclei is produced. The produced nuclei diffuse through the thick target held at high temperatures towards the Ion-source, where it is ionized and extracted usually by applying an extraction voltage in the range of 30-60 KV. The outgoing beam is mass-charge selected by a magnet separation, after the process the beam can be further accelerated by injection into a post-acceleration stage or used directly for decay experiments. This method produces high quality beams which are comparable to stable beams, although the most exotic and short-lived isotopes are hard

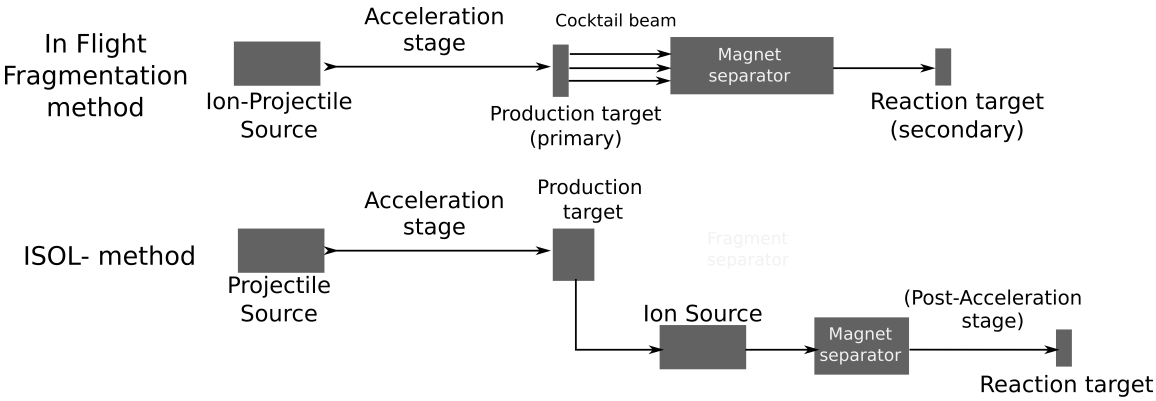

Figure 1.2: ISOL and In-Flight fragmentation method to produce exotic nuclei in particle accelerators. The ISOL method pre-accelerates a light ion that is shot to a thick target, producing a radioactive nuclei that continues towards the ion source. After the isotope is extracted from the source, it goes through an electromagnetic separator delivering it directly to decay experiments or to second acceleration. The In-Flight fragmentation method accelerates a heavy nuclei and make it collide with a light target to produce a cocktail beam. The process ends up with the nuclei species separated following the mass/charge ratio in an electromagnetic separator.

to produce because the extraction time from the ion source can be too long for these nuclei to survive.

On the other hand, the In-Flight fragmentation method can produce more exotic isotopes but the beam is worse in energy precision and beam focus as well as purity. In this case a heavy ion is accelerated until the desired velocity, it is let to impinge on a thin target producing a cocktail beam of several ions, which continues with a similar velocity through a magnetic fragment separator for selection before reaching a secondary target where the experiment is performed. This latter method only relies on tagging electronically the bunch of isotopes that reach the experimental hall contrary to the high-purity beams of the ISOL method. A scheme of both methods can be seen in the figure 1.2 .The first production and identification of relativistic radioactive beams was at Berkeley in 1979 [7][8] using ^{40}Ar and ^{48}Ca as primary beams using the fragmentation method.

All discovered isotopes are ordered on the nuclei chart (see figure 1.3) in a similar way the atoms were organized in the Mendeleev periodic table. This table arranges the nuclei in colors and positions following the stability and their amount of protons and neutrons. The limits of the nuclei chart are regarded as the dripline, but it does not have an obvious definition (a deeper discussion can be found in [9]). The dripline can be regarded

as the boundaries where the nuclei cannot keep more neutron or proton within them [10], in a more theoretical approach it can be referred as where the separation energy of the nucleons goes to zero [11], the definition can also point to the nuclei which last nucleon is not bound and has decay times within the strong force interaction times, 10^{-22}s or faster [12]. The definition of [11] gives an interpretation for the limits of the dripline to be at the lightest isotope for the proton-rich nuclei and the lightest isotone for the neutron-rich nuclei, in that case ^{6}Li, ^{6}He, ^{8}Li,^{8}He, ^{11}Be, ^{11}Li, ^{14}B, ^{14}Be, ^{17}C, ^{17}B, ^{19}C, ^{19}B, ^{22}N, ^{22}C and ^{26}F would be the limits for the light neutron-rich nuclei. The green nuclei of figure 1.4 have a negative separation energy $S_{n,p} < 0$ and decay by proton or neutron emission, they do not even have a bound energy level, thus they are usually regarded as unbound nuclei or nuclei beyond the dripline.

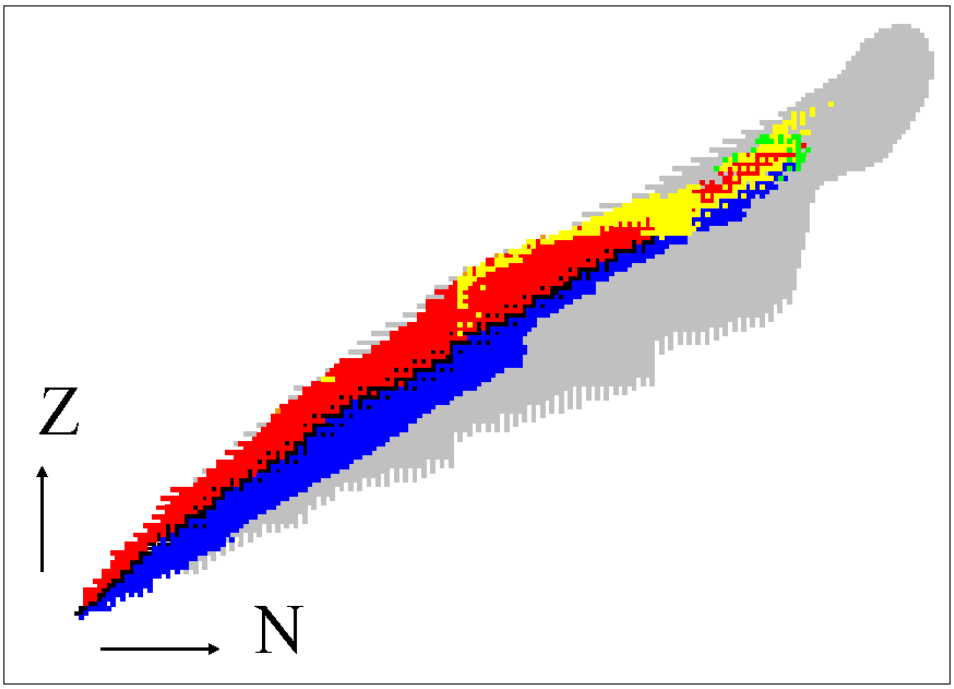

Figure 1.3: Chart of nuclei. It increases in neutron number from left to right, and increase in proton number from top to bottom. Black color isotopes are stables. Red colored are proton rich, thus promoting β^{+} decaying. Blue colored nuclei are neutron rich and promote the β^{-} emission. The grey-colored part are still unmeasured but predicted isotopes.

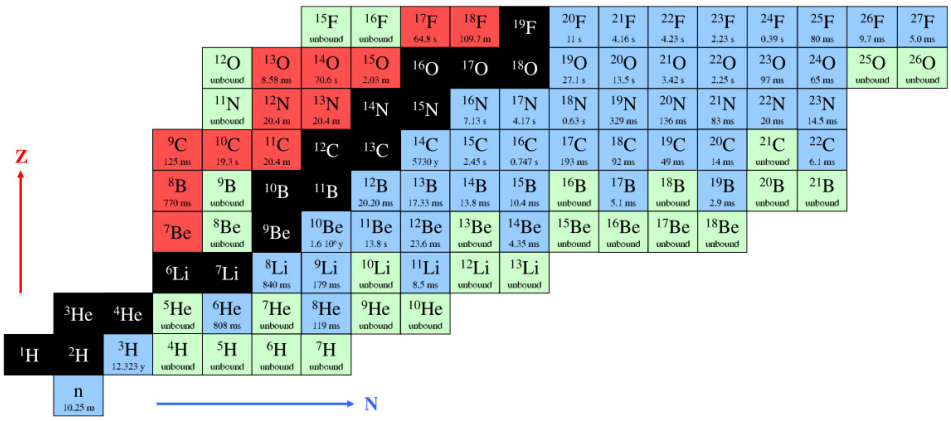

Figure 1.4: Nuclei chart zoomed to the light neutron-rich nuclei area. The black color label the stable nuclei, while the red and blue follow the same trend of 1.3 being proton-rich and neutron-rich with their suitable beta emission as their main decay. The green nuclei are unbound, thus beyond or on the limits of the dripline as described in the text, and decaying via proton or neutron emission. The image is taken from [13].

1.3 The dripline fauna: Halos and unbound nuclei

Due to the Coulomb repulsion the proton dripline is significantly closer to the valley of stability than the neutron dripline, hence the proton dripline has been reached before the medium mass region of Antimony and Bismuth with Z=51-83 [14] whereas the neutron dripline has been probe only up to Oxygen-Neon [15][16][17][18]. This thesis work is focused in the light neutron-rich side of the nuclei chart and the phenomena that emerges there.

1.3.1 Halos

The first experiments using unstable beams studied the nuclear size, in previous years such kind of experiments were performed using electron beams to study the proton charge distribution of the nucleus. In order to probe the nucleon distribution of unstable beams, the interaction cross section (σ_I) with a known target was the measured observable, defined as $\sigma_I = \pi[R_I(projectile)+R_I(target)]^2$, where R_I is the radius of the projectile or the target. The size of several neutron-rich isotopes of Helium, Lithium, Beryllium and Boron were investigated by Tanihata et al between 1985 and 1988 [19][20][21], using beams of 800 MeV/u on Beryllium, Carbon and Aluminum targets. Certain cases such as ^{6}He, ^{11}Be and remarkably ^{11}Li and ^{14}Be had a large radii in comparison to their neighbours and much

stronger than the commonly observed trend $R \sim 1.18 \cdot A^{1/3}$ for the stable nuclei (see figure 1.5). This data suggested a deformation or a matter distribution tail.

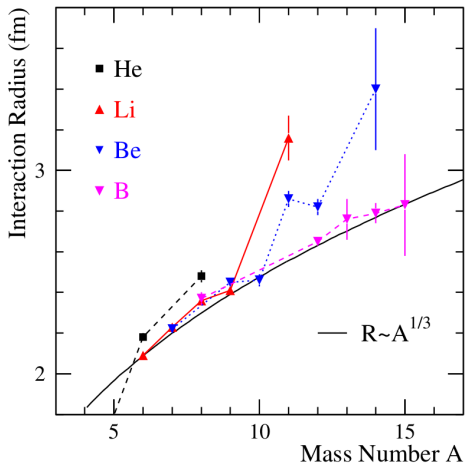

Figure 1.5: Radii comparison between the stable nuclei trend of $R \sim A^{1/3}$ and several isotopes of Helium, Lithium, Beryllium and Boron. The size increase of ^{6}He, ^{8}He, ^{11}Li, ^{11}Be and ^{14}Be is pronounced. Image taken from [22].

This feature was defined by Hansen and Jonson in 1987 [23] as Halo structure, it was understood as an extension of the nucleus size caused by one or two nucleons tunneling out of the classical forbidden region of the nuclear core potential, therefore certain loosely bound nucleons increase the size of the system leading to an escalation of the interaction cross-section. This phenomenon only occurs with a weak Coulomb or centrifugal barrier, causing that the only recognized halos nuclei from the neutron deficient side of the nuclei chart are ^{8}B, ^{17}F, ^{17}Ne and deuteron if it is considered as such, whereas neutron halos are more than 10 isotopes (considered from [24] in 2013).

The large space distribution can be correlated using the Heisenberg principle to a very narrow momentum distribution which is another signature of the halo structure. In the same way, a small binding energy and low relative angular momentum of the valence nucleons (s or p states) are also conditions for the formation of halo states.

Within the halo structure it is worth considering two different cases, the two-body halos, like ^{11}Be or ^{8}B that only have one loosely bound nucleon in the last orbit and the three-body halos, like ^{11}Li and ^{14}Be which have two nucleons instead. This latter kind is widely known as *Borromean nuclei* [25] and have certain special properties. The name comes from the

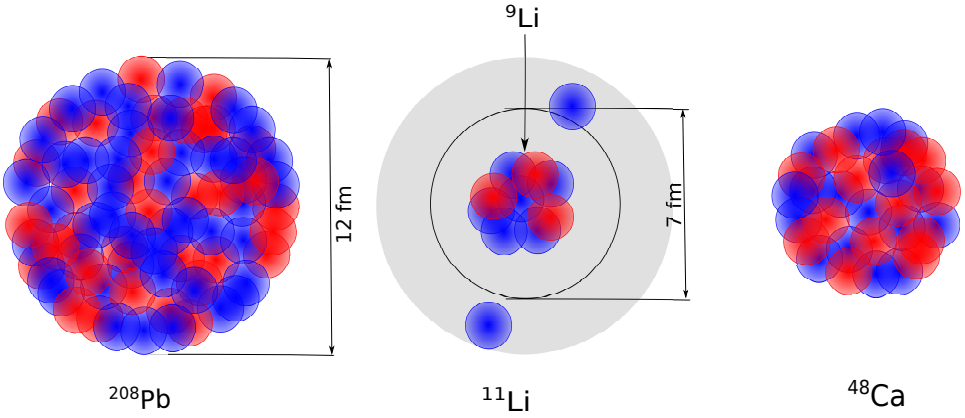

Figure 1.6: Size comparison between the schemes of the stable nuclei ^{208}Pb and ^{48}Ca and the two neutron halo nuclei ^{11}Li (middle of figure). The size of the nucleus with $R_{rms} \sim 3.53(10)$ fm [24] is comparable to the ^{48}Ca, whereas the distance between the two neutrons can reach the size of the ^{208}Pb $R_{nn}^{rms} \sim 6.6(1.5)$ fm [10].

court of arms of the Borromeo family from Italy, three linked rings such as if one of them is removed the others would disentangle. The relationship of the symbol with the three-body halo structure comes from the fact that such a structure is bound while the two possible subsystems, isotope + nucleon or nucleon + nucleon are unbound. Hence, this produces certain pairs of isotopes that the odd neutron-numbered is unbound while the even neutron-numbered is bound.

^{11}Li was the first identified halo and still is the prototype for comparison. It ground state has a binding energy around 300 keV [10] with a total matter radius of 3.53 (10) fm for the interaction cross-section [24] (see figure 1.6 to compare it with Calcium and Lead). For the purposes of this thesis, the halo nuclei ^{14}Be has special interest, it has a binding energy of above 1 MeV and a matter radius of 3.10(15) fm [24] from interaction cross-section. The core of this nuclei is ^{12}Be which is easily polarizable and it is known to have four bound states 0^+, 2^+, 0^+ and 1^-. It has the N=8 shell closure suppressed (as well as ^{11}Li), making it show parallel properties to the ^{8}He, thus it is closer to a ^{10}Be+n+n+n+n system than a ^{12}Be+n+n. The unbound nuclei ^{13}Be, in the middle ground between the core isotope ^{12}Be and the borromean ^{14}Be needs to be studied to have a deeper knowledge of this area of the nuclei chart.

1.3.2 Unbound nuclei

Light nuclei close to the dripline are marginally bound, thus they usually do not have particle-bound excited states, nevertheless it is possible to feed excitations in the continuum. As has been mentioned before in the text and it is clearly stressed in figure 1.4, it is possible to produce and observe certain combinations of protons and neutron that are beyond the dripline, such systems without bound states are known as unbound nuclei.

It is common to refer to these non-bound states as resonances, not as nuclei. Therefore, the prime question that should be asked upon approaching unbound nuclei is *what is defined as a nucleus?*. Unfortunately there is not a satisfactory agreement around this subject. The main criteria that can be followed to achieve a conclusion is the lifetime of the potential nucleus. As explained for the halo nuclei, the two barriers that must be overcome by a nucleon to tunnel out of the nuclear core potential is the Coulomb barrier and the angular momentum, thus the lifetimes of the neutron-deficient isotopes can be much higher and usually increase with Z (with the Coulomb barrier), even longer than the $\sim$ms scale of the beta decay. On the other hand, the neutron-rich isotope neutron emission is just hindered by the angular momentum, hence they usually have lifetimes lower than picoseconds. The IUPAC (International Union of Pure and and Applied Chemistry), which is the world authority about naming and setting chemical elements, set a constraint for considering a new element of at least 10^{-14}s [26] of existence based in the time needed for a nucleus to acquire its outer electrons, as an element can not be considered as such without electrons. Such a guideline would be an applicable criterion, although following a similar reasoning, the time-scale for nuclear phenomenon (as mentioned at the end of section 1.2 about the dripline) is in the order of 10^{-22}s, therefore such a lower limit would be more consistent. However, this reference threshold is just not clearly defined (more about this discussion can be found in [9]).

The first measured neutron-rich unbound nucleus was ^{5}He in 1937 by Willams et al [27] and it was not until 1965 [28] with the study of the di-neutron scattering length that another resonance was found. Since then, and more insistently after the development of the radioactive beams, a wide-variety of these neutron unbound nuclei have been identified. The figure 1.4 show the wide variety of these resonances that have been found in the last years, making obvious that in order to have a deep understanding of the boundaries of nuclear structure is mandatory to investigate them. The bound nuclei with the highest ratio $\frac{N}{Z} = 3$ is ^{8}He, whereas the unbound systems are able to reach much higher limits like ^{7}H and ^{10}He with $\frac{N}{Z} = 7,4$, therefore with a ratio difference with the last bound isotope of $\Delta\frac{N}{Z} = 4,1$. The theoretical nuclear models, due to the difficulties of the many-body problem, are still not able to describe in a general way the nuclear force. The unbound systems are laboratories to test the theoretical

models for the interaction between a core and single neutron (in the case discussed here) above or on the limits of the nuclear force.

Recent summaries and updates in unbound nuclei research had been published by Tanihata et al [29], Simon et al [13] in 2013 and Baumann et al [30] in 2012. Some of the most recent results for neutron rich unbound nuclei, involve assigning a ground state 0^+ and a excited state 2^+ for the ^{10}He [31][32]. The $^{25-26}$O resonances have also been subject of research lately [18][17] finding a ground state $3/2^+$ for the first, and a 0^+ground state and a 2^+ excited state for the latter. The Oxygen neutron-rich chain has been the subject of special attention due to the intention to reach the double magic nuclei ^{28}O.

1.3.3 ^{13}Be

The exotic Beryllium isotope with 13 mass number has been very controversial over the last years, being the target of several studies. The following will be a brief report of the previous published results.

The first observation was in 1983 by Aleksandrov et al [33] using the reaction ^{14}C(^{7}Li,^{8}B) finding a state at 1.8 MeV above the ^{12}Be + n threshold, with Γ=0.9$\pm$0.5 MeV, using the missing mass method. Almost ten years passed until the next measurement was made by Ostrowski et al in 1992 [34] at VICKSI (Berlin) using a double-exchange reaction ^{13}C(^{14}C,^{14}O)^{13}Be at E_{lab}=337 MeV, determining that the ground state was at 2.01(5) MeV against one neutron emission with Γ=0.3(2) MeV and one excited state at 5.13(7)MeV with Γ=0.4(2)MeV, even finding indications of another excited state around 7.51 MeV. In 1995 Korsheninnikov et al [35] with d(^{12}Be,p), observed the same state around 2 MeV as well as suggesting three excited states around $\sim$5, 7 and 10 MeV. At the same time, von Oertzen et al [36] published a measurement at 24 MeV/u for the reaction ^{13}C(^{14}C,^{14}O) producing a strong resonance at 2.01 MeV which they attributed to a $d_{5/2}$ state, and another at 5.13 MeV. Belozyorov et al [37] in 1998 used the reaction ^{14}C(^{11}B,^{12}N) at 190 MeV/u, they assigned a J=1/2 character tentatively to a ground state settled to the lower energy of 0.80(9) MeV, and reported about several additional states at 2.02(10), 2.90(16), 4.94(12), 5.89(14) and 7.8(2) MeV. The next important observation was published in 2000 by Thoennessen et al [38] using a 80 MeV/u beam of ^{18}O fragmented on a ^{9}Be target, reporting about a low-lyings($<$200 keV) s virtual state with a_s $<$-10 fm scattering length. In 2004 Simon et al [39] published results from GSI using a ^{14}Be beam of 250 MeV/u impinging on a carbon target which produces two p and d wave resonances. That same year Lecouey et al [40] reported about a one proton knockout experiment at GANIL using a 41 MeV/u beam of ^{14}B impinging on a Carbon target and used the invariant mass method to find a low-lying s-state at about 0.7 MeV and d-state at around 2 MeV. Haik Simon et al [41] performed another experiment in 2007 with a 287 MeV/u

beam of ^{14}Be, reporting a s-virtual state with a scattering length of a_s <-3.2 fm.

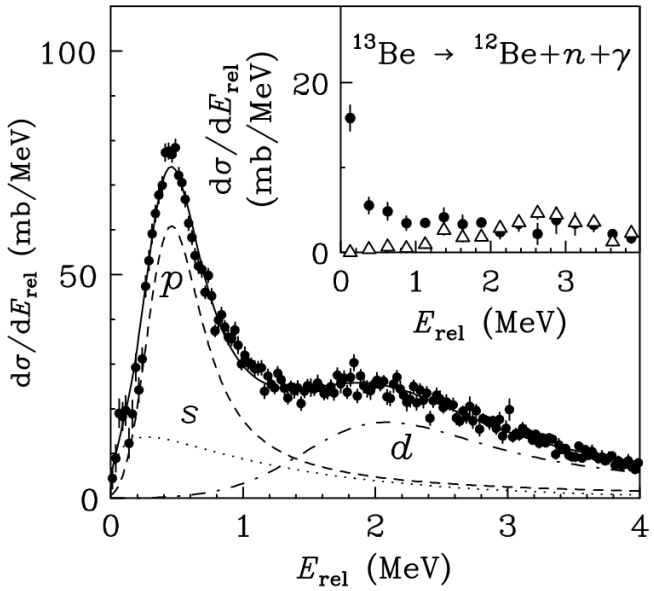

Figure 1.7: ^{13}Be relative energy from the published paper of Kondo et al [42]. The relative energy is fitted to one s-virtual state and two resonances p and d, further information in the text. The inset shows superimposed the relative energy of ^{13}Be in coincidence with two γ rays from the ^{12}Be. Black circles with the 2.1 MeV and white triangles with the 2.7 MeV gamma.

In 2010, Kondo et al [42] published the results from an experiment performed at RIKEN using the invariant mass method with a one-neutron removal reaction of ^{1}H(^{14}Be,^{12}Be+n) with 69 MeV/u energy, it was the first experiment carried through that measured the γ rays coming out of the ^{12}Be daughter. Kondo found one virtual s state with a_s=-3.4(6) fm and two resonances at 0.51(1)MeV and 2.39(5)MeV with p and d character. The Relative energy extracted in that experiment is in figure 1.7.

Aksyutina and the R3B Collaboration [43] published new results coming from an experiment performed at GSI with 304 MeV/u using ^{14}Be neutron knockout impinging on a Hydrogen target in 2013. Additionally to the analysis of that data they adopted an holistic approach including in the interpretation of the results the data coming from Kondo [42], and taking into account the previously published results of the ^{13}Be. They assumed for the analysis that as the structure of ^{14}B has the main configuration ^{13}B($3/2^{-}$)$\otimes$(sd) [44], meaning that only s and d states should be populated significantly in ^{13}Be whereas with neutron knockout p states can be populated. The investigation used the invariant mass method to get the relative

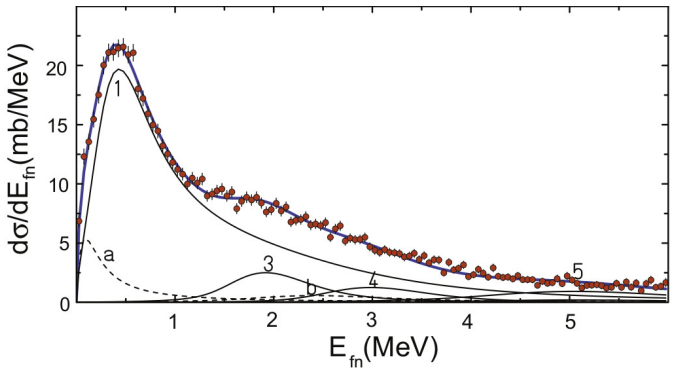

Figure 1.8: ^{13}Be relative energy from the published paper of Aksyutina et al [43]. The resonance number 1 describes the contribution from the two l=0 resonances with destructive interference. a and b are the cross-section of the relative energy in coincidence with gammas coming out of ^{12}Be found by Kondo (see figure 1.7). The component 3 have 1.95 MeV whereas the component 4 is at 3.02 MeV, the state at 5.2 MeV is the component 5.

energy of the system ^{12}Be + n, whereas in order to extract the momentum interpretation of the resonances they used the momentum profile method (previously explained also by Aksyutina [45] that same year), taking advantage from the assumption that the knocked out neutron inside the projectile (^{14}Be) have the same momentum of the ^{12}Be + n system. They performed a previous fit of the data considering the ground state to be $1/2^+$ at 0.81(6) MeV, the momentum profile analysis reported about a complication in the interpretation in this state, which seemed like a combination of $1/2^+$ and $1/2^-$ character. In order to solve this latter complication they introduced the possibility of destructive interference between two s-states, performing a new fit. The conclusions they reached included settling the ground state at 0.46 MeV as an s-state interfering with an excited s-state at 2.9 MeV, one $1/2^-$ state at 3.02 MeV and one $5/2^+$ state at 1.95 MeV as well as one final state at 5.2 MeV with J=$5/2^+/3/2^-$ character. They left open the possibility of another state around 1 MeV with $l \neq 0$. In figure 1.8 the relative energy spectrum of Aksyutina is shown [43].

The last experimental result was published by Randisi et al [46] in 2014 from GANIL (figure 1.9 display the final result of decay energy). The investigation was carried out using a $^{14-15}$B beam of 35 MeV/u via breakup on a carbon target. The invariant mass method was used to extract three different resonances at E$_r$= 0.4, 0.85 and 2.35 MeV with an angular momentum of J=$1/2^+$, $5/2^+$ and $5/2^+$.

This work is about an experiment that populates ^{13}Be using ^{14}B (p,2p)^{13}Be reaction in a CH_2 target, including quasifree scattering con-

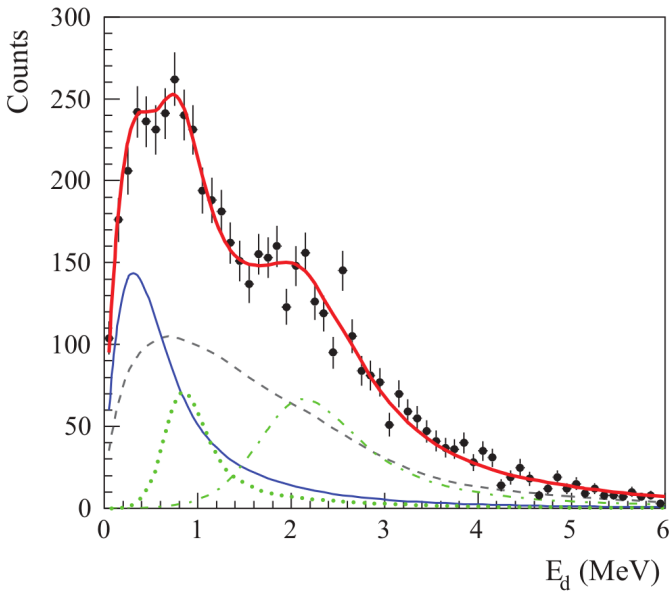

Figure 1.9: ^{13}Be decay energy from the published paper of Randisi et al [46]. The blue solid line is the ground s-state at 0.40(3) MeV whereas the dotted green line is a d-wave resonance with 0.85(13) MeV and the dot-dashed green line is a another d-wave resonance with 2.35(14) MeV. The gray dahsed line is a nonresonant continuum.

ditions. This work features a gamma-ray detector, which only has been included before in the work by Kondo et al. The experiment was performed at GSI in 2010 by the R3B Collaboration.

1.3.4 Resonances or quasi-stationary states.

As the main subject of this work are the previously mentioned unbound or resonance states, it formal interpretation will be briefly introduced.

A simple interpretation of the resonances [47] could be understood taking into account the square-well potential model with a particle inside. It is well-known that in a such a case the wave-function will only be solved by a finite number of negative energies within the potential and the particle will be classically confined inside. The wave that represents the particle needs to be in phase whenever it reaches the boundaries to the potential, this only happens in such a finite number of energies. However outside the square-well the wave can adopt any energy, although it must be taken into account that the discontinuity of the potential provokes reflection to particles with energies close to the boundaries, therefore close to the potential

frontier there are certain favoured energies as well, that keep the particle at least partially confined. Such a energies are called resonances or quasi-stationary states. This is a quantum phenomenon that does not happen in the classical world. These resonances emerge as prominent peaks of the excitation spectrum (i.e. relative energy for the unbound systems studied in this work), as a hint that there is this kind of state at that energy position.

1.4 Direct Reactions: Knockout

Since Rutherford nuclear reactions has been one of the main methods to probe the atomic nucleus. The collision of subatomic particles or nuclei breaks them out in their inner components or change them in a fundamental way. The reaction outcome is greatly determined by the energies of the used projectiles, such an energy selection can be done using the particle accelerators.

The nuclear reactions are usually distinguish as two different types [48][47]. If the interacting components form a compound system which stays together long enough to share the energy uniformly, then at some point that energy is accumulated in one component which makes the system to decay, this is called Compound Reaction. On the other hand if the interaction is glancing between both particles, if it is rapid in the nuclear force order of magnitude ($\sim 10^{-22}$s) (which can be up to six order of magnitude faster than the compounds reactions), is regarded as Direct Reaction. The latter is favoured at higher energies of the projectile and at the same time, taking into account the De Broglie hypothesis($\lambda = \frac{h}{p}$) , the wavelength of the particle would decrease with the energy, making easier to penetrate inside the nucleus and probe more bound components.

There are three main types of Direct Reactions, besides elastic scattering where there are not modification of the nucleus. The first case is when the incident particle suffers inelastic scattering and the received energy is spent on exciting rotational and vibrational modes of the nucleus. The second case include modifications in the nuclei composition, such reaction involves the transfer of one or several nucleons from either the target to the projectile (Pick-up reaction) or the opposite (Stripping Reaction). The last type of reaction is regarded as Knockout Reaction, and the interaction of the projectile with the target, provokes the ejection of one nucleon or light fragment from the target which continues freely.

Knockout reaction have been used as a powerful tool to probe the deeply bound nuclear shell structures [11], using high energy beams (more than 100 MeV/u). As this kind of reaction involves at least three outgoing particles, due to the momentum conservation, in order to understand the whole picture is needed to sum all the outgoing momenta. The figure 1.10 shows an scheme of a typical knockout reaction with an incoming proton

impinging on a nucleon inside a Target of mass number A. The momenta conservation is indicated in equation 1.1, considering the Target to be at rest whereas the nucleon inside the Target have certain momentum.

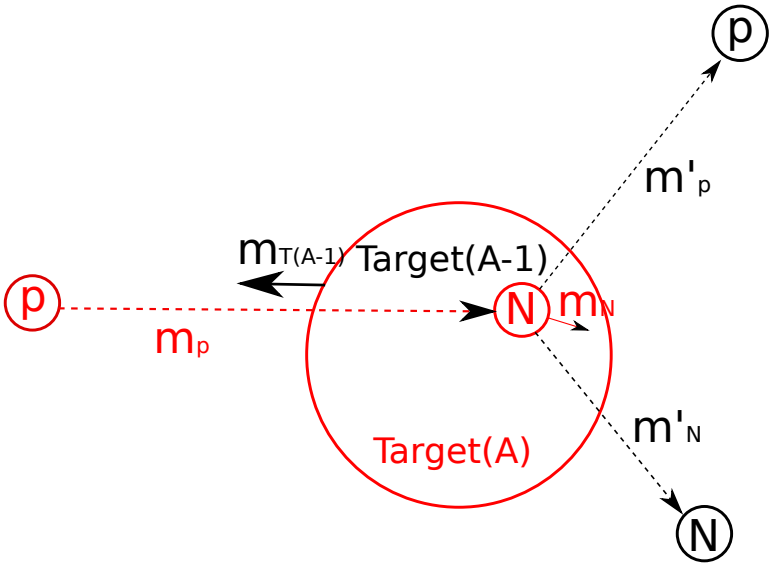

Figure 1.10: Scheme of a Knockout Reaction of a proton(p) impinging on a Target(T) with mass number A, knocking out a nucleon(N). m are the linear momenta, red color indicates the situation before the reaction whereas the black colored lines and spheres indicates the outcome of the reaction. Dashed lines indicates the moving nucleons. The opening angle between particles of the same mass in a Knockout Reaction is $\sim 90°$.

$$m_p + m_N = m_{T(A-1)} + m'_p + m'_N \tag{1.1}$$

In order to investigate the most exotic nuclei provided by the radioactive beams (see section 1.2), it is advisable to use *Inverse Kinematics*. This technique involves colliding unstable nuclei with any mass against light stable targets, therefore the object of interest of the experiment is the beam nuclei not the target as it usually was with stable beams. Such an approach inverts the intention of Knockout reactions to knocking-out a nucleon from the beam not from the target. Using such a method it is possible to populate very short lived nuclei such as unbound resonances that would not survive the flight through a fragment separator.

1.4.1 Quasifree scattering

The quasifree scattering (QFS) reaction is a knockout reaction that fulfill certain conditions. The projectile must be simple, usually a proton

or an electron, which can be single or within a nuclei. The key condition is that the rest of the projectile is not involved in the reaction process, acting as a spectator. Therefore the interaction can be considered as quasifree, in first approximation other kind of interactions does not need to be taken into account. The typical reactions are (e,e'p), (p,2p) or (p,pn), although this work is going to focus in the (p,2p) reaction. This type of reaction has been a primal interest of the R3B Collaboration as a tool to investigate the single particle structure or the cluster structure of a nuclei. Several works have been carried out studying this kind of reaction e.g. [49][50][51][52].

In reactions like (p,2p) or (p,pn) a proton from the target knock-out a nucleon from the beam in inverse kinematics. Both particles are emitted in the same plane, and as both have the same mass, with an opening angle of $\sim$90° in the laboratory frame. The coplanar condition translates to $\Delta\phi \approx$ 180°, whereas the opening angle using high energies in inverse kinematics produce an opening angle of $\Delta\theta \approx 80°$, such a degrade in the opening angle is because of the mass increase of the incoming nucleon due to the relativistic velocities ($\beta \approx 0.7$). Both angular trends can be used as signatures of the presence of this kind of reaction. The signatures can be seen in figure 1.11. A good summary with further explanation of this kind of reaction is [53].

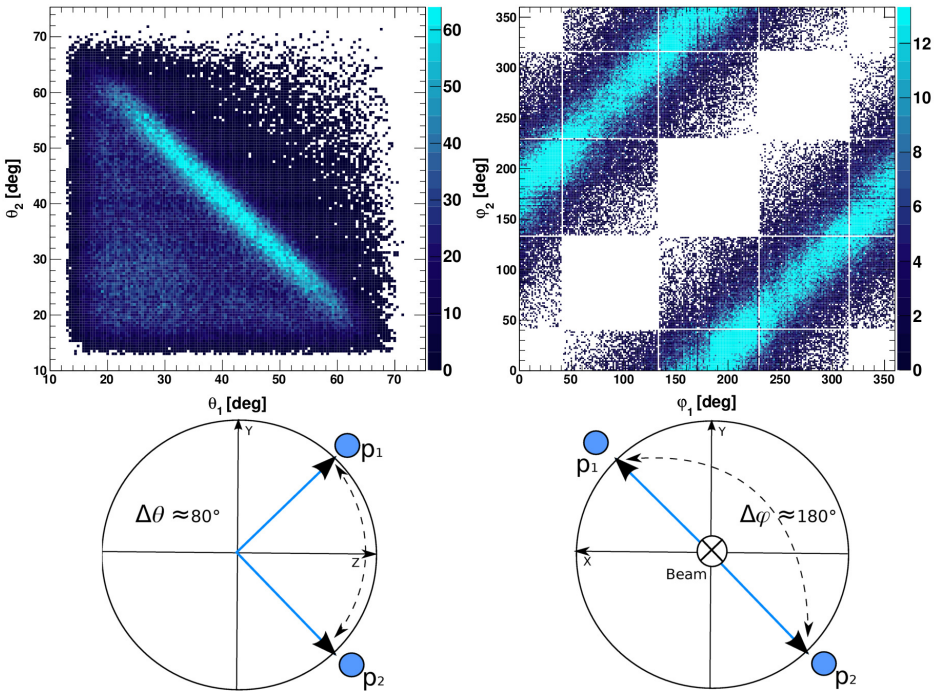

Figure 1.11: Quasifree scattering signatures for a (p, 2p) reaction with CH_2 target. *Left:* It shows the opening angle correlation $\Delta\theta \approx 80°$for a high energy QFS reaction in inverse kinematics in the laboratory framework. *Right:*It shows the $\Delta\phi \approx 180°$ coplanar correlation of the QFS reactions. Angular correlations taken from [50].

" There is nothing like looking, if you want to find something.
You certainly usually find something, if you look,
but it is not always quite the something you were after. "
J.R.R Tolkien, The Hobbit

2 Experiment & Detector setup

2.1 The experiment

The data used in this thesis is coming from the S393 experiment [54] performed in the late summer of 2010 at GSI Helmholtzzentrum für Schwerionen-forschung GmbH by the R3B Collaboration. The experiment was focused on two main tasks, the study of astrophysical reactions ratios relevant for the r-process nucleosynthesis and the use of quasi-free knock-out reactions to study the evolution of shell and cluster structures close and beyond the neutron-dripline. In order to reach the channels of interest, six different settings of mass-to-charge ratios were used for the fragment separator.

The experiment had 21 beam days and a large amount of collaborators were involved along the preparation and run of the experiment, the information that might be of relevance was written to the elog [55]. As the dataset was huge, more than ten thesis have results based on the research done in this experiment, and the interaction between the PhD students and the professors involved is done through a second analysis elog [56].

The aim of this work is the study of the shell structure of ^{13}Be, a neutron-rich nucleus at the dripline, this was done using (p, 2p) reaction knocking out deep bound protons from the incoming beam ^{14}B.

2.2 GSI Helmholtzzentrum für Schwerionen-forschung GmbH

GSI [57] is a facility built in Darmdstadt (Germany) in the year of 1969 and since then has been dedicated to the production and acceleration of heavy ions, currently it cooperates with hundreds of institutes around the world on research in different areas like material, biophysics, medical science, plasma, atomic and of course nuclear physics. Several of the super-heavy elements have been discovered at GSI, including Bohrium-107, Meitnerium-108, Roentgenium-111, Copernicium-112 and Hassium-

108 named after the German state of Hesse, and Darmstadtium-110 named after the location of the research center.

Currently a major upgrade is being performed in the facility, thus it is not in operation at this time. The future installation FAIR (Facility of Antiproton and Ion Research) will be one of the largest research projects worldwide, providing ion and antiproton beams of high intensity and quality.

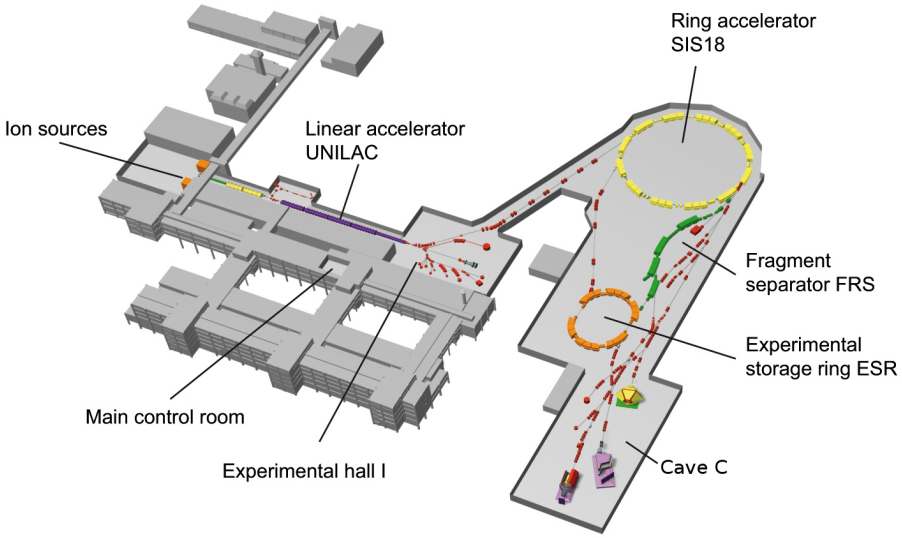

Figure 2.1: Overview of the GSI accelerator facility and the experimental beam production technique followed for the R3B Collaboration experiments. The ion source produce the primary beam, which is accelerated in the UNILAC and send to the SIS18 in order to reach the higher energies. When the beam is extracted from the accelerator it is let to impinge on a light target that produces a cocktail of particles which goes through the FRS that separates the different species before reaching the R3B experimental hall: Cave C, where is situated the detectors setup.

2.2.1 Ion sources

There are several ion sources in GSI for the production of a wide variety of ions with different intensities and ionizations, but in order to produce Argon as primary beam there were two sources (see figure 2.2) on operation 2010, when the experiment was carried out:

- PIG (Penning Ionization Gauge) ion source
  This source generates plasma inside a strong magnetic dipole field, producing gaseous and metallic ions.
- MUCIS (MUlti Cusp Ion Source)
  This ion source has three spiral tantalum filaments placed simmetrically relatively to the beam axis. 60 SmCo-magnets creates the multicusp field of 1.8 T for producing all types of ion gases.

Figure 2.2: Pictures of the sources PIG(left) and MUCIS (right). From [57]

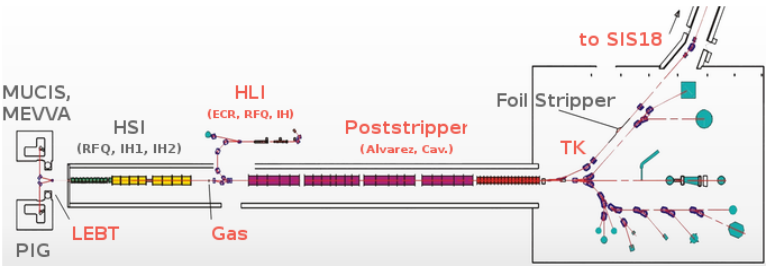

Figure 2.3: Scheme of the UNILAC and the connection with the ion sources and the SIS 18

2.2.2 UNILAC

The UNIversal Linear ACcelerator [58] is the first acceleration stage, able to reach beam energies up to 11.4 MeV/u for elements from hydrogen to uranium.

From the ion source, the beam goes through the High Current Injector (HSI) which consist of a low energy beam transport system (LEBT), the 36 MHz IH-RFQ accelerating the ion beam from 2.2 to 120 keV/u and RFQ adapter matching to the IH-DTL consisting of two separate tanks accelerating the beam up to the HSI maximum energy of 1.4 MeV/u. The beam

is stripped in a gas and one charge state is selected before injection to the DTL section where is accelerated to 11.4 MeV/u. Before the transfer to the SIS18, there is a foil stripper and a charge state separator.

2.2.3 SIS(SchwerIonenSynchrotron) 18

The pre-accelerated ion beam coming from the linear accelerator is further accelerated in the heavy-ion synchrotron up to 90% of the speed of light. The ring has a 216 m circumference with a maximum bending power of 18 Tm. A proton beam can be accelerated up to 4.5 GeV while an Uranium beam can reach 1 GeV/u, the beam emmitances can go from 30x8 to 5x8 mm mrad.

The beam in a synchrotron needs different time periods to be accelerated before extraction, this causes that the beam goes forward in ion bunches with pauses in-between. The acceleration cycles are called spills.

When the beam is extracted from the SIS it is let to impinge in a thin primary target with low Z, producing the secondary beam of a wide variety of lighter elements which are injected in the FRS. During the S393 experiment this primary target was Beryllium of 4011 mg/cm^2. In this experiment the Argon (^{40}Ar) primary beam was accelerated up to 490 MeV/u.

2.2.4 FRS

The FRagment Separator [59] [60] is an achromatic magnetic forward spectrometer with a momentum resolving power of 1500 for an emittance of 20π mm mrad. It is composed of four stages each of them consisting in 30° dipole magnets and a set of quadrupoles before and after the dipole in order to focus the beam (see figure 2.4).

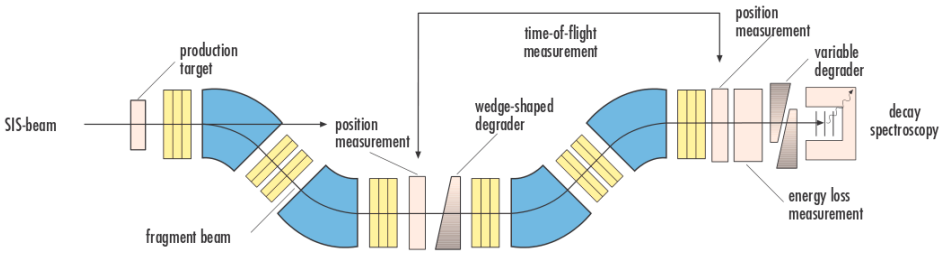

Figure 2.4: Overview of the fragment separator. The blue dipoles bend the beam in order to apply the magnetic rigidity method, and the wedge degraders in pink-grey assures a specific energy loss. The yellow colored parts are quadrupoles for focusing purposes and the scintillators for measurements are pink.

After the primary target the species of the secondary beam are selected using a method involving the energy loss of the isotopes and the magnetic rigidity. First the ions are separated according to their mass-charge ratio, this is done based in the Lorentz force which equals the centripetal force on a circular radius ρ keeping the ratio between the charge (Z) and the mass (A) of the isotope, which can be summarize in the equation 2.1, where K is a constant, B is the magnetic field intensity, β is the ratio of the velocity of the isotope and light and γ is the lorentz factor. The latter equation is only valid for high energies, fully stripped beams like the used in this facility. Therefore what this equation means is that for a specific ratio $\frac{A}{Z}$ a certain magnetic rigidity ($B\rho$) is fixed, thus those ions will follow a unique trajectory(ρ) for a given magnetic field(B).

$$B\rho = K \cdot \frac{A}{Z} \cdot \beta \cdot \gamma \tag{2.1}$$

A wide variety of ions will have the same mass-charge ratio so in order to distinguish between them the separator use wedge-shaped degraders as can be seen in figure 2.4. The energy loss of heavy charged particles follow the Bethe-Bloch formula (2.2), which states that is higher according to the amount of material went through, these wedge degraders have different depth, thus will cause different energy loss depending on the trajectory. This cause the beam intensity loss in the process, so for some experiments it is necessary to avoid this last kind of ion-selection process.

$$-\frac{dE}{dx} = \frac{4\pi n Z^2 e^4}{m_e v^2}\{ln\frac{2m_e v^2}{I[1-(\frac{v}{c})^2]} - (\frac{v}{c})^2\} \tag{2.2}$$

Along the FRS there is up to eight different 3 mm thick scintillators, called from S1 to S8, in order to perform time-of-flight, position and energy lost measurements, which are needed to monitor the beam.

2.3 Cave C: R3B Setup

After the beam has passed the fragment separator it ends up in the Cave C, where the R3B setup has been producing data for many experimental campaigns with small changes between them, in this document just the S393 configuration will be explained. An overview of the setup is shown in figure 2.5.

The main feature of this detector setup is being capable to make complete kinematic measurements, this means that is able to record all the information including energy, mass and charge from the different incoming isotopes and the outgoing reaction products. To accomplish this it is equipped with a large variety of plastic scintillators, stripped and non-stripped silicons, fiber detectors and a strong electromagnet.

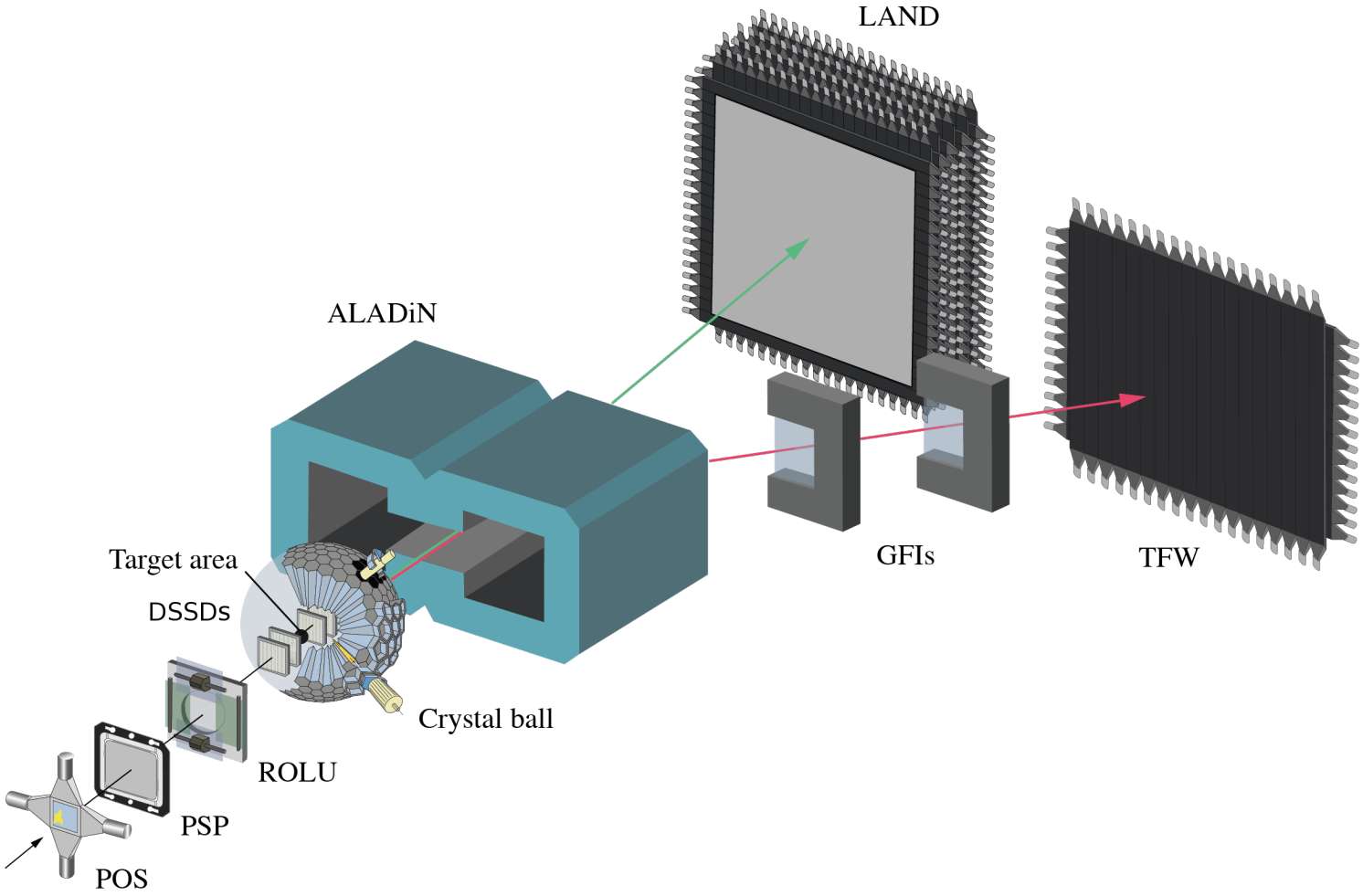

Figure 2.5: Setup overview. The important detectors are shown, and the three different setup stages are indicated as well, the incoming, around the target and outgoing, the latter is divided in three branches based on the purpose: neutrons,fragments and protons. The proton branch is not included because it is not used in this work. Imagen taken from [61].

The setup can be divided in three different stages following the position and purpose of the detectors: Incoming, around the target and outgoing.

2.3.1 Incoming beam detectors

S8 and POS

In order to make time-of-flight measurements two scintillators are used, S8 is the last one of the previously mentioned from the FRagment Separator, it consists on a plastic paddle with two photomultipliers (PMTs) at both ends.

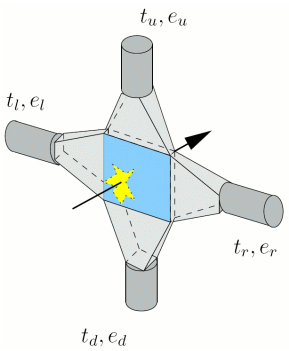

Figure 2.6: Schematic view of the POS. When the beam hits the plastic, the scintillation light is produced, reaching the four photomultipliers. The four signals collected in the PMTs give time, energy and position information of the beam, although nowadays this detector is primarily used only for the time-of-flight.

The POS is located in the incoming beam pipe of the Cave C setup, it consist on a square shaped plastic of 5.5x5.5 cm^2 with four PMTs attached to the sides, it is generally used as the start of the time-of-flight measurements and also can give information of the energy loss of the beam. An scheme of the detector is shown in figure 2.6.

ROLU

The ROLU device allows to define the beam size before reaching the reaction target, using four remotely controlled scintillators. Any particle that doesn't go through the defined hole made by the disposition of the four scintillators as can be seen in figure 2.7 will hit one of them and produce a signal which can be used as a veto trigger for the Data Acquisition System.

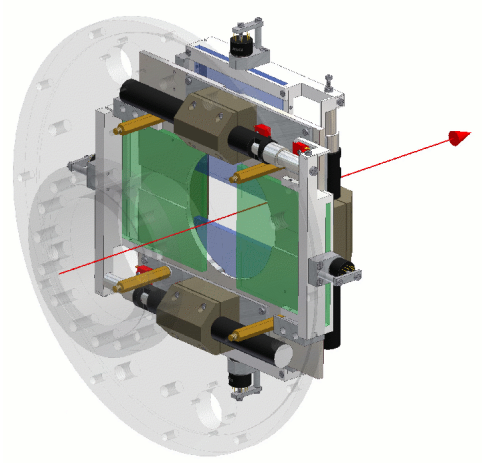

Figure 2.7: The ROLU names comes from the four scintillators in German: Rechts (Right),Oben (Above),Links (Left),Unten (Below). The paddles has the size of 95x100 mm^2 and a thickness of 5 mm.

PSP

The Position Sensitive silicon Pin diode (PSP) is a square plate of high resisting n-type silicon with a thickness of 300 μm and an active area of 4.5 x 4.5 cm^2. This detector is used for tracking the beam position and for identification of the isotopes charge by energy loss. The front side of the plate has Boron ions implemented, forming a p-n junction, making this side the anode and the other side as the cathode.

As can be seen in figure 2.8, there are four independent readouts in the corners of the anode, in order to collect the charge for position reconstruction purposes. As the charge fraction collected in each different readout is proportional to the position of the charge deposition it is possible to extract that information using the equations 2.3 & 2.4. The cathode also have one charge collector which allow to know the energy loss on the detector.

$$X_{pos} = \frac{(Q_2 + Q_3) - (Q_4 + Q_1)}{(Q_1 + Q_2 + Q_3 + Q_4)} \tag{2.3}$$

$$Y_{pos} = \frac{(Q_1 + Q_2) - (Q_3 + Q_4)}{(Q_1 + Q_2 + Q_3 + Q_4)} \tag{2.4}$$

The PSP have a position resolution of approximately 200 μm and an energy resolution of 1%.

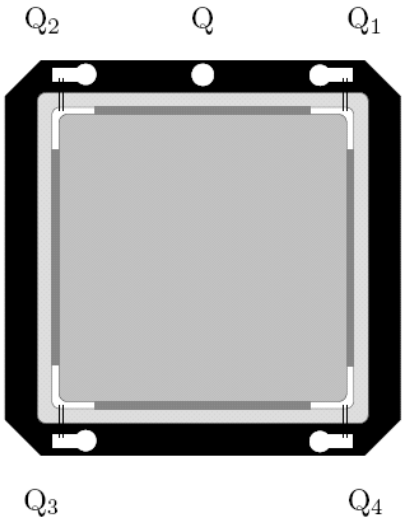

Figure 2.8: Schematic view of the PSP. The anode holds the 4 position detection charge readouts while the cathode have one single contact for charge collection to detect the total energy loss of the incident nuclei in the detector.

2.3.2 Around the target detectors

Target

Of course the target is not a detector but it is used to select the reaction channel and is a main part of the setup as well and that is why is included in this description.

The target holder is a wheel with several square-shaped locations around the border to keep a variety of targets (see figure 2.9). It is remote controlled from outside the experimental hall, which allow to change the desired target without opening the cave.

In the experiment S393, three different targets were used:

- Polyethylene (CH_2): It was used to produce the (p, 2p) reactions. As an alternative a liquid Hydrogen target can be used, but it was not possible at this experiment. It was 922 mg/cm^2
- Carbon (C): In order to extract the carbon contribution from the polyethylene target, some runs with a Carbon target were done. It was 935 mg/cm^2
- Lead (Pb): This heavy target was necessary for the Coulomb excitation part of the experiment. It was 2145 mg/cm^2

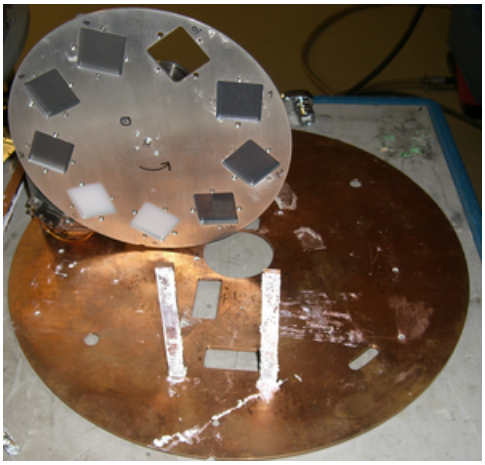

Figure 2.9: Target wheel picture taken before being installed for an experiment.

DSSDs

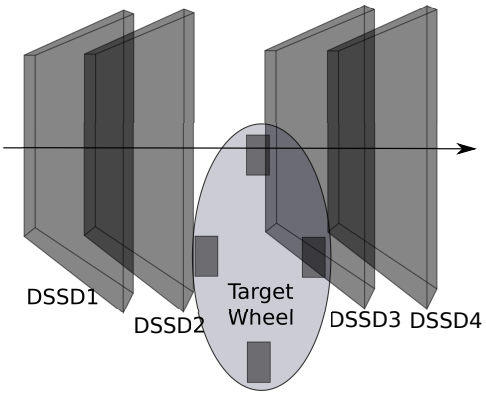

Figure 2.10: DSSD disposition around the target wheel. An scheme of the four working silicons detectors in-beam close to the target. There were four more boxing the target wheel, although as they failed to work in the experiment they have not been included.

The Double-Sided Silicon Strip Detectors (DSSDs) box is composed of 8 micro-stripped silicon detectors with the main objective of tracking the beam before and after the reaction and the protons coming out from the (p, 2p) reactions, as the energies involved are high the isotopes goes very forward-oriented, thus high resolution and segmentation is needed.

The orientation of the different detectors is shown in the figure 2.10.

The four off-beam silicons failed to work properly during the experiment so are not used neither on this work nor in any of the of the analysis of this experiment, so from now on I will only focus on the four on-beam silicon detectors that actually were capable to produce results.

Each of the silicon sensors is 72x40 mm^2 and 0.3 mm thick. Every sensor has an implantation pitch on the junction side (S-side or p-side) of the sensor of 27.5 μm with a corresponding readout pitch of 110 μm, therefore every four strip is connected to a single readout channel whereas the others are left floating. Those strips are capacitative coupled, which allow to improve the resolution getting information from them. The K-side(n-side) of the sensor has an readout pitch of 104 μm in this case every strip is readout. The result is 640 strips on the S-side(X) and 384 on the K-side(Y) for a total of 1024 channels in each detector. The angular resolution that can be obtained is close to 1 mrad . These detectors are slow to digitize all the channels every event, with times in the order of μs.

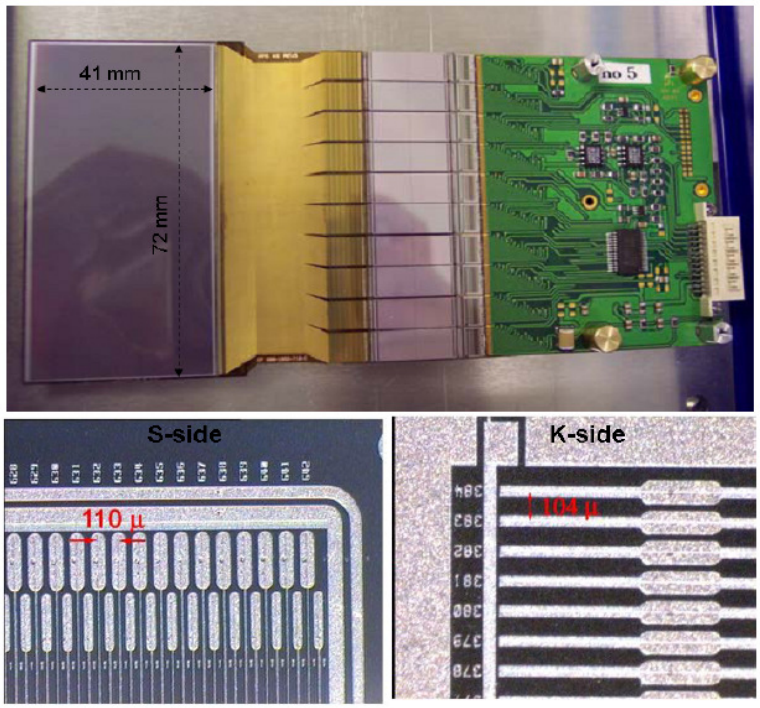

Figure 2.11: Photograph of a Micro-Stripped Double Sided Silicon Detector (DSSD), showing the 0.3 mm thick sensor and with two pictures zoomed to the readout area, indicating the readout pitch which is 110 μ and 104 μm for the S-side and K-side respectively. Image taken from [50].

Crystal Ball

Covering the target and the silicon box, there is a sphere of 162 NaI scintillator crystals assembly called Crystal Ball with an inner radius of 25 cm and a crystal length of 20 cm (see figure 2.12). Such a geometry follow the requirement of covering the same solid angle of 77 msr with every crystal, in order to achieve this target, four different crystals shapes are used: Regular pentagon (12), and three kinds of hexagons (60+60+33).

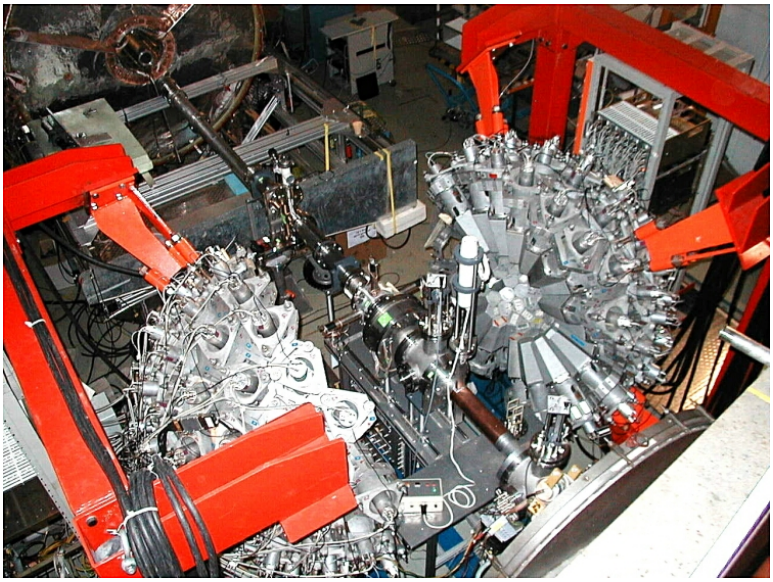

Figure 2.12: Photograph of Crystal Ball opened. There are two different holders for each side of the ball, so it can be kept completely opened in order to work close to the target. When the ball is closed up most of the 4π of solid angle is covered except from three crystals, one in the bottom for the target holder and two for the beam pipe coming in and out.

This detector has two main pourposes: Detection of the gamma-rays emitted from the nuclear reaction produced in the target, and detection of the protons knocked out from it, specially for the (p, 2p) reactions.

The realtively high segmentation of Crystal Ball permits to perform Doppler correction for the relativistic high energy beam gammas emitted in-flight from fragments moving at the speed of light. In order to be able to detect the high energy protons with the same scintillator crystals where the gammas are detected the readout of the most forward oriented photomultipliers was modified. 64 of the PMTs had two readout, one for the dinode as usual, and another one in the anode with less amplification allowing to record the energy loss up to 274 MeV protons, otherwise this high energy particles would have just saturated the readout.

ALADIN

Approximately two meter away downstream of the Crystal Ball, the most important "member"of the R3B setup is found, the A Large Acceptance DIpole magNet (ALADIN). It purpose is bending the reaction products to the three different branches of detectors with an angular acceptance of $\pm$ 60 mrad and a maximum magnetic field strength of about 1.5 T. However for the utilization of the magnet the used unity is the current which can go up to 2500 A but after 1900 A the correlation between the field strength and the current becomes nonlinear.

2.3.3 Outgoing fragment detectors

Proton Branch

The most bended particles that came out from the reaction are the protons, so 30° from the forward direction two group of detectors where placed. Two drift chambers for tracking and one time of flight wall at the end of the branch. As the proton branch is not used for the analysis explained in this document, is not going to be detailed.

Fragment Branch: GFI

The called Fragment Branch is at an angle of 15° from the forward direction of the setup after the ALADIN magnet. The first detectors are two fiber detectors, the GFIs (Gross-Fiber detektor) used for tracking the fragments and identification of the different masses.

These detectors are 50x50 cm^2 consisting of 500 parallel fibers (see figure 2.13). Each fiber has 1x1 mm^2 and is coated by a material of lower refraction index in order to guide the light, and the cross-talk is avoided by an additional white coating between the neighbour fibers. The consequence of this covering is a reduction on the geometrical efficiency, going down slightly below 90%.

One end of the fibers have Position-Sensitive PhotoMultiplier (PSPM) for the identification of the hit fiber, and in the other end a common PMT is coupled in order to get timing information. The PSPM is a Hamamatsu R3941 with a rectangular photocathode of 64x58 mm^2 and 16 mesh-type dynodes, while the anode has a rectangular grid of 18 wires in the X direction and 16 wires in the Y having a distance of about 3.7 mm between them. In this way the charge distribution on the anode grid is correlated with the position of the light in the photocathode, using a mask as it is shown in the figure 2.13.

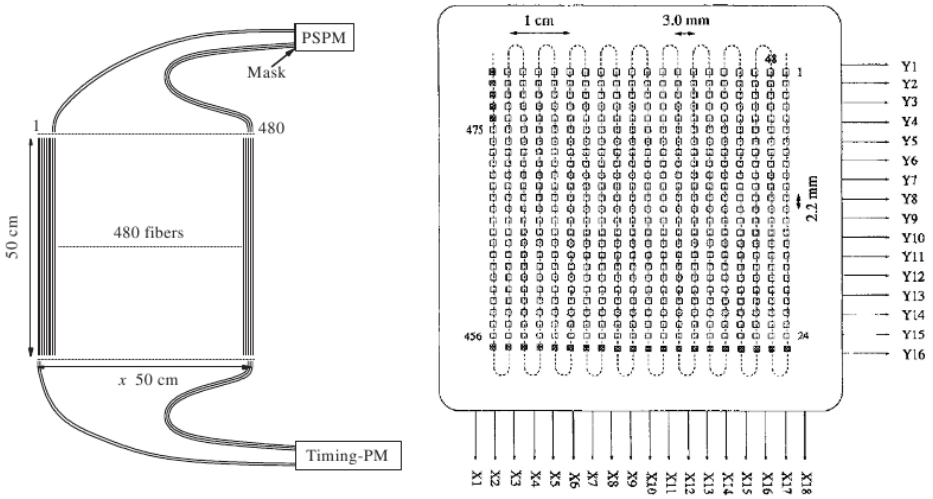

Figure 2.13: Schematic view of the GFI from [62]. The left picture has an scheme of the side of the GFI showing how the fibers and the PMTs are positioned and where the mask is as well. The second picture on the right, is the mask, showing the holes where the fibers are located and the coordinate system for the position correlation.Dark squares indicate unused holes and the relative position of the anode wires are indicated as well.

Fragment Branch: TFW

At the end of the fragment branch there is a Time-of-flight wall (TFW) very similar to the one located in the proton branch. This detector just as it is named is used to get the start or stop for the time-of-flight measurementafter the reaction but it is also used as an energy loss detector able to identify charge differences of the coming fragments.

This wall is built on 32 plastic scintillators paddles of 5 mm depth, 18 are vertical with 10 cm width and length of 1.4 m, on the horizontal direction there are 14 paddles of the same width and 1.8 m of length. At both ends of the paddles are two PMTs able to detect the amount of scintillator light and the timing.

The interaction on the scintillation paddles produce light that goes in opposite directions through the paddle until reaching the photomultipliers on both ends. In order to extract the interaction information, meaning time, position and energy loss, some calculations have to be done.

The time detected on both paddles are given by the equations 2.5, where T is the absolute time of the interaction and C is the velocity of light in the paddle material.

$$t_1 = T + \frac{s_1}{C} \qquad\qquad t_2 = T + \frac{s_2}{C} \tag{2.5}$$

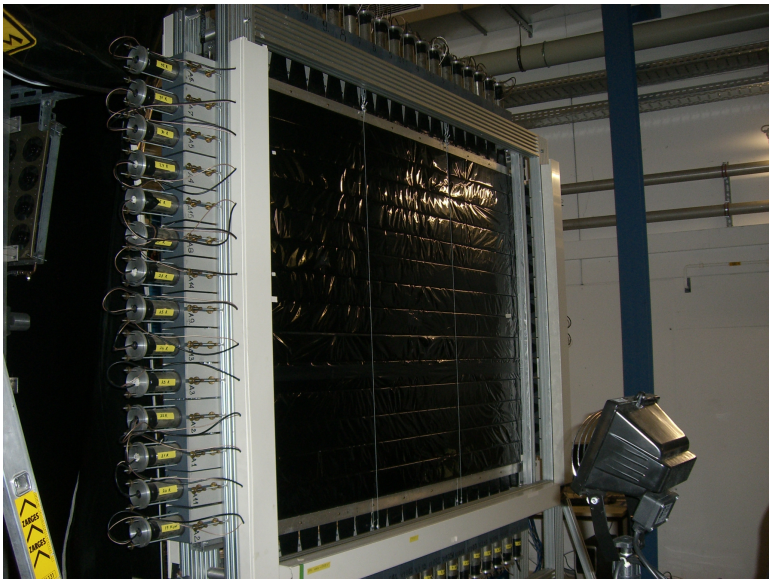

Figure 2.14: TFW picture from the setup of the s393 experiment. It can be seen the 18x14 paddle distribution and the PMTs on both ends of the paddles.The scintillator material is wrapped in black plastic in order to minimize the lost of scintillator light and the contamination from outside photons.

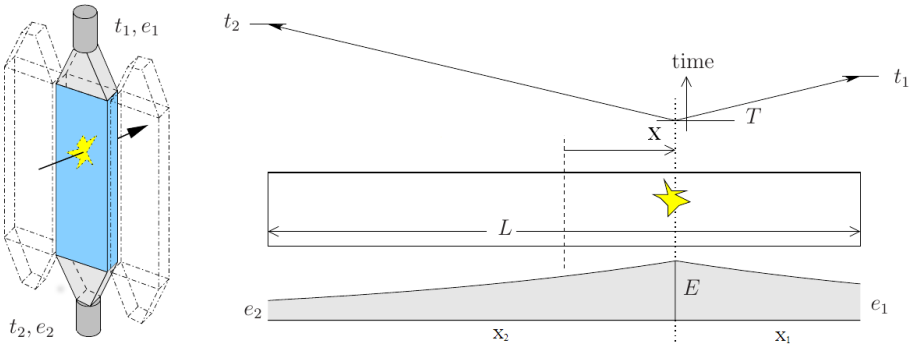

Figure 2.15: Schematic view of a TFW paddle and a drawing of the main interaction points and variables.E, X and T are the energy, position and time of the interaction, L is the longitude of the paddle, $x_{1,2}$ are the distance of the interaction from each PMT, $t_{1,2}$ are the times and $e_{1,2}$ the measured energy. Image taken from [63]

Summing both previous equations, the absolute time of the interaction is calculated by the equation 2.6, where L is the length of the paddle and $x_{1,2}$ are the distance the light goes through which are related following $L = x_1 + x_2$. The constants L and C can be treated as mere offsets for the calibration.

$$T = \frac{t_1 + t_2}{2} - \frac{x_1 + x_2}{2C} = \frac{1}{2}(t_1 + t_2 - \frac{L}{C}) \simeq \frac{1}{2}(t_1 + t_2) \tag{2.6}$$

The position of the interaction can be calculated just using the time difference of both signals like it is shown in the equation 2.7, where λ is the attenuation length.

$$X = \frac{1}{2}[(x_1 - \frac{L}{2}) + (\frac{L}{2} - x_2)] = \frac{C(t_1 - T) - C(t_2 - T)}{2} = \frac{C}{2}(t_1 - t_2) = CT \tag{2.7}$$

For the energy loss,the light attenuation of the paddles have to be taken into account with the equations 2.8

$$e_i = E \cdot e^{-\frac{x_i}{\lambda}} \qquad\qquad i = 1, 2 \tag{2.8}$$

Those equations allow us to reach the equation 2.9 where the parameter $e^{\frac{L}{2\lambda}}$ can also be taken as a constant and is moved to the gain in the calibration.

$$E = \sqrt{e_1 e_2 \cdot e^{\frac{x_1}{\lambda} + \frac{x_2}{\lambda}}} = \sqrt{e_1 e_2} \cdot e^{\frac{L}{2\lambda}} \simeq \sqrt{e_1 e_2} \tag{2.9}$$

This equation are applied for all the scintillator paddles based detectors of the setup like POS and LAND.

Neutron Branch: LAND

The Large Area Neutron Detector (LAND) [64] is the only detector of the neutron branch, located 13 meters away straight from the target center. The full detector is 2x2 m^2 with 1 m depth (see figure 2.16), it was designed to measure time of flight and position of fast neutrons with energies above 150 MeV , giving excellent three momentum resolution.

LAND consists on 200 paddles, each covering an area of 200x10 cm^2 with 10 cm depth an example paddle can be seen in figure 2.17. Each paddle has a sandwich structure with 11 sheets of iron (the two outer ones are 2.5 mm thick, the others are twice that thickness) and 10 scintillator plastic sheets of 5 mm thick. The detector is divided in 10 layers, each with 20 paddles. Every layer is perpendicular to the adjacent (see again figure 2.16), in such a way that it is possible to determine the vertical and horizontal position by the detection of the scintillation light. The paddles are equipped with strip guides wich direct the light to the PMTs in both sides and using

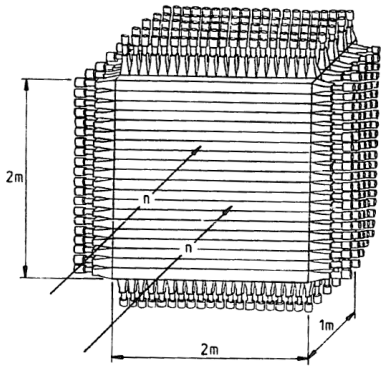

Figure 2.16: Schematic view of the detector. As it is explained in the text, there are 10 layers all of them perpendicular to their adjacent, every layer is equipped with 20 paddles.

the difference in arrival time of the signals the particle hit position within the paddle is determined.

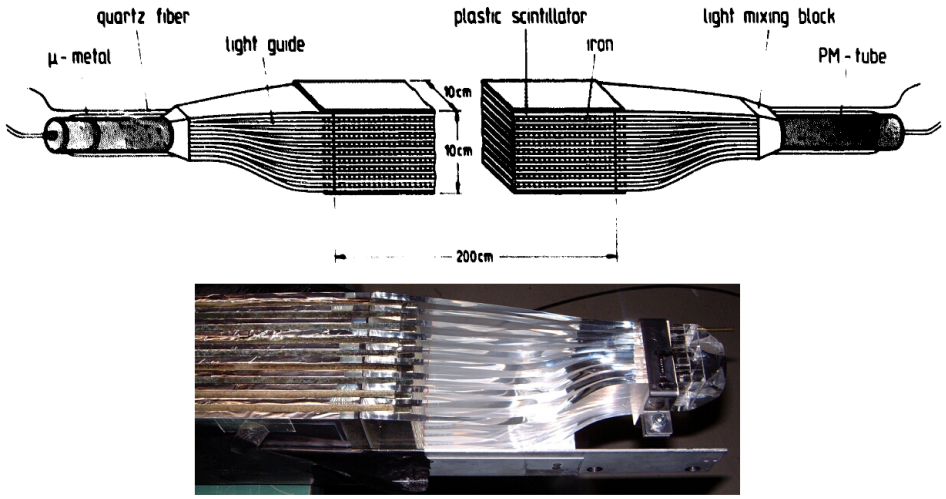

Figure 2.17: On the top there is a scheme of the sandwich structure of one paddle, showing the plastic and iron layers. The bottom picture is a photograph of the sandwich.

Often a VETO detector is setup in front of LAND in order to reject charged particles before reaching the neutron detector, but this was not used in the case of the S393 experiment.

"You'll find truth in your looking glass, not on the tongues of men "
George RR Martin, A feast for crows

3 Detector calibrations

In nuclear physics experiments the data is usually organized following the so called *events*. This is the set of physical phenomena and detectors signals produced within the time window opened by one accelerated isotope upon entering the setup. The data acquisition modules produce signals coded as bits that are stored together with the label-channel information that are preceded by the module identification. All this data from every module is packed with a unique identification per event. Thus the collection of thousands of this data packs make up usually the ListMode Data (lmd) files.

The signals produced in the detectors described in the previous chapter are processed and recorded using a Data AcQuisition system (DAQ) known as Multi Branch System (MBS) designed originally by Nicolaus Kurz et al [65]. This framework used at several facilities was developed at GSI. It main task is mapping the memory in order to access the different data acquisition modules of the electronic setup and handle the trigger synchronization of the different detector systems, as well as combining these different data into *events*. As a result the data is saved in lmd files of size close to 1 Gb.

3.1 Introduction to Land02

In order to describe the analysis procedure of a R3B experiment is impossible to avoid mentioning land02 [66]. Land02 is the software package used by the collaboration for calibration and data analysis of the GSI experiments. It was originally developed by Håkan T. Johansson but it has been extended and supported by a lot of members of the collaboration, primarily by Ralf Plag.

Land02 consists in a group of individual programs that guide the data from the lmd files collected by the acquisition program through the calibration of the different detectors in Cave C until the particles are tracked through the setup at the end of the process.

Figure 3.1 shows a flow chart of the stages the data follows under the analysis of an experiment.

- **lmd**

  As explained before, the data coming from the data acquisition is compressed in lmd files containing the information delivered by every module per event.

- **raw**

  The raw data is here understood as the first step after the unpacking of the lmd file, thus it is the same data but in read-friendly way for a specific analysis program, in this case the ROOT Data Analysis Framework [67].

- **tcal**

  This is the first level of calibration of every detector system where an initial internal time-calibration has been performed and the base line of the signal is settled, for instance subtracting the pedestals in the relevant detector channel.

- **sync**

  After this second-level of calibration the data starts to reflect the physics. All the time signals are related to a common zero and the corresponding gain is assigned to each energy channel.

- **dhit**

  This calibration stage is where the hits on the detector are physically mapped in space using the detector internal coordinate system.

- **hit**

  The hit positions are translated to a common unit with the origin usually selected as the center of the detector where the beam goes through in the ideal case of a perfect alignment, therefore the calibration can contain positive as well as negative lengths.

  It is important to emphasize that in land02 every detector is finally calibrated using the same units, nano-seconds (ns), centimeters (cm) and Megaelectron Volts(MeV) for time, distance and energy respectively.

- **track**

  This is the higher level of data treatment, where the correlation between the different detectors of the setup is settled and some physical values are calculated directly from the combination of them, like the Atomic Mass (A) or the Atomic Number (Z) as determined by the Time of Flight and energy loss in the incoming detectors.

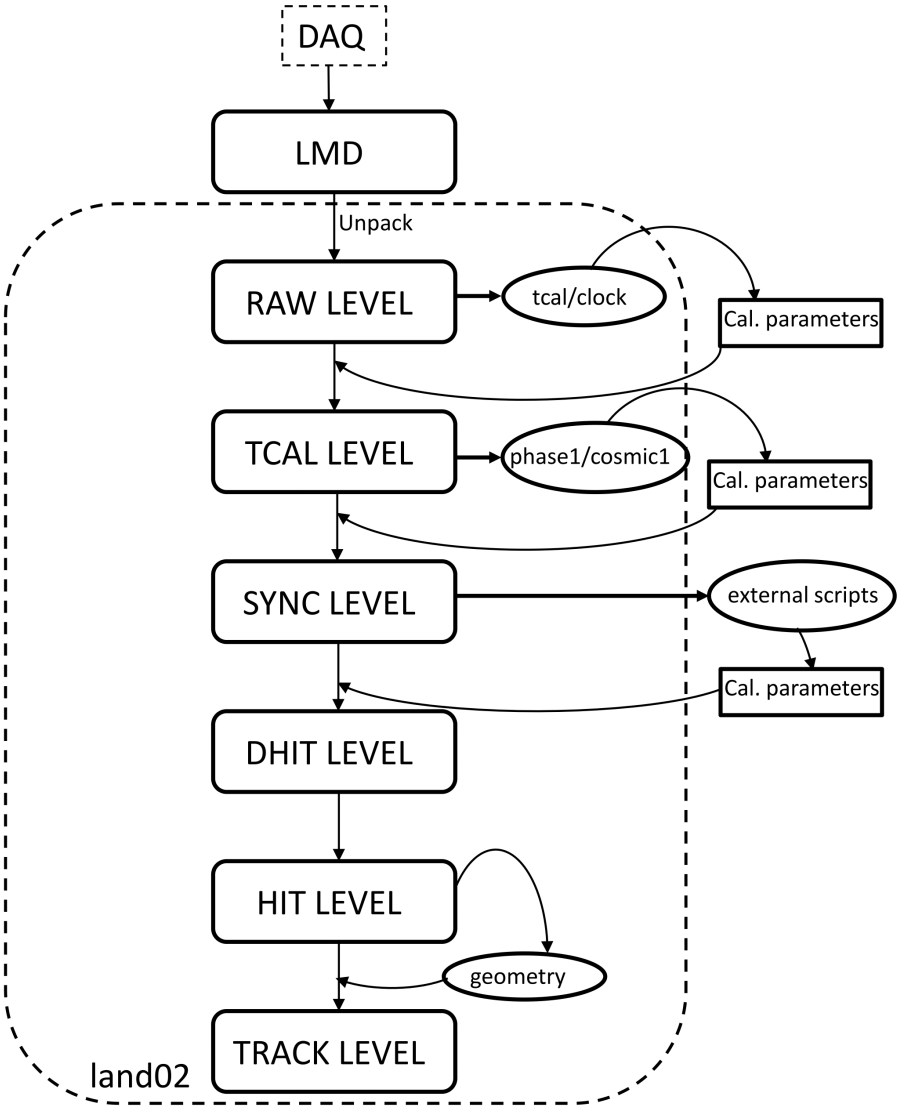

Figure 3.1: Flow chart of the different Land02 data levels (see text for further explanation). The connection between the calibration parameters and the land02 scripts used for calibration is detailed.

3.2 General points about calibrating with land02

The first and most important program to get a good calibration is of course, the unpacker, named *paw_ntuple* in Land02 for historical reasons. It allows to unpack the data in the previously explained calibration levels, reading the parameters and producing calibrated ROOT[67] files ready to be analyzed.

Is important to stress that in an experiment like the S393 which lasts several weeks the calibration parameters can change throughout the experiment very easily due to temperature and humidity variations, also because there were six different fragment separator settings, therefore several parameters associated with specific detectors like the amplification stages had to be changed accordingly. The function LT_RANGE is used to flag the parameters to be used for a certain collection of lmd data files.

3.3 Triggers

In experimental nuclear physics, a "trigger" is usually a system of logical signals used to activate the data acquisition to record the signals produced within that event. It can be quite simple, from just recording every signal above certain threshold, to a very complex system that includes several conditions on every detector. Because of the size of the setup and the broad range of research topics to study, in this kind experiment the trigger system is of the latter kind, allowing to change the priorities according to the beam time and the setting.

The logical signals are combined to produce a trigger pattern (Tpat) which consist in 16 bits of data which is added to every event in order to be able to classify it following the conditions that were fulfilled. Some triggers are fired more often than others, this would lead to an excess of redundant data, that is why it is usual to downscale these triggers, saving data space. As an example, if a trigger is downscaled by 64, one every 64 events meeting just that trigger conditions, would be recorded.

The s393 experiment used the trigger pattern of table 3.1. The basic Tpat is called "Minimum bias" and fulfill the conditions of "Good Beam" i.e. coincidence of Spill On (incoming of a spill from the accelerator), a signal in POS and anti-coincidence with a ROLU signal (POS.!ROLU), meaning that centered beam is coming in. The Good Beam conditions are used very often in coincidence with a signal in the Fragment Wall(TFW), therefore having a centered beam reaching the end of the setup, named as Fragment Tpat in table 3.1. All the Tpat with an anti-coincidence with the Spill On signal are used for calibration (cosmic rays). The Id is related with the bit number (n) saved to the lmd file with Id = 2^{n-1}.

Id	Tpat \Raw signal	trloctrl tracer	late-trigger kill	Early pile-up	Spill on	CB L+R	NTF	pix	S8	CB sum delayed	CB sum	CB OR delayed	CB OR	proton wall delayed	proton wall	fragment wall delayed	fragment wall	land cosm	land mult	POS	POS.IROLU
1	Minimum bias Good Beam(GB)				■																■
2	Fragment GB + TFW			■	■												■				■
4	FRS S8 Hit end FRS				■				■												
8	CBSUM Fragment + CB Energy		■	■	■						■						■				■
16	Proton Fragment + DTF			■	■										■		■				■
32	GB-pileup Discard Pile-up			■	■																■
64	Pix GB + pix for calibration				■			■													■
128	Neutron GB + TFW + hit in LAND			■	■												■		■		■
256	CB muon No Beam + CB high energy				■					■											■
512	Land Cosm No Beam + hit in LAND				■													■			■
1024	TFW Cosm No Beam + TFW				■											■					■
2048	CB Gamma No Beam + CB				■							■									■
4096	DTF Cosm No Beam + DTF				■									■							■
8192	NTF Cosm No Beam + NTF				■		■														■
16384	CB L+R muon No Beam + CB both sides				■	■															■

Table 3.1: Relationship between the raw trigger signals (horizontal order) and the trigger patterns (vertical order) in the s393 experiment. The green squares means a coincidence signal and red squares an anti-coincidence signal.

3.4 Raw → TCAL

Most of the detectors of the setup use a QDC (Charge to Digital Converter) at the end of their electronic chain. Whenever the timing gate is open the voltage on an internal condenser is integrated to produce a digital value that is recorded. This capacitor is charged by the signal from the detector and a little current supplied by the QDC, thus the read value will always have a certain off-set produced by the module called Pedestal. In order to go from the raw level to the TCAL pedestals must be subtracted. Land02 have a script called *clock* which goes through off-spill data looking for a certain time trigger (clock) coming in regular intervals. The recurrent size of the signal in that kind of events is subtracted in every channel. The Crystal Ball modules are different and instead of using the *clock* program, the pedestals are calculated using a known source run. As a result of this calibration, all channels within a detector have the same base line (zero) value.

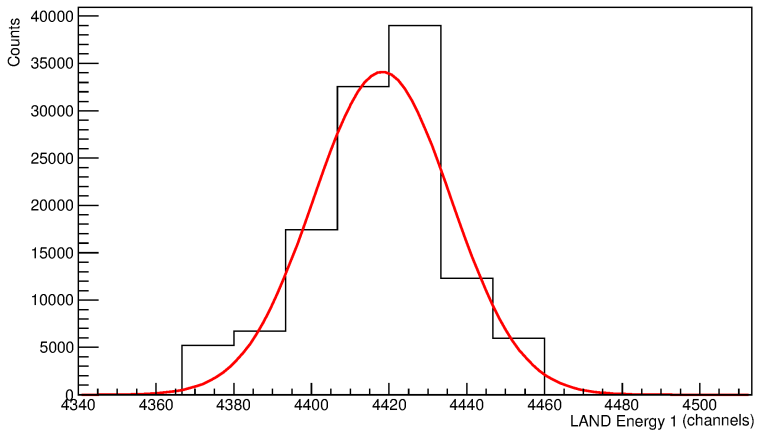

Figure 3.2: Standard pedestal fitted by the *clock* program on one of the PMTs signals from LAND. Looking at the coincidences with the clock trigger signal is obtained the pedestal signal position that must be subtracted. It is fitted to a Gaussian function to get the mean position value.

Also the time calibration within the detector is performed in this level. The TDC (Time to Digital Converter) have a certain gain value which can change along the time of the experiment, thus it have to be measured at different moments using a time calibration module. This module send two delayed signals, one to the DAQ and another to all the electronic channels, hence recording such events allow us to keep on check the gain of each module. *tcal* program in Land02 goes over the raw data and produce a correction factor for the time signal. This calibration leaves all time correlated

within the detectors and in the common unit of nano-seconds, although every detector time is still uncorrelated with the global time of the setup. Further information can be found in [68][69].

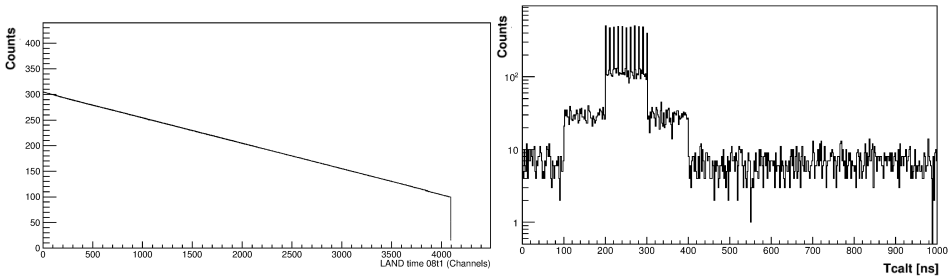

Figure 3.3: *Left:* Standard calibration plot of the *tcal* program. The correlation of the tcal time with the time measurements from one LAND PMT can be seen. *Right:* Typical output from the time calibrator. It has to cover the TDC range of all detectors that require calibration.

3.5 Incoming beam identification calibration

What is usually understood as the "incoming "detectors consist in the PSP, POS and S8 (see section 2.3.1). These detectors give Particle IDentification by charge and time of flight measurement of the the incoming beam.

The PSP usually provides energy loss and position information. Unfortunately the latter was not possible in the s393 experiment due to the lack of calibration runs (called "Pixel runs"). This kind of detector require the use of an active mask with a grid of hundreds of small square pixels that allows to have a reference for position calibration, but the amount of data with the pixel mask on was too low. The PSP have certain position dependency of the energy deposition, that could not be corrected due to the lack of statistics, however the resolution of the mass/charge ratio is enough for a good separation of the incoming beam.

The energy loss is provided by the cathode in the detector that can be calibrated using several different ions (different energy losses) by fitting the data to Gaussian (see figure 3.4). The energy values corresponding to each curve can be estimated using ATIMA (or similar program). The channel and the energy loss values are correlated using a linear fit, providing slope and offset as parameters. Therefore each channel is directly related to a certain energy loss value, which corresponds to a certain charge Z.

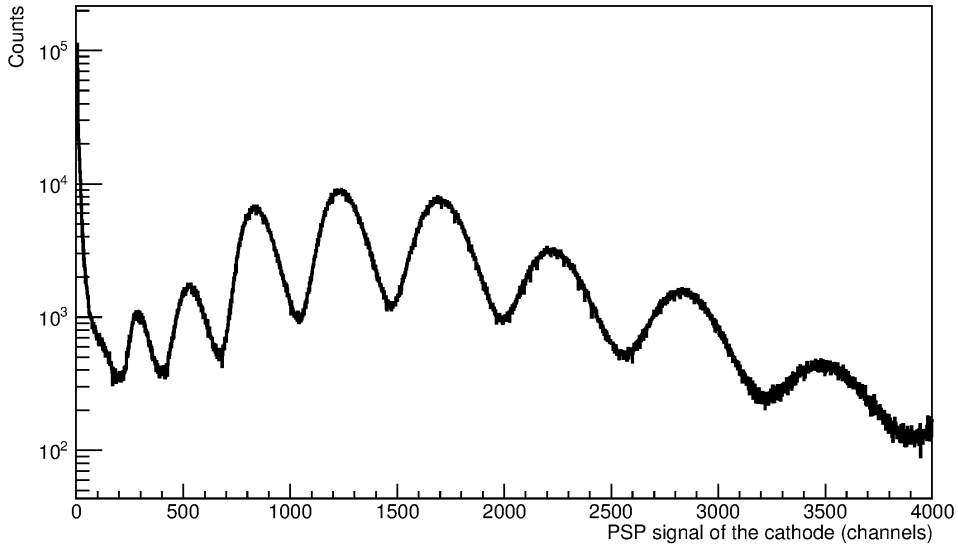

Figure 3.4: Different energy loss deposition in PSP detector of nuclei with different Z. Each peak is fitted to a Gaussian function to get a mean for the value of the energy loss for every isotope (which can be correlated to a certain charge Z).

The scintillators S8 and POS, provide the time of flight for the ion identification.

$$\beta = \frac{\Delta X_{FlightPath}}{c \cdot ToF} \tag{3.1}$$

The equation 3.1 shows the relationship between the beta (β), flight path ($\Delta X_{FlightPath}$) and Time of Flight (ToF) of an isotope. The equation 3.2 is the time difference between S8 and POS which is the result of the time of flight and the electronics involved.

$$\Delta T = ToF + T_{offset} \tag{3.2}$$

Combining these equations results in 3.3, thus making a linear fit of the time difference (ΔT) against the velocity (β), it is obtained the time offset and the flightpath which is considered as a parameter of the fit. The velocity of the incoming isotopes can be calculated from the beam energy using the SHARP calculator ([70]).

$$\beta \cdot \Delta T = \frac{\Delta X_{FlightPath}}{c} + \beta \cdot T_{offset} \tag{3.3}$$

Once the charge and the flight path are calibrated, it must be related to the mass/charge ratio for particle identification. This is done with the

equation 3.4, calculating the Bρ with the SHARP calculator. The result can be seen in figure 3.5.

$$\frac{A}{Z} = K \cdot \frac{B\rho}{\beta\gamma} \tag{3.4}$$

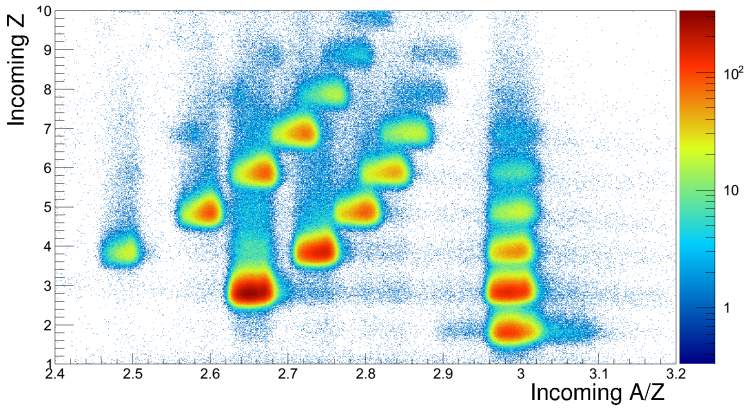

Figure 3.5: Example of Particle Identification for the setting 5. The Y axis holds the charge(Z) of the incoming nuclei whereas the X axis represents the mass/charge (A/Z) ratio of that nuclei.

3.6 Calibration of the detectors around the target

3.6.1 Double Sided Silicon Strip Detectors (DSSDs)

Due to the importance of measuring the outgoing angle of the fragment, the position calibration of the Double Sided Silicon Strip Detectors (DSSDs) is crucial in this research. The calibration from the TCAL level to the HIT level has been performed with some routines made by Valerii Panin and Matthias Holl, hence a more detailed explanation can be found in their respective Thesis [50][51]. This calibration is very charge dependent, thus the Z of the isotope of interest must be previously selected by the incoming detectors, and an empty run or the non-reaction part of the beam have to be used in order to calibrate the silicons located after the target.

The energy signal of a particle punching through the DSSD is shared over several neighbour strips. A Carbon nuclei activate an average of 5.4 strips on the K-Side and 8.3 on the S-Side. Therefore the positions and energy of these detectors is driven by clusters of neighbour strips with signals over a certain threshold.

In order to assign a position to a cluster, it is calculated using a center-of-gravity approach, weighting with the energy signal in every strip,

$$X_{cog} = \frac{\sum_{i}^{k} E_i n_i}{\sum_{i}^{k} E_i}. \tag{3.5}$$

In the equation 3.5 n_i is the strip number and E_i the energy signal, and the sum goes through all the strips of the cluster $\{i...k\}$. That determination of the position within a cluster permits to calculate a position in the detector with the equation 3.6,

$$X = P \cdot X_{cog} \tag{3.6}$$

Where P is the value of the readout pitch size, 110μm and 104μm for the S-Side and the K-Side.

This method produces positions distributions with obvious patterns favouring the positions of the strips in the center of the clusters. This affect no only to the measured positions but the energy as well. In order to avoid this effect, an impact parameter η is defined (see equation 3.7) to represent the inter-strip signal distribution. The $Integer(X_{cog})$ value usually is the number of the central strip of the cluster, therefore if η=0 the hit is in the central strip, while with η=1 is in the next strip with a readout. Hence this parameter allow us to represent the inter-strip area for both S- and K-side of the DSSD.

$$\eta = X_{cog} - Integer(X_{cog}) \tag{3.7}$$

In order to correct the position to have a continuous distribution in the inter-strip region the distribution of the η parameter must be integrated using the equation 3.8,

$$X_N = Integer(X_{cog}) + P \int_{0}^{k} f(\eta) d\eta. \tag{3.8}$$

The change from a pre-smoothering of the η parameter to the result after the integration can be seen in figure 3.6.

Every broken or wrongly coupled strip will continuously fire a signal or not deliver it, thus the strip has to be flagged as "dead"and not included in the calibration in order to avoid miss-identification of the clusters.

After the position calibration is finished, a similar approach has to be follow in order to correct for the gainmatching of the clusters. The gain in every strip is different, so every cluster energy-distribution is divided in three bins and fitted to a Gaussian function for correction. The energy is

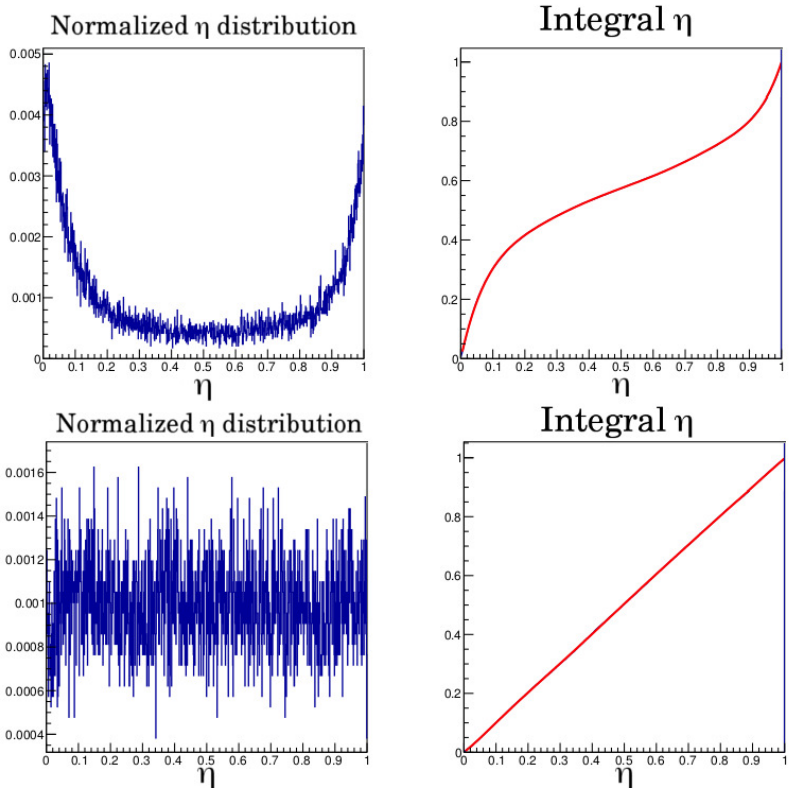

Figure 3.6: (a) η Distribution before calibration. It can be easily seen that the values where η=0,1 are clearly favoured because is where the real strips readout are located. (b) Result after the integration, the distribution is continuous and smooth. Is important to notice the very small range of the Y axis in the left plot, it is showing a very flat η distribution.

also gainmatched to a certain value thus all the clusters within a K-side/S-side have the same energy value. The energy resolution for Boron is around 7%.

3.6.2 Crystal Ball (XB)

The calibration of the Crystal Ball is divided in two separate branches, due to the fact that the pulses coming from the forward crystals are split in two signals for different amplification stages in order to fulfill the different dynamic range of gamma-rays and protons.

Source	Calibration peaks
^{60}Co	1173 keV
	1332 keV
^{22}Na	511 keV
	1275 keV
^{56}Co	2598 keV
	3253 keV

Table 3.2: The three different standard sources used for the calibration. ^{60}Co and ^{22}Na sources were used in the s393 experiment but the ^{56}Co was used in the following experiment s389. For the ^{56}Co is only detailed the used peaks.

Gamma branch

Along the experiments we took advantage of the beam stops to make calibration runs with sources (see table 3.2) which are used to perform the energy calibration of the gamma branch. F. Wamers [49] developed several useful scripts to help in the process. To produce the energy calibration consists in seeking the identification peaks of each source (see figure 3.8) and making a linear fit to correlate the channels with the energies (see figure 3.9). Due to the fact that along the experiment the sources used were ^{60}Co and ^{22}Na the calibration is only reliable over a small region, thus it is complemented with the source ^{56}Co of the s389 experiment, carried out in October 2010 just after the s393. The prompt reaction gammas suffers an important Doppler correction due to the high beam energies, the consequence of this are the very different amplitude gains, determined by their position in the sphere. The most forward angles receive much higher energies than the backwards (see figure 3.7).

At the beginning of the analysis I developed my own gamma calibration using the two sources of the s393 experiment as it was reported in my Master Thesis [71]. Later on I have used the calibration performed by R.Thies for the experiment. The efficiency calibration of the detector is used in order to measure cross-sections, as it is not need in this work it was not included, although if more information is needed see reference [72].

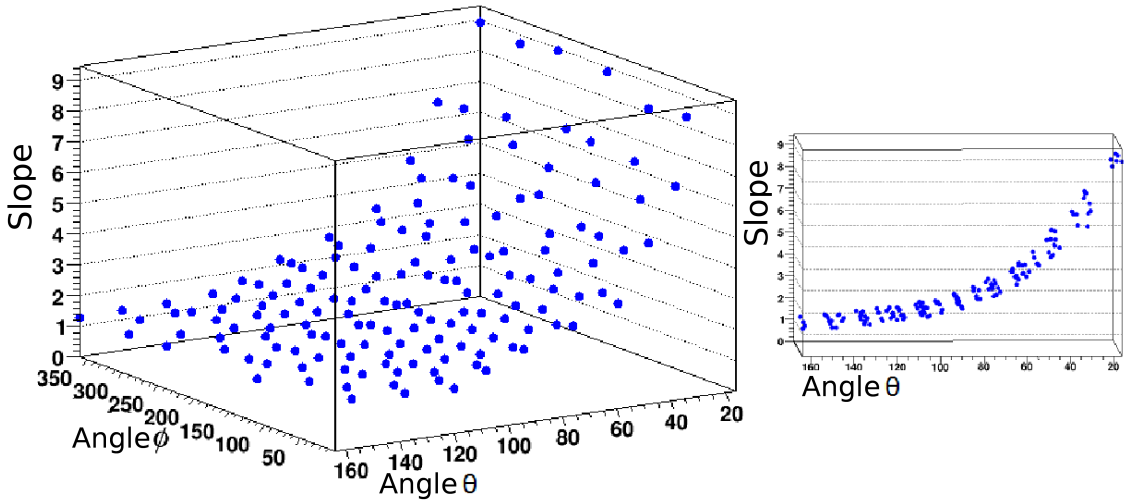

Figure 3.7: Calibration slope against the crystals angles. The slope grows when θ go down, because the scintillators in the forward angles (closer to 180°) will measure the highest energies.

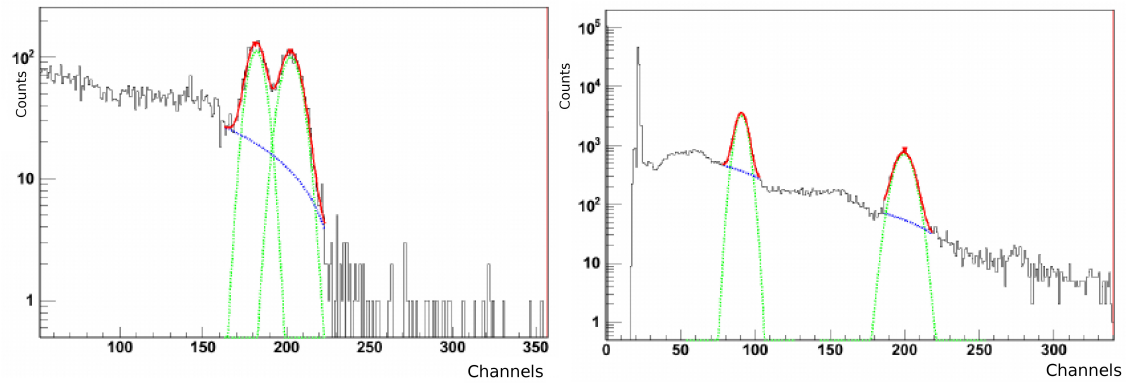

Figure 3.8: Calibration peaks for the crystal 42. (a) Using ^{60}Co the energies are at 1173 and 1332 keV (b) Using ^{22}Na the energies are at 511 and 1275 keV.

Addback and Doppler correction for the gamma branch

Gamma rays have an important probability of leaving their energy in several Crystal Ball detectors, hence is needed to take into account this possibility and include an Addback algorithm to improve the detection efficiency. The algorithm used is the "closer-neighbours algorithm"(see figure

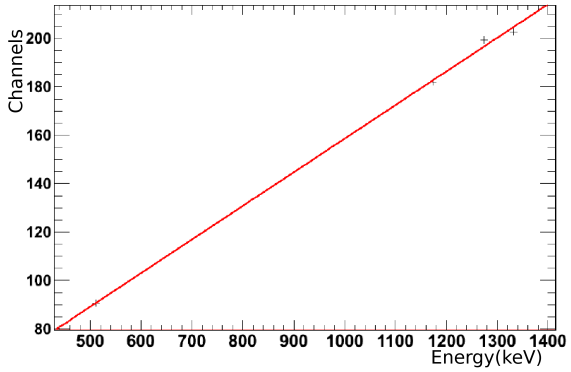

Figure 3.9: Linear fit to correlate channels with energy for the Crystal Ball

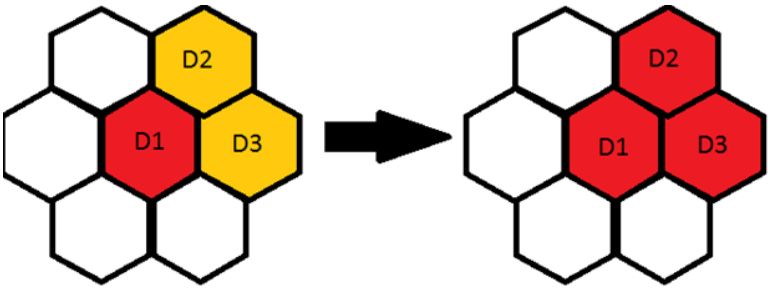

Figure 3.10: Closer-neighbour algorithm. After sorting and ordering the crystals by the energy in an event, starting with the highest (D1), the energy deposited in the surrounding crystals is added making a cluster. All crystals of the cluster are taken away from the crystal lists, and starts again with the following. The angle used for the Doppler correction is from the detector which starts the cluster.

3.10), there are other several options, but none of them have proven to be better[73].

The last step before being able to analyze the gamma data from the Crystal Ball is applying a Doppler correction to every event in each crystal. It is determined by the equation 3.9, where β is the ratio of the isotope velocity in middle of the target and the light speed, γ is the Lorentz factor and $\theta_{crystal}$ angle is from the cluster. This correction can be applied after the DHIT calibration level.

$$E_{CM} = E_{lab} \cdot \gamma(1 - \beta \cdot cos\theta_{crystal}) \tag{3.9}$$

Due to the Doppler boost the gamma energies can reach up to 15 MeV but the source peaks used in the calibration are at 2.5 MeV maximum, thus

the calibration procedure could be largely improved.

Proton branch

This branch is crucial for the detection of the knock-out protons from the (p, 2p) reaction. The calibration was performed by Ronja Thies.

Muons and protons have very similar masses and the same absolute charge, therefore they have a similar energy deposition, thus this calibration is performed using cosmic muons from the atmosphere. A land02 program named *gamma2* is used to look for two different kinds of trajectories: (a) Across two opposite crystals and (b) Crossing the shell, going through several crystals. The atmospheric muons have enormous energies, hence as charged particles are in the low-loss energy regime (not reaching the Bragg peak), the simulations [49] shows that in the (a) case you are sure of the direction so the muon goes through the full length of two crystals leading to an energy loss of 90 MeV, whereas for the (b) case the muon traverse sideways through the shell leading to 45 MeV energy deposit.

Using both different kinds of flight paths and their different energy loss, a linear fit is performed to correlate the channels and the energies of the 64 crystals with high energy regime in the PMTs. More information can be found in [74].

Time calibration

The internal time calibration in Crystal Ball uses the *gamma2* script as well. Event by event, it looks for two crystals that have detected the full energy of the two peaks from the sources ^{22}Na or ^{60}Co in the same event, as these gamma-ray pairs can be considered to be emitted at the same time, they are used to calibrate the time difference of the crystals. After collecting a considerable amount of statistics this time difference is fitted to a Gaussian curve in order to obtain a mean time difference. The obtained data is used to solve an equation system to get a time offset for every crystal such as all summed give zero. These offset provide the time correlation between all crystals times, afterwards the Crystal Ball is correlated with the full detector setup.

3.7 Calibration of the outgoing fragments detectors

3.7.1 Fiber Detectors (GFI)

In order to calibrate the GFI it is needed to perform a *sweep run*, in this kind of run the target is empty and the magnet current is changed continuously to illuminate the full area of the outgoing detectors. The GFIs are used to track the masses of the outgoing fragments, thus the energy

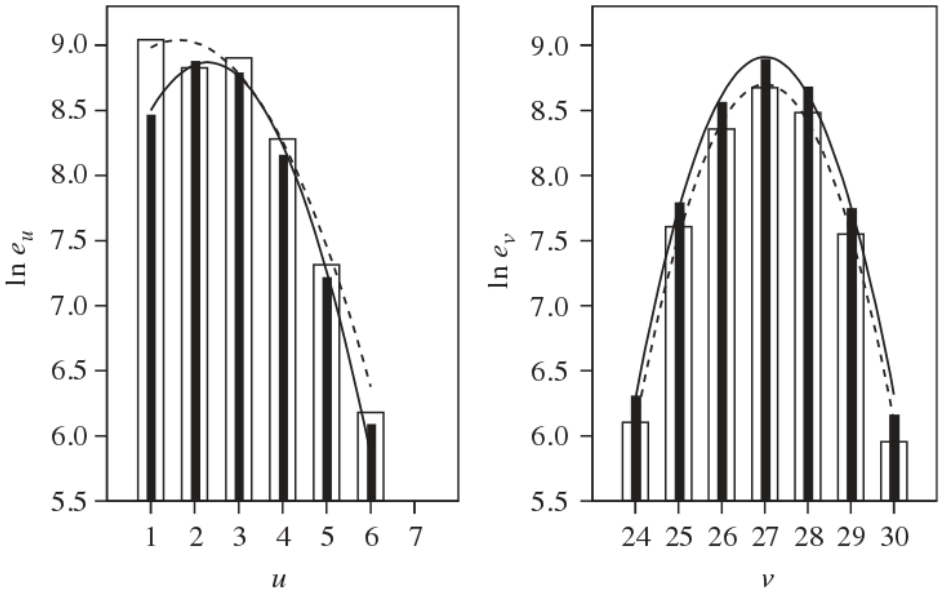

Figure 3.11: Example of charge distribution in the anode wires. The open and filled vertical bars are the electrical signal of each wire before and after gainmatching. The dotted and filled line are the fit functions, before and after gainmatching. Taken from [62].

loss is not necessary but the position, although due to the different gains of the anode wires is mandatory to gainmatch them before the position calibration. There are 34 wires, 18 in the horizontal direction (u) and 16 in the vertical direction (v). An isotope hitting the GFI produces scintillation light which is guided through the fibers to the Position-Sensitive-Photomultiplier (PSPM), generating electrical signals in around seven anode wires. Fitting the distribution to a function gives the gainmatching parameters (see figure 3.11). As the process includes resolving an equation system which starts from the best previous fit, it should be repeated usually around three times to get stable parameters (see figure 3.13).

The position calibration needs to correlate every fiber with a position in the PSPM coordinate system (u,v). To project the fiber signals into this coordinates, a two-dimensional histogram is used. Every cluster is fitted to a Gaussian distribution to provide a mean value (and the associated deviation) for the cluster position in the wires coordinate system. The next step is determining their neighbours which is done using the angles and lengths of the vectors of the grid, indexing this data to produce a grid which relates the fibers with their PSPM coordinates and the position of fiber in the detector (x). This grid easily assign signals to positions if the hit is within the width of a fiber (cluster), in such a case that a hit signal is between clusters,

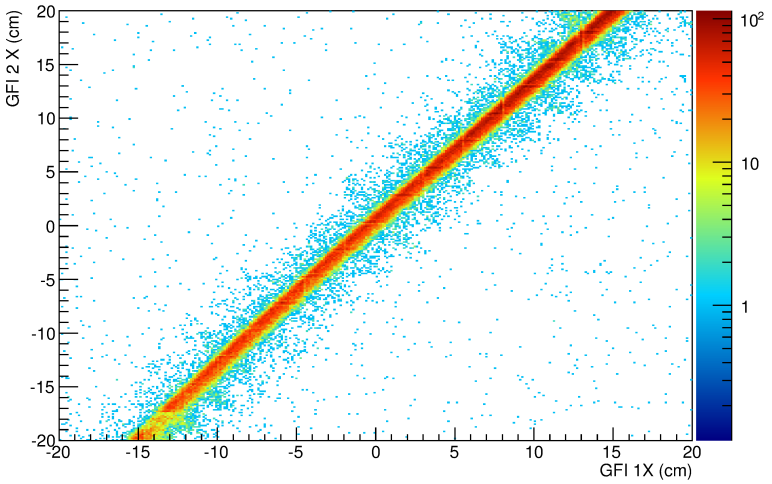

Figure 3.12: Correlation between the two GFI detectors in the experiment that were separated by 150 cm. Good correlation between the GFI 1 and GFI 2 is indicated by a straight line close to 45° and is a signature of good position resolution.

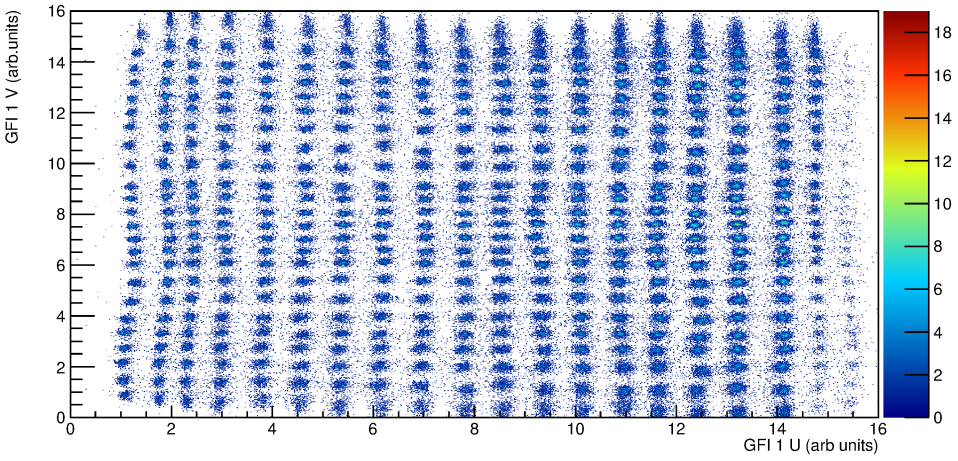

Figure 3.13: Calibration result of the GFI. Every point clusters represents one fiber, three iterations of gainmatching has been performed. All the clusters as well as the fiber mask boundary is good resolved and defined.

the probability of belong to one of them is calculated assigning different weights and including a randomization. For further details about the calibration see [62].

3.7.2 Time-of-Flight-Walls (TFW)

After have run the *clock* and *tcal* codes in order to reach the TCAL level, running the script *phase1* will gainmatch the PMT signals within the paddles and correct the time.

One goal is to synchronize the energy and time within every paddle, gathering an amount of "clean"data, just hitting one paddle in each plane, avoiding ambiguities. The data collected in each paddle is fitted such as the offset is zero in the middle. This produces the gainmatching for the energy and an offset for the time, as well as the speed of light within the paddle that is also needed for the position calculation.

In this kind of detector, there are two layers of scintillators, one to measure the Y direction and a second one the X direction, therefore there will be a small time and energy deviation between X - Y planes. As this difference in energy loss between them is negligible at this beam velocities, we can consider it to be equal. In the same way, the distance between the two layers is 1 cm, thus the time of flight difference is also insignificant in this case. Consequently, the other goal in the calibration is to synchronize the X and Y plane in order to have the same time signal and energy loss, producing a gain for the energy and an offset for the time.

Once the internal calibration of the detector is finished, correlate the measured energy and time with the real energy loss and the time of flight with the setup. Using such a program like ATIMA [75] it is possible to calculate the time of flight from the target and the energy loss of a chosen isotope upon reaching the TFW. These values are correlated to the mean values from previous steps of the calibration.

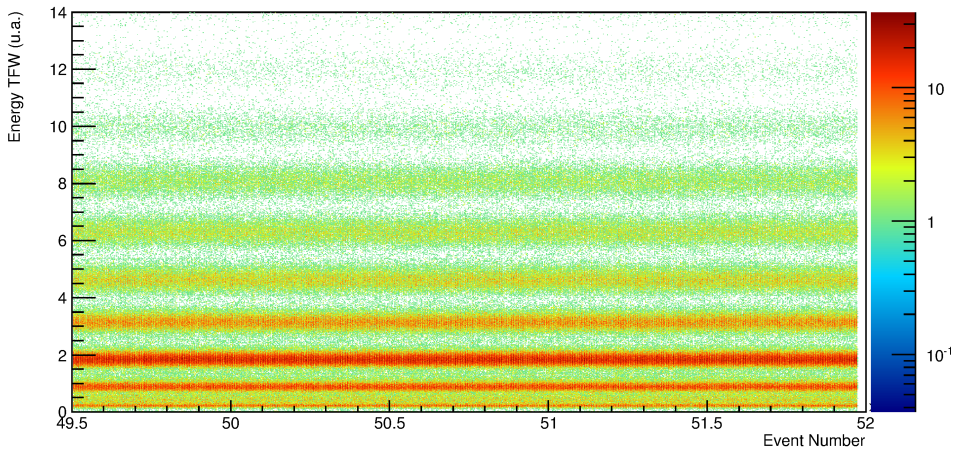

Figure 3.14: Time of flight wall after calibration. The different offsets in the gains of the energies has been match to have a smooth energy distribution over the events.

3.7.3 LAND

Calibrating LAND is very similar to calibrate the TFW, the neutron detector consists in several planes of sandwiched iron with plastic scintillator. Therefore, the procedure is similar, the energy signals within the paddle must be gainmatched as well as the time signals needs to be shifted to obtain a zero in the middle of the paddle. This calibration is performed using the script *cosmic1*, which uses cosmic muons like in the Crystal ball proton calibration. The useful events are particles coming from above with such a high energy to go through several scintillator planes. Obviously, is also required to synchronize the signals between the different planes.

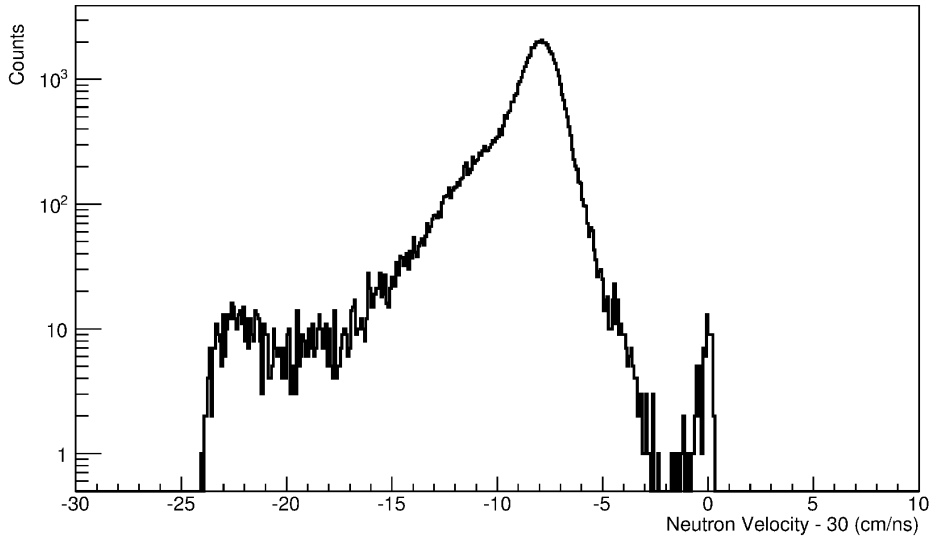

Figure 3.15: The gamma-rays peak is at the right-most part of figure. It is already calibrated to a velocity of 30 cm/ns.

In order to synchronize the time stamp of the detector with the time stamp of the full experimental setup, the gammas coming from reactions are used. Gamma rays travel with the same velocity (c), hence a certain peak at higher velocities than anything else can be easily find and used as a reference to complete the calibration (see figure 3.15).

3.8 Tracker

In order to complement land02, R.Plag has developed a tool[76] to track the particles, simply named *tracker*. The main objective of this is to have a good determination of the different masses of the isotopes after the reaction. The program uses root files with unpacked data at HIT or TRACK

level (see section 3.1), and produces a new root file, similar to the previous but with several new leafs.

The tracker approximates the trajectories of the different isotopes and fragments using several parameters as an input and extracts the masses of this isotopes thanks to the previously mentioned equation 3.4. To calculate the trajectory is necessary to know the ALADIN magnetic field, there is a mapping that relates the field with the current of the magnet, therefore providing the current used in a certain run allows the tracker to use the right value of B. The velocity is obtained from the Time of Flight (using TFW) and the flightpath with the corresponding energy loss of the fragment in every detector calculated with the Bethe-Bloch equation (2.2 equation. The charge must be specified too. The trajectories are determined using hits in the DSSD, the GFIs in the X direction and the TFW (mainly in the Y direction). The program can work on three different modes: forward tracking which needs two detectors before ALADIN and one after (DSSDs + GFI), backward tracking using two detectores after the magnet and one before (DSSD + GFIs) and mixed mode that uses two detectors in both sides of the setup. The most used method in this analysis was forward tracking. In this approach, the program calculates a track with fixed positions in two detectors before the magnet (DSSDs), presuming a mass and an initial velocity, it minimizes the trajectory changing the mass accordingly and correcting the β with the different energy loss.

The position of the detectors must be given and calibrated using empty runs or non-reacting beam, and once certain positions are determined, the ToF from the target to the TFW must be calibrated as well. The calibrations are basically performed by comparing the calculated tracks with the "real tracks"(hit positions) until reaching differences within the detector resolution limits.

The program have additional features, like tracking the protons through the proton branch which has not been used in this analysis. It is capable of tracking the incoming isotopes with the two DSSDs before the target and POS, although this have several problems in the s393 experiment because of the problems with the first silicon. The code tracker also calculates the Doppler correction using the β of the fragment (see section 3.6.2).

"...no matter how many instances of white swans we may have observed,
this does not justify the conclusion that all swans are white."
Karl Popper, The logic of scientific discovery

4 Analysis

In the previous chapters I was explaining the experimental setup used to study the nucleus of interest as well as the methods required to understand the detectors. In this chapter I will explain the techniques used for extracting the physical significance of the dataset from the s393 experiment.

The intention of this research work is to probe the nuclear structure of the unbound nuclei ^{13}Be using the reaction ^{14}B(p,2p)^{13}Be. The analysis include several steps. The first step to be done is the identification and separation of the incoming nuclei of interest ^{14}B. Secondly to select the right outgoing channel: ^{12}Be + neutron which is the result of the break up of the unbound isotope ^{13}Be. Determining the angle between these two components as well as their velocity provide us with the information required to produce a relative energy spectrum which gives insight to the system they composed before: ^{13}Be. Such a spectrum must be interpreted via fitting to Breit-Wigner functions, the basis will be explained in this chapter, whereas the results will be discussed in the chapter 5. The fragment ^{12}Be can be emitted with an internal energy excitation, knowing this information will help to know the previous state of the ^{13}Be, therefore looking for gammas-rays from ^{12}Be is the third step. The last step is looking for the two protons product of the (p, 2p) reaction to complete the analysis.

4.1 Incoming isotope identification

From the interaction between one nuclei of ^{40}Ar of the primary beam and the production target a broad variety of isotopes can emerge (see section 1.2). The purpose of the fragment separator is to throw out the species with too high charge to mass ratio for our interest (see section 2.2.4), although the selection of isotopes that reach the Cave C is extensive. As explained in the previous chapters, the PSP, S8 and POS are used to select the incoming nuclei.

The interesting projectile for this work is the nuclei ^{14}B that is present in three different FRS settings of the experiment s393, i.e., optimized to three distinct $\frac{A}{Z}$ ratios. The figure 4.1 is the isotope identification of the summed runs used for this analysis, the useful data is from two settings, the third have too low statistics of ^{14}B.

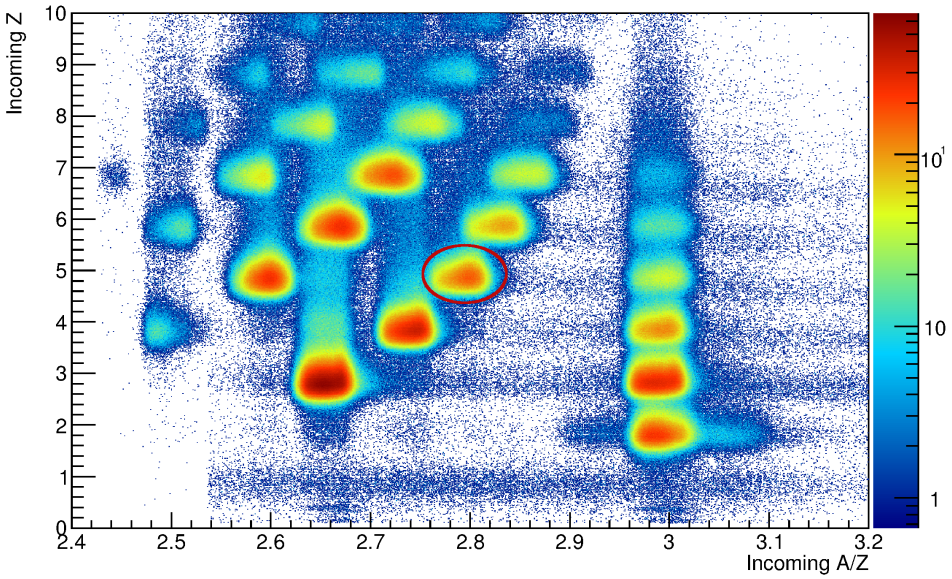

Figure 4.1: Fragment identification of the data files included in this analysis. The Y axis is the charge (Z) of the incoming isotopes whereas the X axis is the mass/charge(A/Z) ratio of them. This plot required TPat 2, i.e., Minimum bias and fragment trigger. Included data from two different settings (4 and 5) which have data of $\frac{A}{Z} \simeq 2.8$. corresponding to the nuclei $^{14}_{5}$B is the interesting incoming channel for this research work, therefore it must be gated on the corresponding blob, indicated by the red ellipse.

4.2 Detector alignment

In order to obtain the angle between the outgoing particles, all detectors involved have to be properly aligned, as it will be explained in the section 4.4. DSSD and LAND are the detectors used to measure the incoming and scattering angles of the particles outgoing from the reaction.

At the end of the experiment, photographs of the experimental setup were taken in order to perform a photogrammetric measurement which determine the detector positions very precisely, this provides the data needed for an alignment later on. In order to be able to take pictures inside of the Silicon Box (where the DSSD are located) they have to be taken very close by, therefore the accuracy reached for the DSSDs relative position by this method was 400μm much higher than for the other detectors. Further details about the used method can be found in [77].

A good position resolution does not guarantee that the origin of coordinates of the four silicon detectors have a good alignment. This was achieved fitting the coordinates of the silicons 2-3-4 to a straight-line, using data from empty runs (unreacted beam). The procedure minimizes the trajectories with three parameters, the coordinate X and Y and a rotation with the beam axis. The first silicon position was corrected by projecting the results to this detector.

After the DSSDs are fixed to a common origin of coordinates, the alignment with the LAND detector is checked. Although the position of the center of LAND and the target with respect to the beam-axis is known with precision, a certain miss-alignment was found, that was considered as a small angle deviation of the DSSDs target ground plate. This was discovered by projecting the position distribution of incoming nuclei on LAND and comparing with neutron distributions. The deviation was corrected for applying a certain rotation correction reflected in X and Y offsets. A detailed explanation of the procedure is available in [77]. The uncertainty of the method ended up being dominated by the internal resolution of the DSSDs, 10 μm [78].

4.3 Fragment and neutron selection

^{13}Be is a resonant unbound nuclei and thus the half-life is around 10^{-21} seconds according to [79]. Such a small half-time results in a required mean distance for decaying of around $D_{decay} = c \cdot \beta \cdot \frac{t_{1/2}}{Ln(2)} \simeq 1,5 \cdot 10^{-11}$cm, using a rough $\beta \simeq 0.7$. The ^{13}Be will thus not reach any detector, forcing us to look for the ^{12}Be and the loss neutron.

There are two steps to follow in order to find the fragment $^{12}_{4}$Be, to select the charge (Z=4) and the mass (A=12). The first detector involved in the charge measurement after the reaction are the Double Sided Silicon

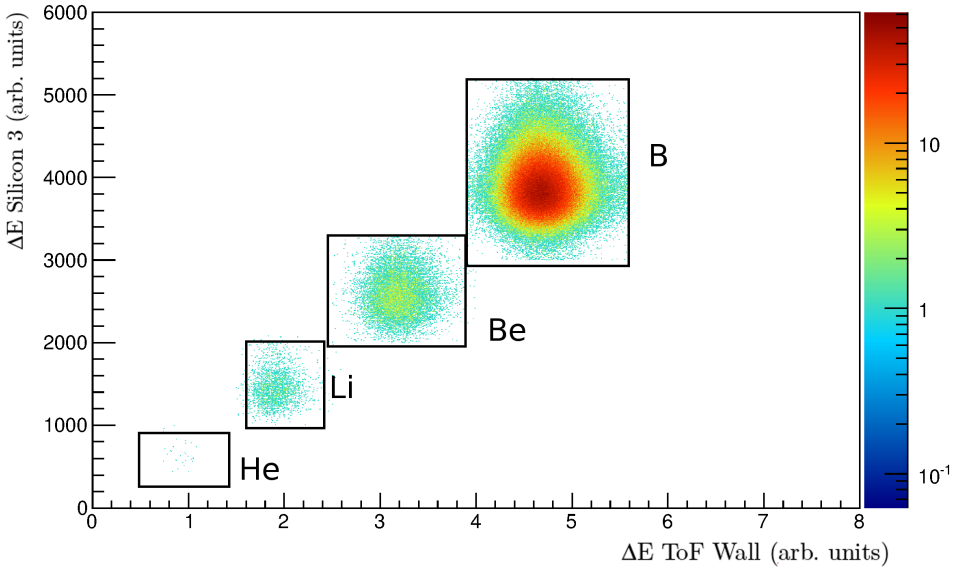

Figure 4.2: Charge identification plot, showing the energy loss in the first silicon after the target against the energy loss in the time of flight wall. The biggest blob is the unreacted beam, i.e. Boron, thus the second blob is the Beryllium, including $^{12}_{4}$Be, which is the main interest of this research work.

Detectors (DSSD), the energy loss in them is directly related to the charge of the fragment. Nevertheless the fragments produced in the reaction are unstable and they have a chance to disintegrate before reaching the end of the fragment branch. In order to guarantee their integrity the selection must be done in coincidence with the energy loss in the Time of Flight Wall (TFW) (see figure 4.2).

The second step is to produce a mass spectra (see figure 4.3), which includes the *tracker* (see section 3.8). Using the forward-tracking mode, the position of the silicons after the target are fixed and the tracks are minimized using the GFI(x) and the TFW(y) position.

In coincidence with the previous charge and mass selection, one neutron must be detected by LAND. Finding this nucleon is mandatory in order to produce a relative energy spectrum of ^{13}Be. Exists the option of making the coincidence including events with several neutrons detected, despite these kind of events were not many, it was decided to keep the most restricting option in order to have a cleaner energy spectrum at the end.

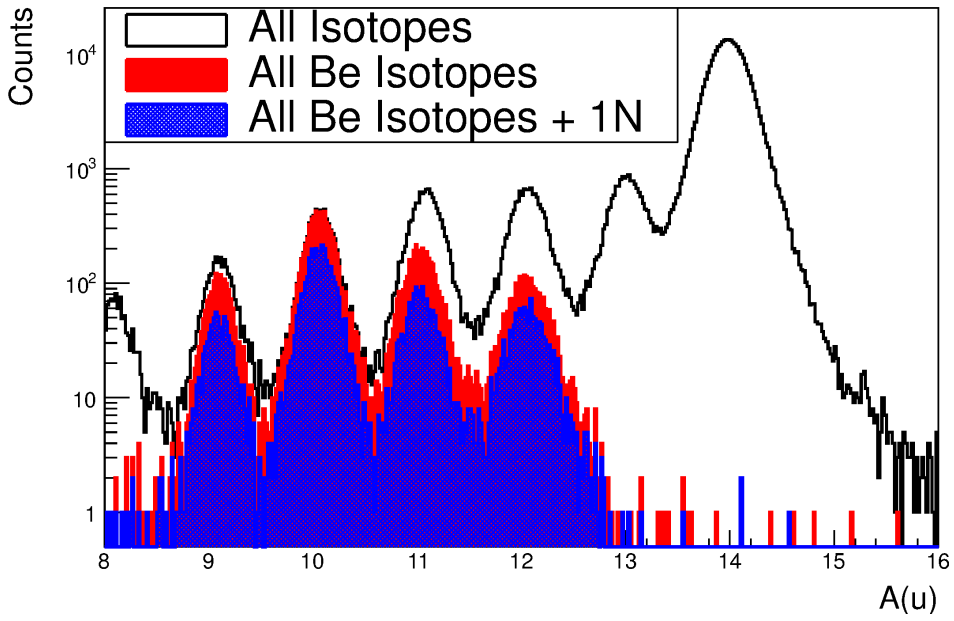

Figure 4.3: Overlap of three different mass spectrum following tracking. *White*: Selection of the incoming beam as ^{14}B. *Red*: Selected ^{14}B as incoming and Be as outgoing. *Blue*: Selected ^{14}B as incoming and Be as outgoing in coincidence with one neutron in LAND. The selection of the charge Z=4 makes the masses A=14,13 to disappear. This is coherent with the production of Beryllium from Boron in a (p, 2p) reaction and the unbound nature of the ^{13}Be.

4.4 Invariant mass and relative energy

This work is dedicated to investigate the nuclear structure of the ^{13}Be, we are going to use the invariant mass method [30] to obtain the relative energy spectrum of the ^{12}Be as well as of the outgoing neutron. The invariant mass method has been used before by the R3B Collaboration in several research works like [50] and [80].

This method is founded in the fact that Minkowski norm of the four-momenta of the physical system is a Lorentz invariant,

$$\mathbf{P} = \begin{pmatrix} P^0 \\ P^1 \\ P^2 \\ P^3 \end{pmatrix} = \begin{pmatrix} \frac{E}{c} \\ p_x \\ p_y \\ p_z \end{pmatrix} \tag{4.1}$$

which is related with the sum of the masses of the system [81] with:

$$||\mathbf{P}|| = \left(\sum_i P_i\right)^2 = M_{inv}^2 \cdot c^2 \tag{4.2}$$

Further development of the equation 4.2 makes it become 4.3 :

$$M_{inv} = \sqrt{\sum_i m_i^2 + \sum_{i \neq j} \frac{E_i \cdot E_j}{c^4} - \sum_{i \neq j} \frac{p_i \cdot p_j}{c^2} \cdot cos\theta_{ij}} \tag{4.3}$$

The equations 4.4 and 4.5 are introduced from the Special Relativity to produce the equation 4.6

$$E_i = \gamma_i \cdot m_i \cdot c^2 \tag{4.4}$$

$$p_i = \gamma_i \cdot m_i \cdot \beta_i \cdot c \tag{4.5}$$

$$M_{inv} = \sqrt{\sum_i m_i^2 + \sum_{i \neq j} m_i \cdot m_j \gamma_i \cdot \gamma_j \left(1 - \beta_i \cdot \beta_j \cdot cos\theta_{ij}\right)} \tag{4.6}$$

The invariant mass of a system is the sum of the rest masses of the components and the relative energy between them after break up (see figure 4.7).

$$M_{inv} \cdot c^2 = E_{rel} + \sum_i m_i \cdot c^2 \tag{4.7}$$

Including the previous invariant mass result of 4.6 into 4.7 deliver the equation 4.8.

$$E_{rel} = \left(\sqrt{\sum_i m_i^2 + \sum_{i \neq j} m_i m_j \gamma_i \gamma_j \left(1 - \beta_i \beta_j cos\theta_{ij}\right)} - \sum_i m_i\right) c^2 \tag{4.8}$$

Applied on the case of ^{14}B(p,2p)^{13}Be,

$$E_{rel} = \left(\sqrt{m_{^{12}Be}^2 + m_n^2 + m_{^{12}Be} m_n \gamma_{^{12}Be} \gamma_n \left(1 - \beta_{^{12}Be} \beta_n cos\theta_{^{12}Be+n}\right)} - m_{^{12}Be} - m_n\right) c^2. \tag{4.9}$$

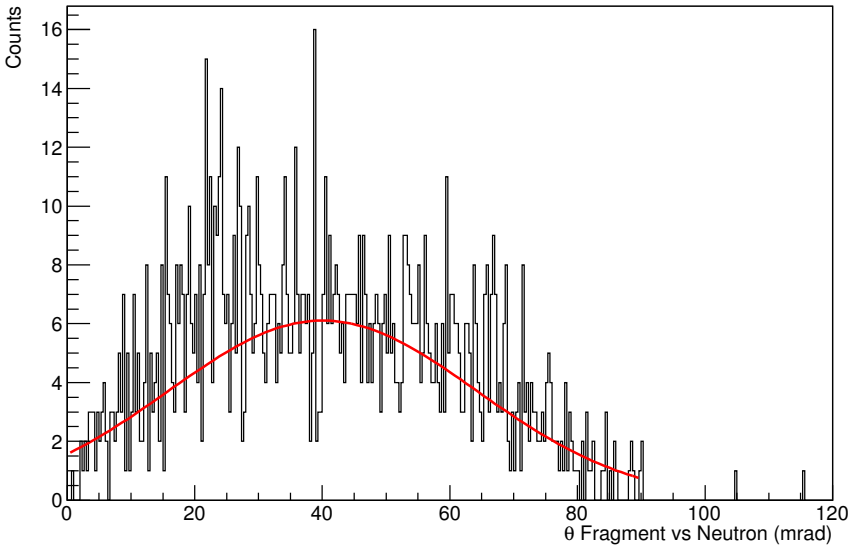

Figure 4.4: The angular distribution between the outgoing neutron and the ^{12}Be. It has been fitted to a Gaussian distribution.

From equation 4.9 one can deduce the observables to perform the analysis:

- $\theta_{^{12}Be+n}$

  The opening angle between the outgoing fragment ^{12}Be and the neutron. This parameter can be determined combining the data from the DSSDs and LAND respectively. The figure 4.4 shows the angle distribution of the reconstructed ^{13}Be.

- β & γ

  The velocity of the outgoing products (fragment and neutron) is related to the β and γ parameters. These are measured using the TFW and LAND, correcting it with the tracker. Both velocities distribution are in figures 4.5 and 4.6, the latter shows that there is an appreciable difference between the distribution of fragment-velocity in each FRS setting.

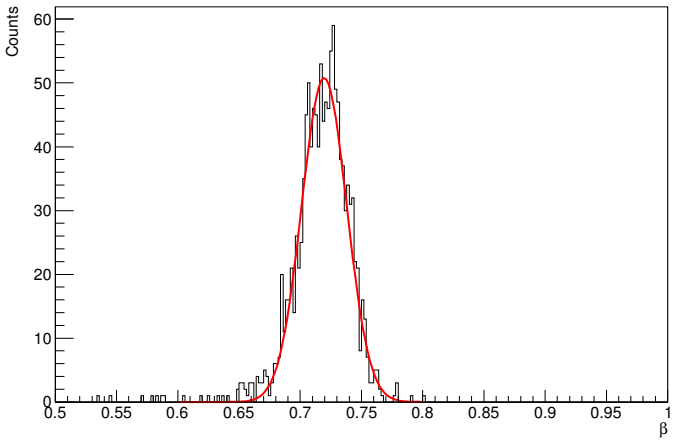

Figure 4.5: β of the outgoing neutron after break up. A fit using a Gaussian distribution has been applied, giving a value of β_n=0.719±0.02

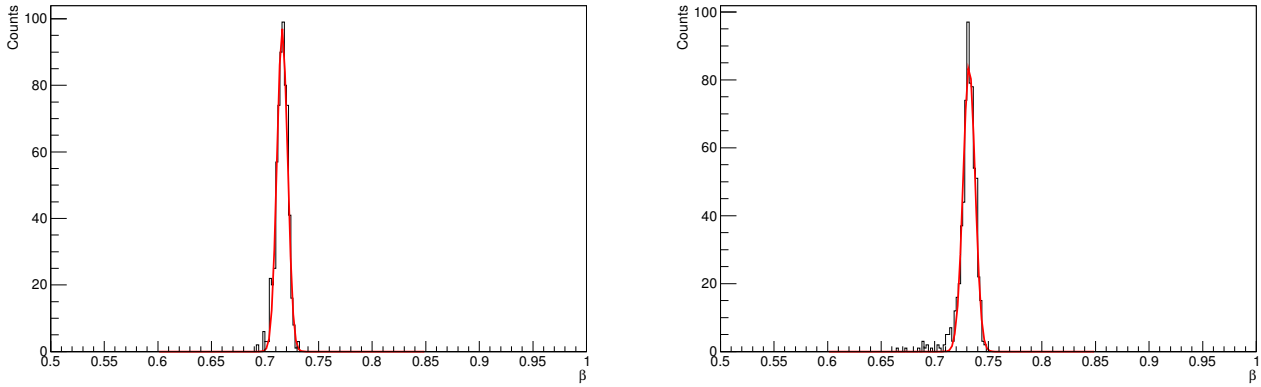

(a) (b)

Figure 4.6: β of the outgoing ^{12}Be fragment after break up. Due to the fact that two different fragment separator settings are used for the final analysis, the incoming and outgoing fragment have two different velocities: (a)Data from setting 4, centered at ^{22}O ; (b) Data from setting 5, centered at ^{23}O. A fit using a Gaussian distribution has been applied over the two different datasets, the values obtained are β_{Fset4}=0.716±0.005 and β_{Fset5}=0.732±0.005

The relative energy of the system ^{12}Be and neutron of the events that fulfill the previously explained conditions is displayed in figure 4.7. A total

amount of 1257 candidates of 12Be + neutron have been found within the 0-6 MeV range of the Relative energy spectrum.

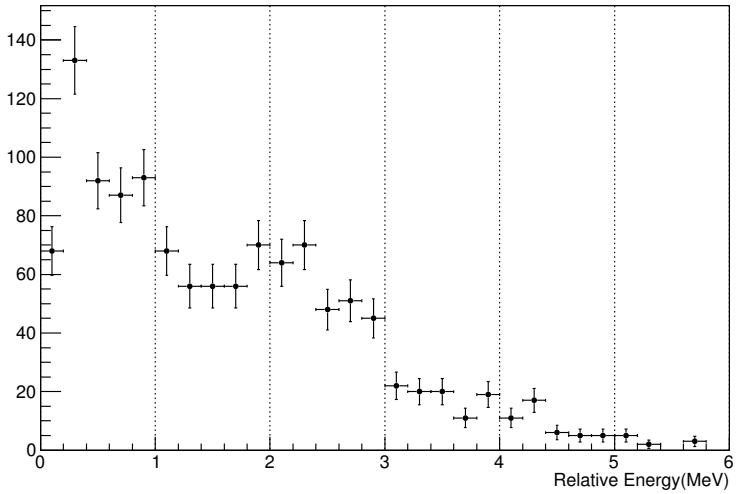

Figure 4.7: Relative energy spectrum of ^{12}Be+neutron. It is obtained with the equation 4.9. The physical interpretation of this figure will be detailed in the chapter 5. Using both data settings, the result has 1257 counts that made it through the conditions imposed.

4.5 Breit-Wigner fit

The aim of this thesis work is disentangle the spectrum of figure 4.7 and study the structure of the nucleus ^{13}Be. It is an unbound nuclei,therefore even it ground state is unbound, however it display certain internal structure in the form of resonances or quasi-stationary states. They are almost bound states, with energies not far from the limits determined from the potential. A peak observable at the relative energy of the system reveals the coincidence with one of these exotic states. These kind of states are described by the Breit-Wigner formula (equation 4.10),

$$\frac{d\sigma}{dE} \sim \frac{\Gamma(E)}{(E_r - E)^2 + \frac{\Gamma(E)^2}{4}} \tag{4.10}$$

The resonance width $\Gamma(E)$ is dependent of the reduced width of the resonance γ^2 and the penetrability factor $P_l(\rho, \eta)$, where l is the angular momentum of the resonance and η is the Coulomb field parameter.

$$\Gamma(E) = 2\gamma^2 P_l(\rho, \eta) \tag{4.11}$$

The parameter ρ is proportional to the reduced mass of the system μ, the channel radius R and the energy E as well as inversely proportional to the reduced Planck constant $\hbar$.

$$\rho = kR = \frac{\sqrt{2\mu E}R}{\hbar} \tag{4.12}$$

The Penetrability factor for neutrons (η=0) is an expression only dependent on ρ, but different for each angular momentum.

$$\begin{aligned} P_0(\rho) &= \rho; \\ P_1(\rho) &= \frac{\rho^3}{1+\rho^2}; \\ P_2(\rho) &= \frac{\rho^5}{9+3\rho^2+\rho^4}; \end{aligned} \tag{4.13}$$

The first conclusion got out from the Breit-Wigner expression is that only two parameters are free to be fitted; the reduced width of the resonance γ, and the resonance energy E_r. The channel radius R must be specially pointed out, this can be described as the range of the used potential. Dividing the R-Matrix into an internal and an external area, therefore it has to be chosen to be larger than the potential radius, thus in the external area only the asymptotic part of the wave function is taken into account. The final result for E_r is not very sensitive to the R value variation as will be seen in the section 5.1.

The function obtained to be fitted has to be folded with detector resolution as will be shown in the section 5.1.1.

4.6 Looking for gamma-rays

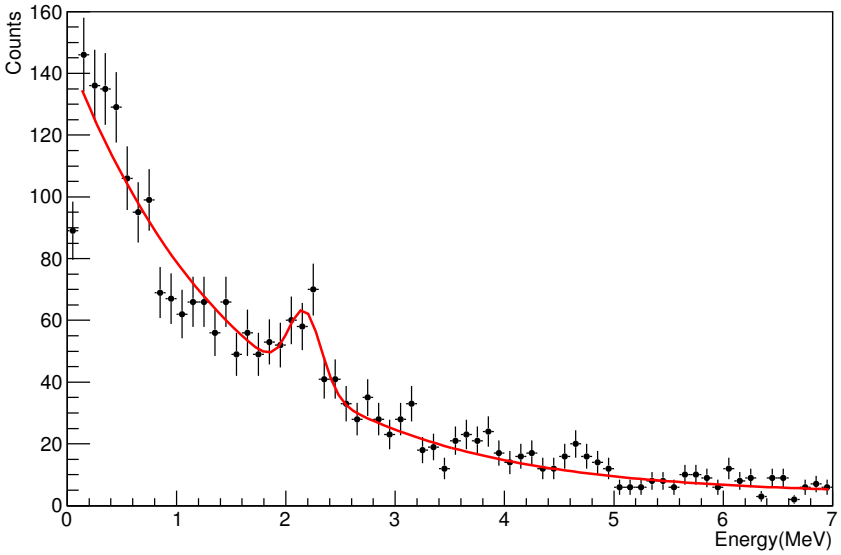

Figure 4.8: ^{13}Be Gamma spectrum detected by Crystal Ball in coincidence with the data showed in the relative energy spectrum (see figure 4.7). The spectrum has been fitted to an exponential + Gaussian distribution in order to subtract the background. One broad gamma-ray peak can be found around 2-2.4 MeV. The fit set the gamma-ray peak at E=2.17$\pm$0.04 MeV.

Unfortunately, the invariant mass method have a drawback, it lacks sensitivity about the energy within the decaying products, just informs about the energy that has been transformed to kinetic energy. To be able to know the ^{13}Be structure with full confidence, it is necessary to compare with the possible states in ^{12}Be that could be fed in the reaction. The way to do it is checking the prompt gamma ray emitted just after the decay with the Crystal Ball detector (section 2.3.2). Figure 4.8 shows the gamma spectrum, including a fit to the background using a negative exponential model and a Gaussian distribution for the broad peak around 2-2.4 MeV.

The daughter nucleus ^{12}Be has been studied extensively in recent years, thus we know already what we are looking for. Figure 4.9 shows that mainly there are three possible excited fed states by the ^{13}Be break up at 2.1, 2.24 and 2.7 MeV. Although the second one at 2.24 MeV is an isomeric state [82] with a too long life time (τ =357(22) ns [83], τ = 331 (12) ns [84]) for the possibilities of this detector setup. In case of feeding the isomeric state the decay will occur far from any detection chance. It is also worth men-

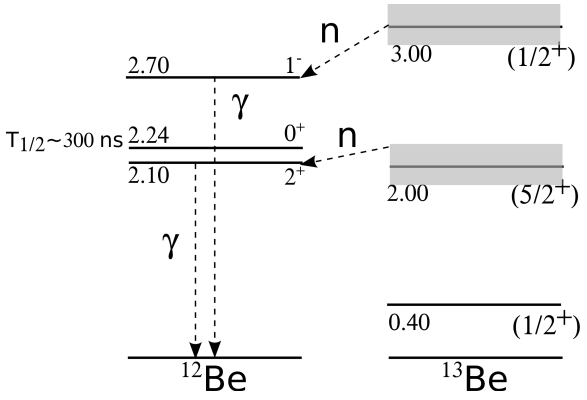

Figure 4.9: ^{12}Be energy level structure with dummy feeding from ^{13}Be . The three possible bound excited states of the ^{12}Be are shown. The state at 2.24 MeV is 0^+, thus decay via γ emission to the ground state is forbidden, further explanation in the text. The states included in ^{13}Be just as a hypothesis to ilustrate the decaying via neutron emission that feds the ^{12}Be states. This level scheme includes the usually accepted states around 0.4 and 2 MeV(this latter only can decay via neutron emission to the 2.10 MeV state from the upper part of the resonance). The state at 3 MeV is a possibility suggested in several papers.

tioning that this kind of state will not decay to the ground state by gamma emission because both are 0^+ and such a transition is forbidden. Therefore it only has two ways to decay to the ground state, electron capture or pair production, in this case the nuclei should be full stripped of electrons, thus the first path should not be available, just the second. The other way of decaying from the 2.24 MeV is emitting one low energy gamma to the 2.1 MeV state from where it could decay again to the ground state.

At the gamma spectrum of figure 4.8, the fit to the Gaussian-shaped distribution located the broad peak at E=2.17$\pm$0.04 MeV with σ=0.49$\pm$0.05, whereas the background has been subtracted as can be seen in figure 4.10. The result of the subtraction was fit again in the same region, positioning the gamma peak at 2.15$\pm$0.02 MeV with σ=0.15$\pm$0.02.

In the only previous ^{13}Be experiment where gamma rays detectors were available [42], they found not only gammas from the first excited state of ^{12}Be at 2.1 MeV but also from the state at 2.7 MeV. The available data of this experiment have not shown a peak that can be correlated to that second state.

The next step is to find a correlation between the gamma ray and any of the resonances found in the ^{12}Be + n relative energy spectrum (see figure 4.7). The peak has been gated-on and the result (see figure 4.11) seems to

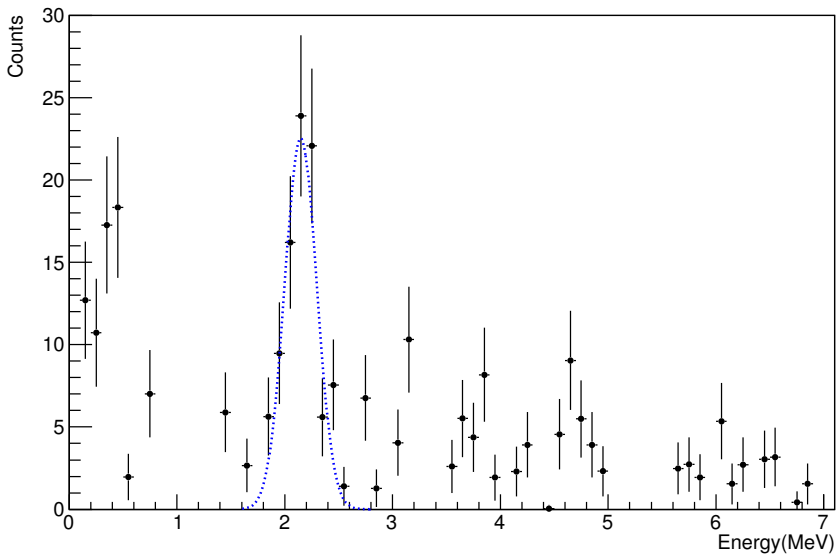

Figure 4.10: The same gamma spectrum of figure 4.8 after subtracting the background.

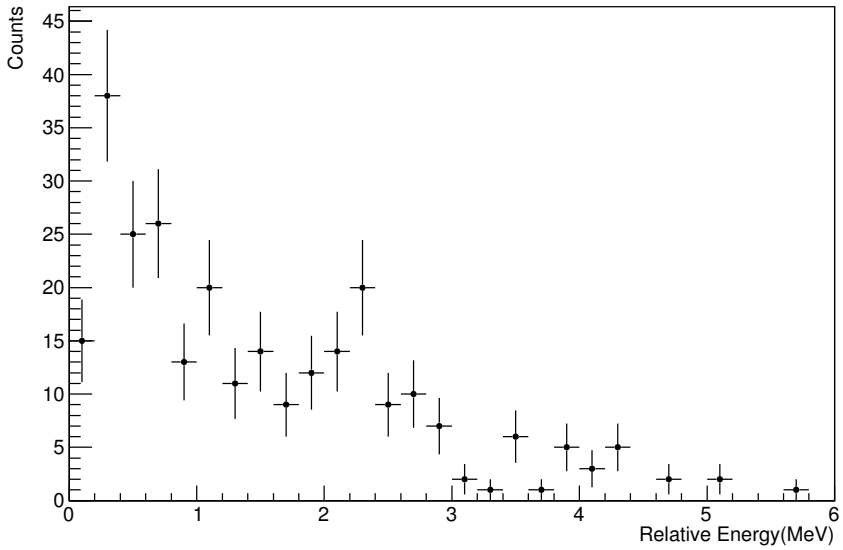

Figure 4.11: ^{13}Be Relative energy spectrum after gating on the gamma-ray of 2.1 MeV.

be dominated by the uncorrelated counts below it, as the result is not too different from the ungated spectrum. In order to clean the uncorrelated counts, the gamma spectrum has been gated off-peak on both sides and a mean of the two relative energy spectra has been performed. The result of the latter has been subtracted from figure 4.11, and the outcome is in figure 4.12. Several other methods to subtract the uncorrelated ^{13}Be events from the relative energy spectrum of the coincidence with the gamma ray at 2.1 MeV have been tried. Although the final result has been similar.

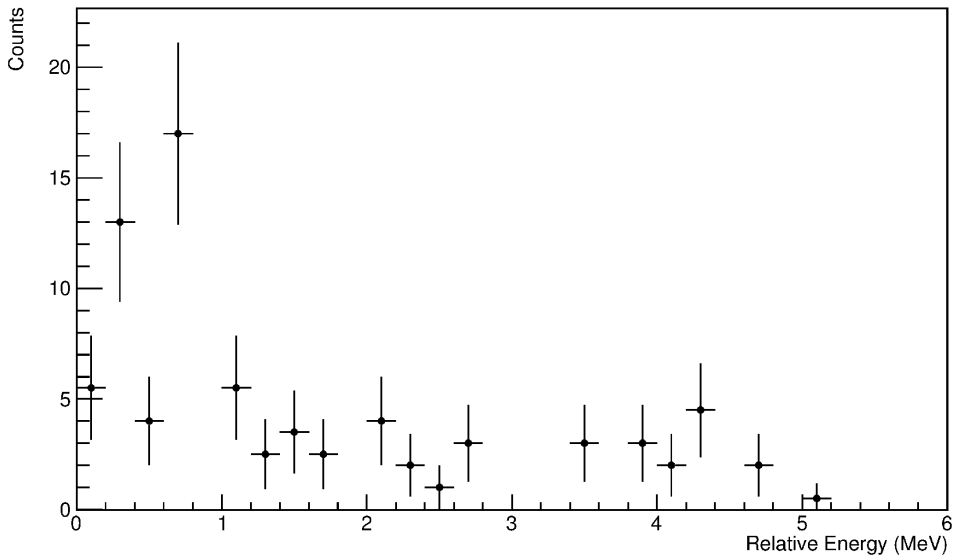

Figure 4.12: ^{13}Be Relative energy spectrum after subtraction of the uncorrelated events. The only bins still favoured are the second and the fourth at 0.3 and 0.7 MeV.

Due to the low statistics is not easy to draw a conclusion from figure 4.12. It seems obvious that there is no correlation with any medium or high energy resonance, as the relative energy spectrum seems rather flat above 1 MeV in all the subtraction methods used. The two bins at 0.3 and 0.7 MeV are in general favoured after removing the uncorrelated events, although the bin at 0.5 MeV is suppressed. Hence, it can be understood as both possible resonances located around those bins are partially fed by a ^{13}Be state that decay at the 2.1 MeV ^{12}Be state. However the second bin of the relative energy spectrum at 0.5 MeV is the highest and in figure 4.12 is lower than the fourth, as the total amount of counts in the peak area was higher than the amount subtracted from the off-peak events, thus it is possible that this low-energy resonance is still uncorrelated from the gamma.

4.7 Looking for the protons of the (p,2p) reaction

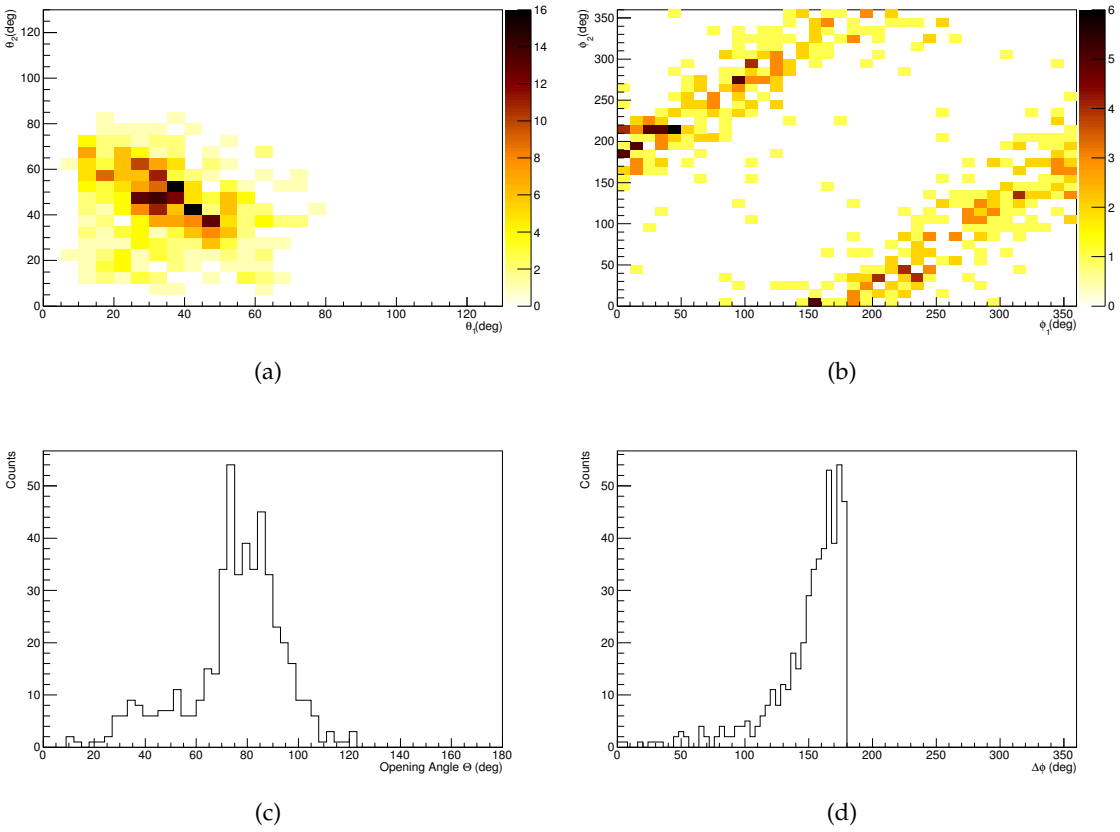

Figure 4.13: Angular distributions of two protons in coincidence with ^{12}Be events from ^{14}B, the integral have 487 counts:(a) Polar Angle correlation, quasi-free scattering correlation is slightly displayed ; (b) Azimuthal Angle correlation, the two strips of correlation between both angles can be slightly seen; (c) Opening Angle, peaked a bit lower of 80°; (d)Azimuthal angle difference, peaked at 180°.

The reaction I am dealing with is ^{14}B(p,2p)^{13}Be using a polyethylene CH_2 target, in the analysis so far I have concentrated in looking for the ^{12}Be + n system. Despite that the previous requirements for the outgoing channel are very selective (incoming ^{14}B + ^{12}Be + n), observing two outgoing high-energy protons with QuasiFree conditions in Crystal Ball would clarify the complete picture of the reaction. However we are limited by the statistics, it is necessary to have a reasonable amount of counts in order to draw conclusions about the structure of ^{13}Be, therefore adding more re-

quirements to clean completely the reaction channel is not necessarily the best option.

This (p , 2p) QuasiFree scattering reaction is characterized by the angular correlation between the two outgoing protons. At non-relativistic velocities the outgoing protons have an average opening angle of 90°, however as shown in section 4.4 in this experiment the nuclei has a $\beta \simeq 0.73$ and thus relativistic considerations must be taken into account. The incident protons (in the ^{14}B) have bigger relativistic mass than the protons at rest in the target, hence the average opening angle between the knocked out protons is smaller, around 82° - 84° . The equation 4.14 is obtained from the scalar product of the vectors of the two outgoing protons.

$$\Theta_{OpAngle} = sin\theta_1 \cdot sin\theta_2 \cdot cos(\phi_2 - \phi_1) + cos\theta_1 \cdot cos\theta_2 \tag{4.14}$$

Additionally, the two particles are emitted back to back in the azimuthal angle $\Delta\phi$ = 180°. In order to represent the azimuthal angle difference, whenever the condition $\Delta\phi$ >180° or $\Delta\phi < 0°$ are fulfilled, the difference is redefined as $\Delta\phi$= 360° - $\Delta\phi$.

Figures 4.13 and 4.14 display the angular distributions as well as the $\Theta_{OpAngle}$ and $\Delta\phi$, using the same conditions as required in section 4.4 for the relative energy, although for figure 4.14 I have avoided the one neutron requirement to increase the statistics a factor of almost two (from 487 to 942 counts). The figures display the two clusters with higher energies detected within an event, having at least 30 MeV in order to discard energies coming from gamma rays. It have to be taken into account that the crystals are rather big and they have an angular uncertainty of ±7.5°, as every event include at least two crystal, the uncertainty could be up to 15°. The angle assigned to every crystal ball event is coming from the crystal hit in that event, therefore due to the size of the crystal, in order to have a good visualization without large gaps in the angular distributions a randomisation [49] in the nominal value of the crystals angle is added to every proton event.

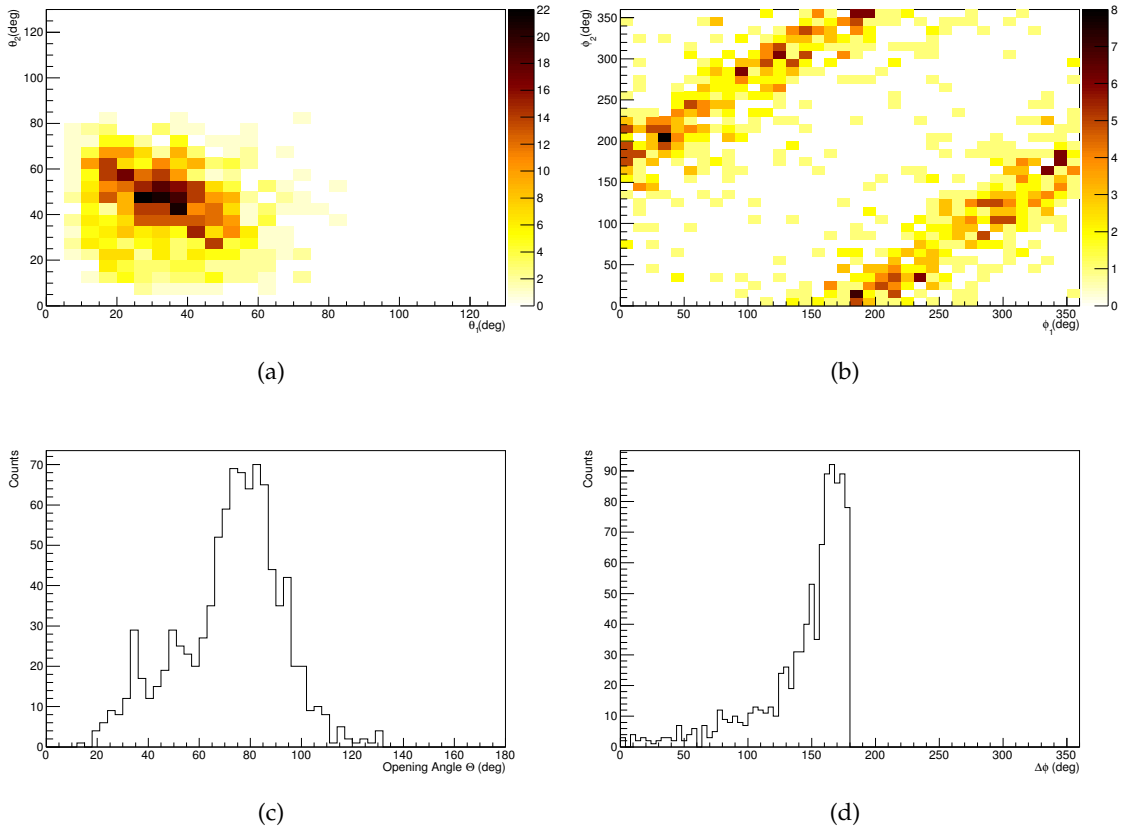

Figure 4.14: Angular distributions of two protons in coincidence with ^{12}Be events from ^{14}B, the integral have 942 counts: (a)Polar Angle correlation, quasi-free scattering correlation can be seen better than in figure 4.13; (b) Azimuthal Angle correlation, the two strips of correlation between both ϕ angles can be seen better than in figure 4.13; (c) Opening Angle, peaked a bit lower of 80°; (d) Azimuthal angle difference, peaked at 180°.

**"All Bette's stories have happy endings. That's because she knows where to stop.
She's realized the real problem with stories...
if you keep them going long enough, they always end in death. "
Neil Gaiman. 24 Hours, The Sandman**

5 Results & Discussion

The previous chapter has covered the analysis method followed to clean and select the production channel of ^{13}Be and it has introduced the basis of the fitting to a Breit-Wigner function including the singularities for this kind of unbound nuclei.

The current chapter will show the different results obtained and the discussion about the interpretation of them in the context of the previous results published.

5.1 Preliminaries

In order to perform the fits a channel radius of R = 5 fm has been assumed. This value has to be large enough to be out of the potential radius extension. It has been taken following Kondo et al [42] who used a value of 4.9 fm, and taking into consideration that in [80] it is shown that a variation of 1-2 fm in this value should not represent a significant difference to the result of the fit, the detector resolution has a much bigger influence.

In order to confirm the previous assumption, after getting a good fit with a reasonable set of values, the position of the resonance has been fixed as well as the angular momentum, and a set of new fits has been performed considering different channel radii. The result of that set of fits can be seen in figure 5.1. It is possible to see certain differences on several spots harder to fit, but can be concluded that the parameter R considered does not determine a big difference in the result.

The minimization method followed has been the χ^2 approach with the MINUIT tool [85]. Despite the low number of counts in the relative energy spectrum, which is a problem for the physical interpretation, it does not represent a problem to be fitted by the χ^2 method which does not work properly with empty or close to empty bins.

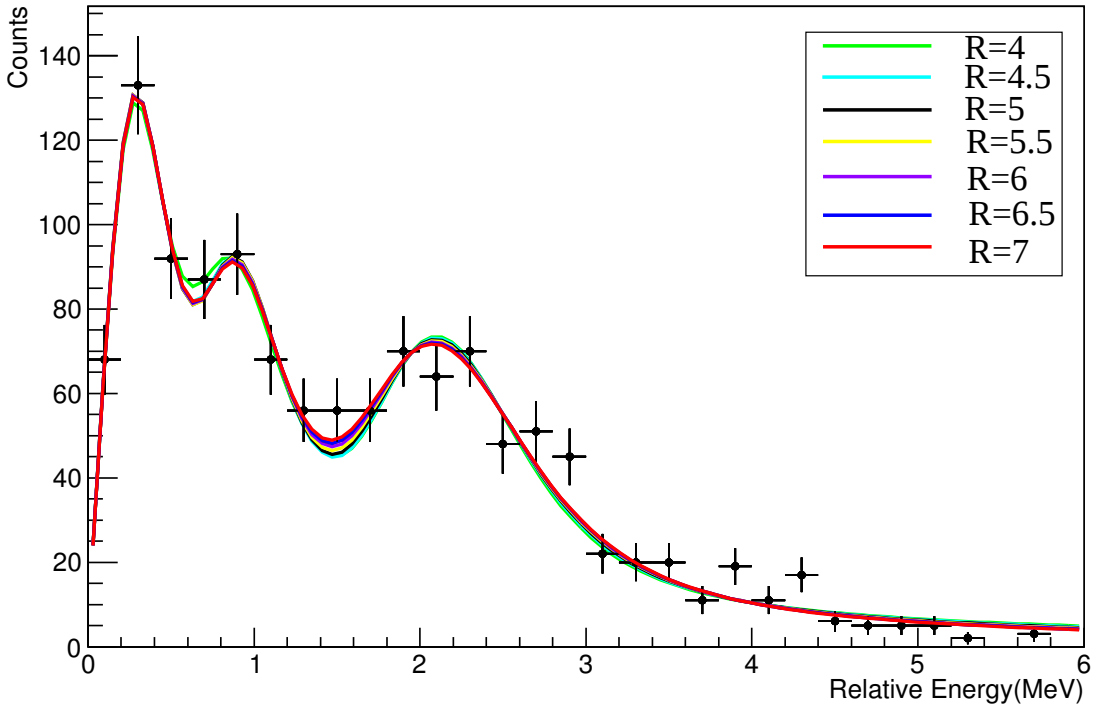

Figure 5.1: Channel Radius comparison. 1-2 fm Changes do not determine a big difference in the final result of the fit.

5.1.1 Folding

In order to compare the relative energy results with the fit to a Breit-Wigner function, it should be folded with the detector resolutions, introducing the uncertainty related to the detector response.

The response function is described using a Gaussian shape with a certain standard deviation σ, that is defined following the function in figure 5.2 for the relevant energy range. Therefore a Gaussian function with that σ dependence is included into the fit procedure.

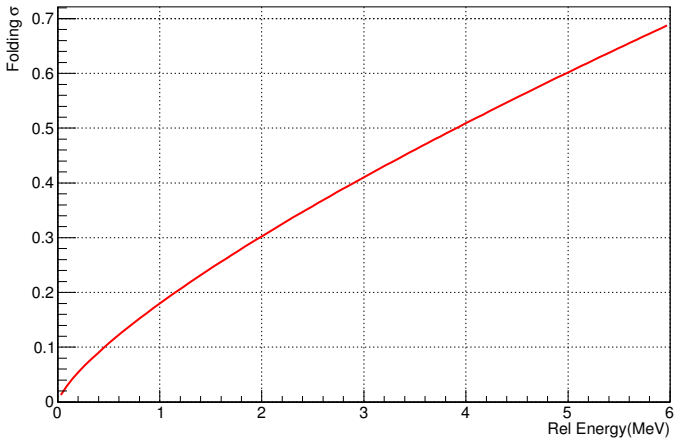

Figure 5.2: Relative energy range against the calculated standard deviation σ used for the folding function.

5.1.2 Non Resonant Background

Despite the reaction channel should be rather clean after the previous selections (see section 4), it is likely that there are events within the spectrum that are the result of a wrong identification either from the incoming or outgoing fragment or the neutron detected. In order to take into account such misidentification a Non-resonant Background has been modeled with the equation 5.1. The model has a negative exponential function and an Error Function with three parameters: $A_{1,2,3}$.

$$E_{NR} = A_1 \cdot e^{-A_2 E} \cdot erf(A_3 E) \tag{5.1}$$

This addition to the fit, makes the resonances results more chaotic, i.e., more dependent to the initial parameter values as well as the constraints included for them and the three parameters of the background. This situation has made impossible to leave freely the background parameters, not only because they easily adopt non-physical negative values but because they greatly determine changes on the resonances. Therefore a previous approximation for the parameters $A_{2,3}$ has been performed as can be seen in figure 5.3. The equation 5.1 has been used to fit a relative energy calculated including other of fragments tracked (Beryllium masses ranging from A = 10-14) whereas the condition of finding one neutron in LAND was fixed.

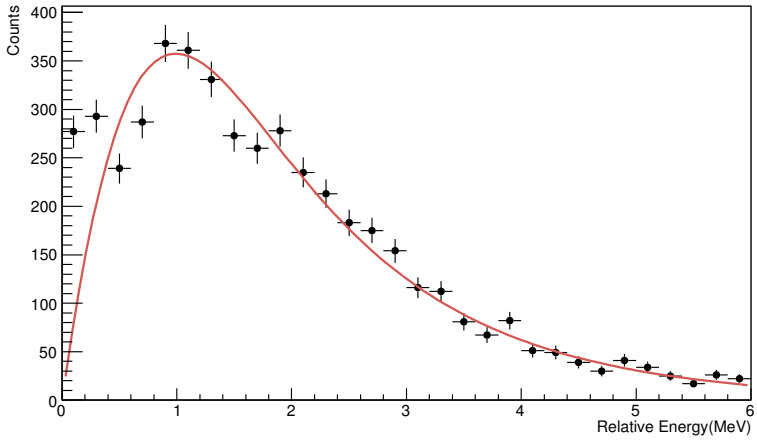

Figure 5.3: Non-Resonant background fitted to get an approximation to the parameters $A_{2,3}$. The data comes from considering for the relative energy calculation the Beryllium fragments with masses between A = 10 and 14 coming out from the ^{14}B reaction with the CH_2 target.

Such a model function has been included to several of the following fits, leaving the first constant (A_1) free. The function was just added to the Breit-Wigner global function and fit accordingly.A similar method has been followed in [17].

5.2 Results

5.2.1 Initial parameters

The first approach has been to perform a set of individual fits to the three resonances that can be seen in the relative energy spectrum in order to find a set of reasonable starting values for each parameter to perform a global fit. The method followed has been fixing the values of the angular momentum l and going through a reasonable range of values for the γ^2 and E_r. Previous publications have found or assumed a low energy virtual state or a ground state with l=0, and found another resonance around 2 MeV with l=2, thus it has been the basic assumption, even though other values have also been tried.

The single fit of each of the three resonances considered are shown in figure 5.4. I have gone through all the values for Er and γ (reduced width, related with Γ, see section 4.5) in a reasonable range to look for good starting values for the global fit. It is worth to point out that for certain fits the value obtained of $\chi^2/N_{df} << 1$, thus the result is overfit and although

it is the minimum value, in general it should not be considered as the best result to start working with. In any case, the values obtained fitting a single resonance are just an approximation that does not represent the real values of the resonances.

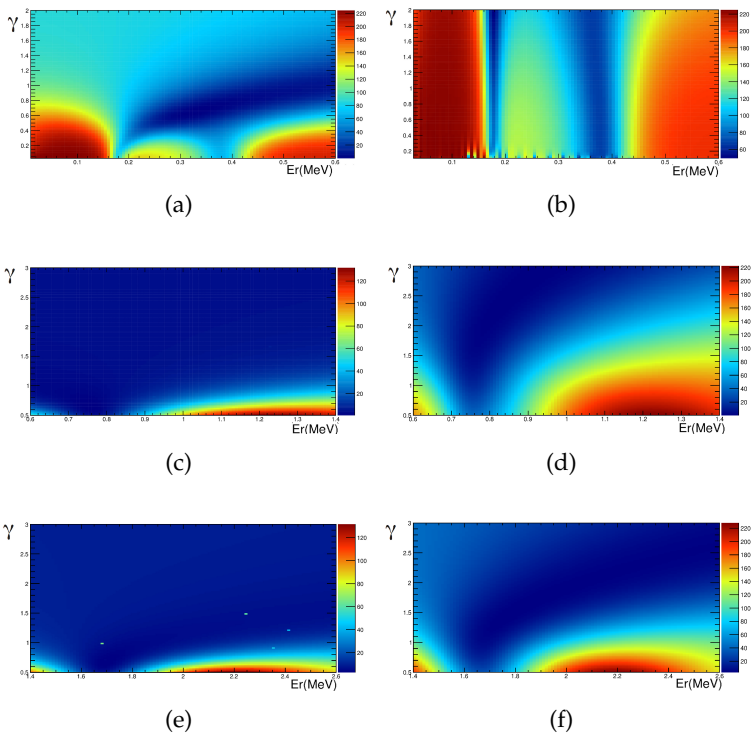

Figure 5.4: The color in the Z coordinate represents the calculated value of χ^2, whereas γ is the reduced width(related with $\Gamma(E)$) and Er the mean value of the resonance. (a) And(b) show the first resonance assumed between 0 and 0.6 MeV with *l*=0,2; (c) and (d) show the second resonance assumed between 0.6 and 1.4 MeV with *l*=0,2; (e) and (f) show the third resonance assumed between 1.4 and 2.6 MeV with *l*=0,2;

The values obtained for the resonance at low energies with *l*=0 of figure 5.4(a) display an important difference in the χ^2 value between 0.2 MeV and 0.4 MeV specially for small widths. A more careful look at these values using the relative energy spectrum shows a strange behaviour close to 0.2 MeV , while the results close to 0.4 MeV are more reasonable. The large size of the bins (0.2 MeV), and the big difference in the number of counts between the first bin at 0.1 MeV and the second at 0.3 MeV is generating this strange behaviour with small widths.

The structure of the incoming ^{14}B nuclei is known and in several publications [86][87] the components of the valence neutrons have $s_{1/2}$ and $d_{5/2}$ character, therefore this is the configuration for the momentum of ^{13}Be states that has been fed in this experiment.

5.2.2 Considering two resonances

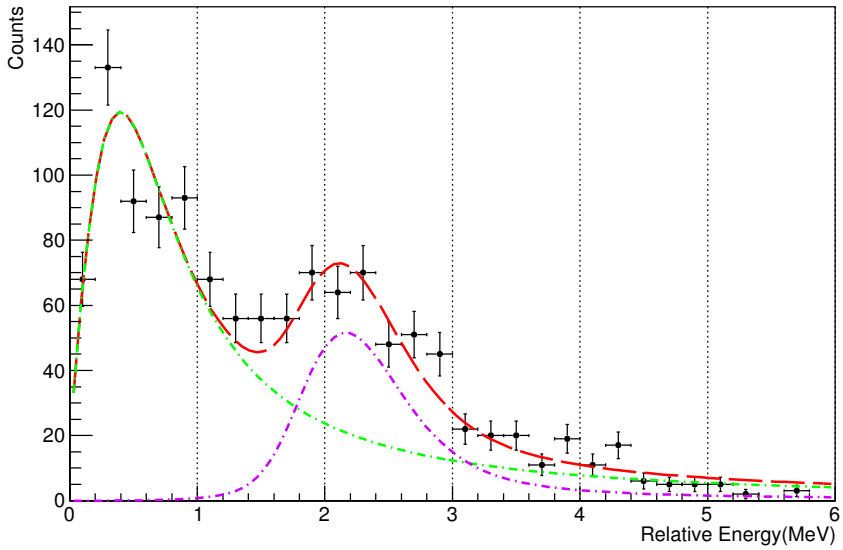

Figure 5.5: Visualization of the fit with two resonances l= 0 (green), 2 (purple) and without a Non-resonant background. The global fit has a goodness of χ^2/N_{df}=2.23903 and it is represented by the red line. Table 5.1 show the results.

#	E_r(MeV)	Γ (MeV)	l
1	0.54(0.04)	1.185(0.002)	0
2	2.18(0.06)	0.381(0.009)	2
χ^2		49.2588	
χ^2/N_{df}		2.23903	

Table 5.1: Table of results considering two peaks without Non Resonant Background and l= 0,2. Figure 5.5 shows the visualization of the fit.

Previous studies have determined only two resonances within the range of 0-2.5 MeV for the ^{13}Be nucleus. Thus, although the fifth bin of the

histogram shows an increment and a significant difference with the sixth bin, it should be considered the option of only two open resonances.

A low energy state with l=0 and another close to 2 MeV with l=2 are initially considered. A fit without a non-resonant background has been made, but the result (see figure 5.5) shows that the first Breit-Wigner function alone is not capable to make a good approximation for its range. The χ^2/N_{df}= 2.23903 indicates the low-quality of this fit (see the result of the fit at table 5.1).

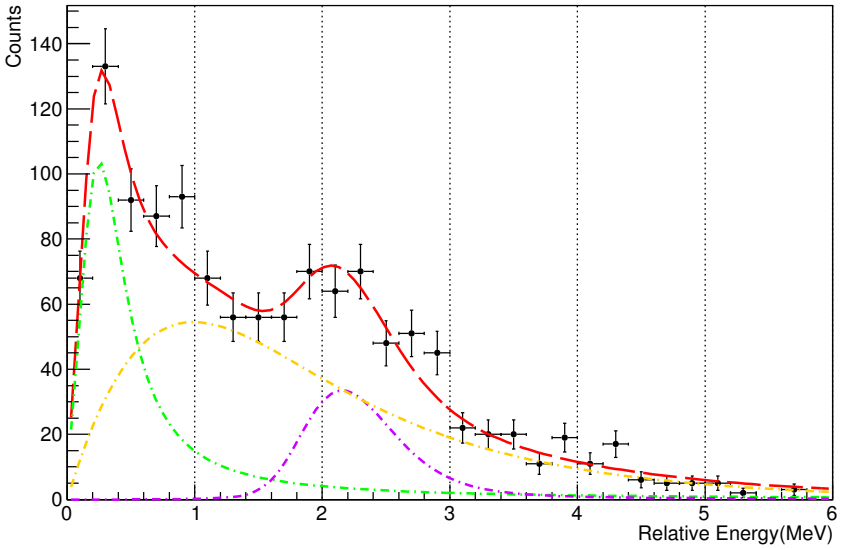

Figure 5.6: Visualization of the fit considering two resonances l= 0 (green), 2 (purple) with Non resonant background (yellow). The global fit has a goodness of χ^2/N_{df}=2.23903 and it is represented by the red line. Table 5.2 show the results.

#	E_r(MeV)	Γ (MeV)	l
1	0.287(0.038)	0.411(0.008)	0
2	2.18(fixed)	0.176(0.034)	2
χ^2		29.04	
χ^2/N_{df}		1.32	

Table 5.2: Table of results considering two resonances with Non Resonant Background and l= 0,2. Figure 5.6 shows the visualization of the fit.

In order to improve the fit, a non-resonant background has been included, the initial values for the mean and width parameters have been the results from the previous fit (table 5.1). The output of the fit had the tendency to produce non-physical values for the resonance widths (lower than 0.1 MeV). To get a result with physical meaning it has been necessary to fix a parameter, the resonance position of the second curve E_r=2.18$\pm$0.06 MeV. It was chosen because it is the least affected by the inclusion of the background. The results of the fit can be seen in table 5.2, the value χ^2/N_{df}=1.32 has been improved significantly. Even though the background gives a better description of the area 0.7-1.7 MeV, it almost skip the count increment in the 0.9 MeV bin, as can be seen in figure 5.6, however sthe description of the low-energy part of the spectrum has improved.

5.2.3 Considering three resonances

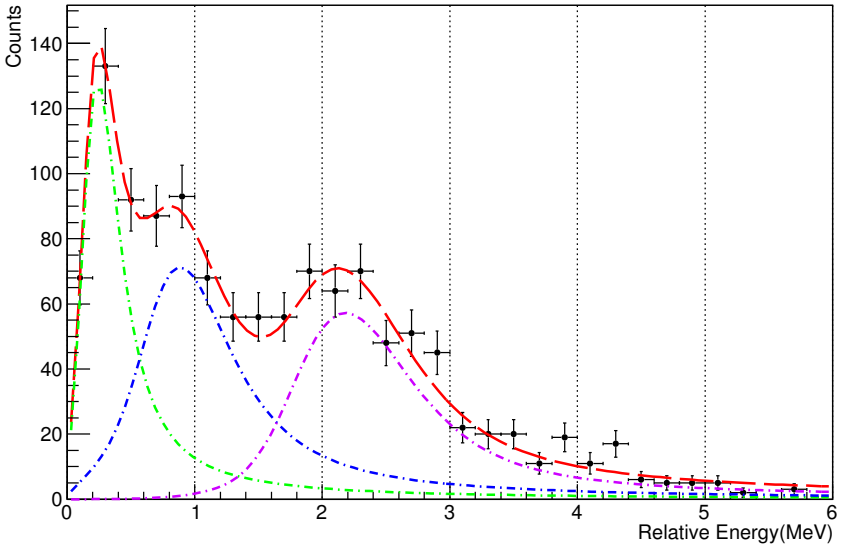

Figure 5.7: Visualization of the fit considering three Breit Wigner functions with l= 0 for the green line, l= 0 for the blue line, l= 2 for the purple line. The global fit has a goodness of χ^2/N_{df}= 1.26978 and it is represented by the red line. The position of the resonances and the widths obtained are in table 5.3.

#	E_r(MeV)	Γ (MeV)	l
1	0.265(0.048)	0.319(0.013)	0
2	0.929(0.080)	0.741(0.029)	0
3	2.209(0.064)	0.635(0.064)	2
χ^2		24.126	
χ^2/N_{df}		1.26978	

Table 5.3: Table of results considering three resonances without Non-Resonant Background and l= 0, 0, 2. The visualization of it is displayed in figure 5.7.

Previous publications have considered the inclusion of a s-or-p state in the region between the low energy s-state and the d-state at 2 MeV [46]. In order to try to reproduce the count increment of the fourth and fifth bin (0.7-0.9 MeV), another Breit-Wigner function has been introduced into the

fit, within the energy range 0.6 - 1.2 MeV. The two possible orbital momentum l= 0,2 have been considered.

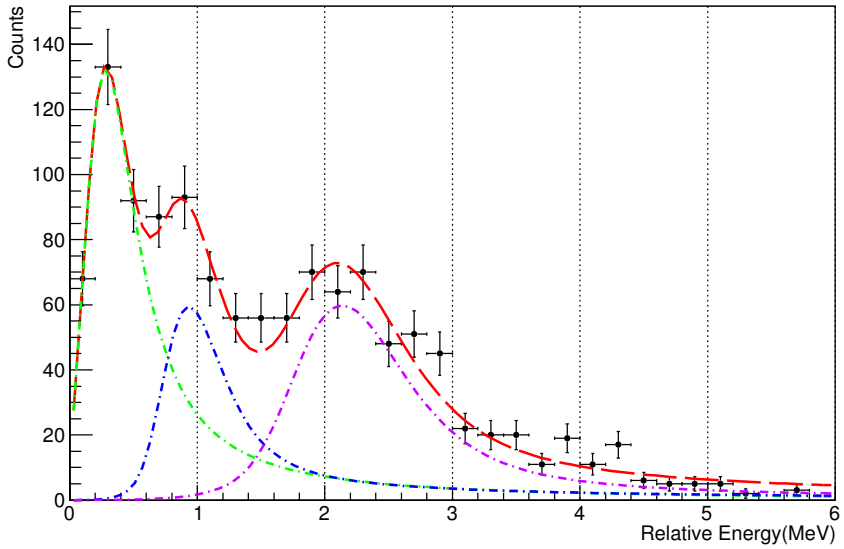

Figure 5.8: Visualization of the fit considering three resonances using three Breit Wigner functions with l= 0 for the green line, l= 2 for the blue line, l= 2 for the purple line. The global fit has a goodness of χ^2/N_{df}= 1.574 and it is represented by the red line. The position of the resonances and the widths obtained are in table 5.4.

#	E_r(MeV)	Γ (MeV)	l
1	0.333(0.036)	0.5196(0.0054)	0
2	0.951(0.055)	0.29(0.026)	2
3	2.157(0.058)	0.5845(0.0076)	2
χ^2		29.9	
χ^2/N_{df}		1.574	

Table 5.4: Table of results considering three resonances without Non-Resonant Background and l= 0, 2, 2. The visualization of the fit is displayed in figure 5.8.

In this case the results obtained for the χ^2/N_{df} (see tables 5.3 and 5.4) are closer to 1 and the fits seems to be more reliable. Figures 5.7 and 5.8 are similar, both options have the same third resonance (within the errors) whereas the widths of the other two resonances are rather different in each case, even the position of the first resonance changes meaningfully between both options.

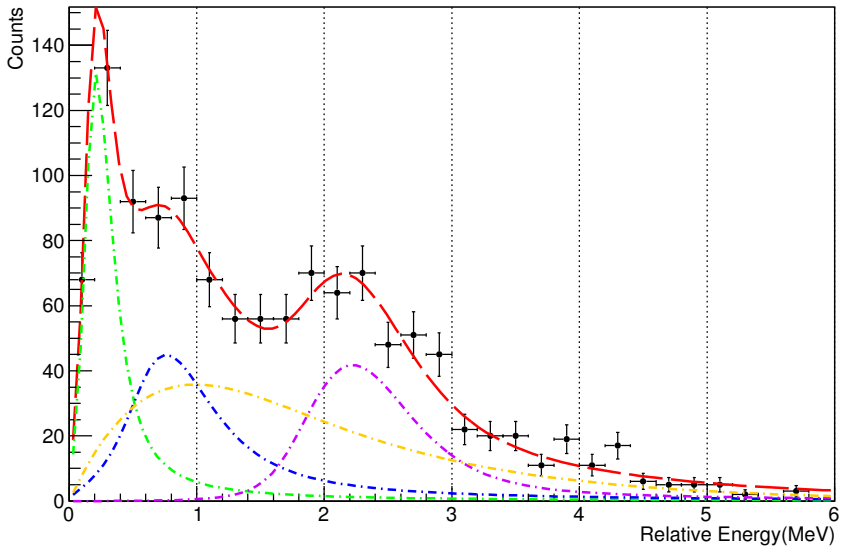

Figure 5.9: Visualization of the fit using three Breit Wigner functions with l=0 for the green line, l=0 for the blue line, l= 2 for the purple line. The global fit has a goodness of χ^2/N_{df}=1.15 and it is represented by the red line. The resonance Energies and the widths obtained are in table 5.5.

#	E_r(MeV)	Γ (MeV)	l
1	0.226(0.050)	0.195(0.034)	0
2	0.80(0.16)	0.743(fixed)	0
3	2.240(0.072)	0.383(0.036)	2
χ^2		21.89	
χ^2/N_{df}		1.15	

Table 5.5: Table of results considering three resonances with Non-Resonant Background and l=0,0,2. The visualization of the fit is displayed in figure 5.9.

The non-resonant background has been included in this case as well, despite it seems less necessary than when considering just two resonances. In these cases it leads to either unphysical widths of the resonances, specially for the second, or that the non-resonant background vanishes, being so small that it was unnoticeable.

In order to find a physical solution for these two cases the width of the second resonance has been fixed using the values calculated before without the background. The other previously calculated parameters were taken as initial input values. Looking at the values obtained (see tables 5.5 and 5.6), the reliability of both fits is high, having a value for $\chi^2/N_{df} \simeq 1.15$ that is almost the same. Again the second resonance is in the same position for both solutions, although there is a noticeable difference in the width. Figures 5.9 and 5.10 show the graphical output of the fit.

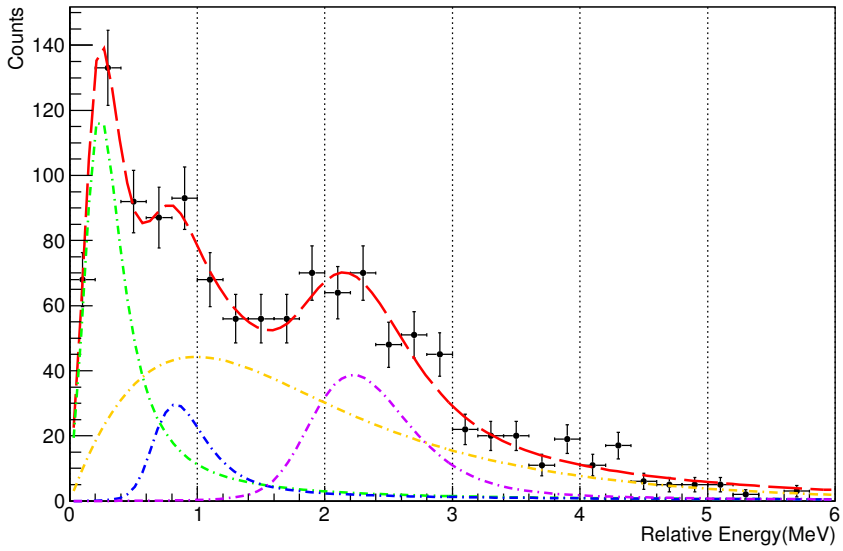

Figure 5.10: Visualization of the fit considering three Breit Wigner functions with l=0 for the green line, l=2 for the blue line, l= 2 for the purple line. The global fit has a goodness of χ^2/N_{df}=1.180 and it is represented by the red line. The resonance Energies and widths obtained are in table 5.6.

#	E_r(MeV)	Γ (MeV)	l
1	0.262(0.033)	0.312(0.007)	0
2	0.838(0.085)	0.29(fixed)	2
3	2.241(0.077)	0.268(0.036)	2
χ^2		22.43	
χ^2/N_{df}		1.180	

Table 5.6: Table of results considering three resonances with Non-Resonant Background and *l*=0,2,2. The visualization of the fit is displayed in figure 5.10.

5.2.4 Considering (p, 2p) reaction and Quasifree Scattering

The reactions with Quasifree scattering are cleaner (quasi-free) than a normal knockout reaction and are capable to excite deeper nucleons of the isotope structure. The Quasifree scattering correlations has been seen in the previous section 4.7, although to make it a requirement of the measurement, certain conditions must be imposed to the knocked out protons from the reaction ^{14}B (p, 2p) ^{13}Be such as 60° $< \Theta_{Op.Angle} <$110° and $\Delta\phi >$110° (see section 4.7 and in particular figure 4.13 and 4.14). These conditions leaves very low counts into the relative energy spectrum (385 counts), but despite the lack of statistics, detailed information can be gained from the spectrum. There are two main features to be pointed out: The resonance around 0.8-0.9 MeV is more evident, which will help to determine a more realistic width for an assigned resonance, and it is also worth to point out the count reduction within the tenth bin at 1.9 MeV, which suggests the possibility of splitting the broad resonance around 2 MeV in two different resonances peaked around 1.6 MeV and 2.2 MeV. However, none of the previous publications have reported two resonances in the area. Thus, in the following this counts suppression will be regarded as a statistical phenomena, and another resonance will not be considered in the fit.

The criterion of considering *l*=0,2 character of the first and last resonance will be followed, as well as the method of testing both angular momentum possibilities for the second resonance.

The error bars for the tenth bin has been increased (by two counts), this has been done due to its error is below the errors of the neighbour bins which produces too big changes in the parameters of the second and third resonance. This was also supported by comparing to the relative energy spectrum obtained requiring two protons in Crystal Ball but no Quasifree scattering conditions.

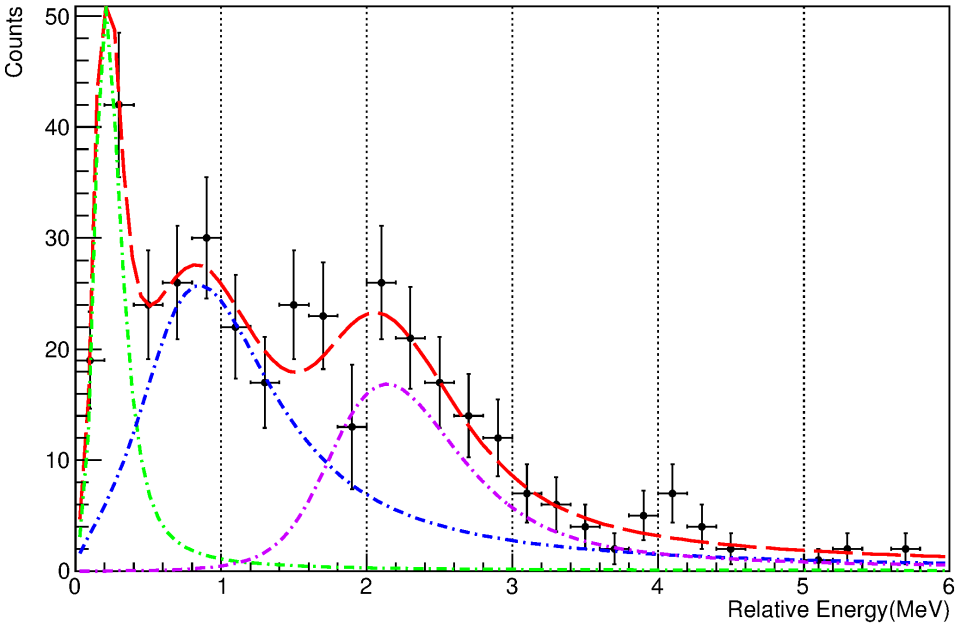

Figure 5.11: Visualization of the fit to a relative energy spectrum in coincidence with QFS scattering, the fit uses three Breit Wigner functions with l=0 for the green line, l=0 for the blue line, l= 2 for the purple line. The global fit has a goodness of χ^2/N_{df}=0.756 and it is represented by the red line. The resonance energies and widths obtained are in table 5.7.

#	E_r(MeV)	Γ (MeV)	l
1	0.214(0.083)	0.12(0.16)	0
2	0.92(0.17)	1.03(0.24)	0
3	2.16(0.21)	0.54(0.20)	2
χ^2		12.85	
χ^2/N_{df}		0.756	

Table 5.7: Table of fit results in coincidence with QFS, using in the fit three resonances and l=0,0,2. Figure 5.11 displays the visualization of the fit.

Looking at figures 5.11 and 5.12 seems evident that the result of the fit using l_1=0 is clearly dominated by the lowered tenth bin. Although the resonances positions are the same (within the broad error of the relative energy) in these cases, considering the Quasifree Scattering conditions and the previous fit without it. The resonance widths did not change much in the case of the l_1=2 (see tables 5.8 and 5.4), whereas for l_1=0, the widths are broader. However the uncertainties are bigger.

It is also worth to consider the goodness of the fits obtained , χ^2/N_{df} = 0.75 for l_1=0 and 0.82 for l_1=2. Both results are good, very close to 1 but starts to be below.

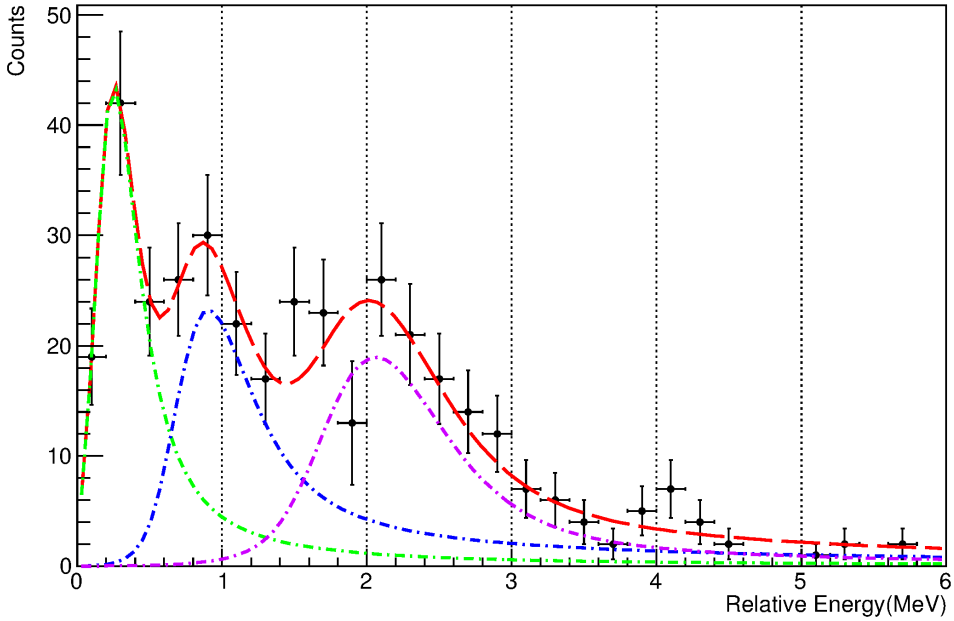

Figure 5.12: Visualization of the fit in coincidence with QFS scattering, it uses three Breit Wigner functions with l=0 for the green line, l=2 for the blue line, l= 2 for the purple line. The global fit has a goodness of χ^2/N_{df}=0.82 and it is represented by the red line. The resonance energies and widths obtained are in table 5.8.

#	E_r(MeV)	Γ (MeV)	l
1	0.279(0.054)	0.322(0.015)	0
2	0.949(0.16)	0.53(0.23)	2
3	2.08(0.17)	0.547(0.087)	2
χ^2		13.9	
χ^2/N_{df}		0.82	

Table 5.8: Table of results in coincidence with QFS, using three resonances and l=0,2,2. Figure 5.12 displays the visualization of the result.

In this case, including a non-resonant background has also been tried but the result has been even more chaotic than for the three resonances situation and after fixing certain values the obtained result has not been satisfactory. As was suggested in the section 5.1.2, the non-resonant background should not be very big due to the clean conditions previously settled, hence in this case after requiring a very restricting condition such as detecting two protons in coincidence, this background should be even lower and therefore negligible.

5.3 Discussion

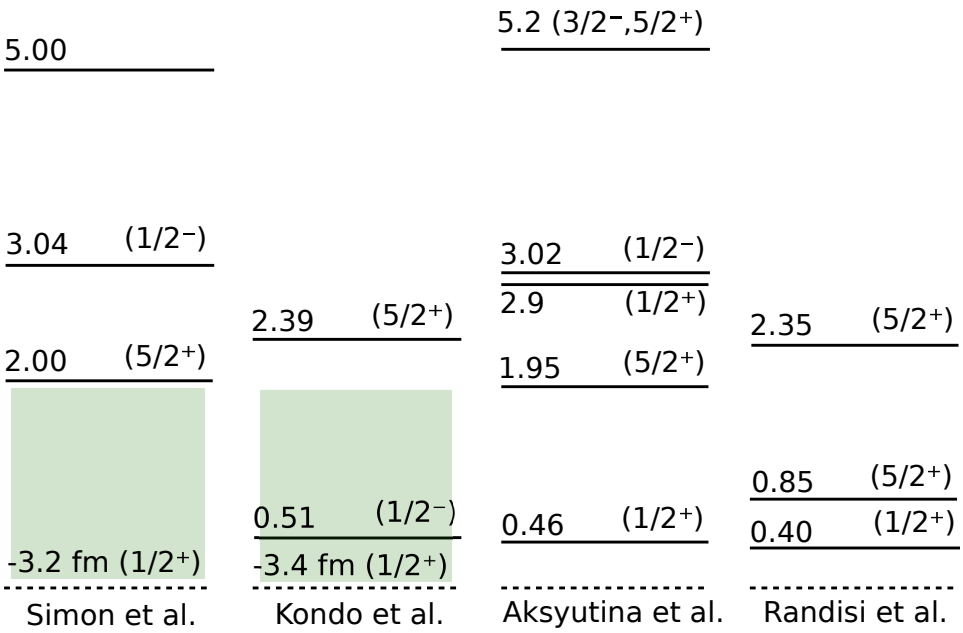

Figure 5.13: Comparison of the latest published experimental results of ^{13}Be.

In order to start the discussion it is necessary to remember certain assumptions that have been made for the analysis.

Previous studies of the incoming nucleus ^{14}B [86][87] have reported the domination of the components $2s_{1/2}$ and $2d_{5/2}$ on the valence neutron configuration which should be intact after the reaction ^{14}B(p,2p)^{13}Be of this experiment. That is why only s or d states were considered as options for the analysis. It is important to remember as well that ^{13}Be, since it is a neutron-rich unbound nucleus or resonance, in principle should not be able to hold s-states due to their lack of a centrifugal barrier, although as pointed by [40] ^{12}Be is a deformed nucleus without magicity despite having N=8,

thus the core is not inert and should provide the possibility of emerging s-states. Actually the latest experimental results published by Aksyutina et al [43] and Randisi et al [46] already considered the first low-energy state as a $1/2^+$ state, in contrast to several previous works like Kondo et al [42] and Simon et al [41] that were including an s-virtual state to describe the first resonance (see figure 5.13).

The case of the $5/2^+$ state at around 2 MeV is different, there seems to be a common agreement between the previous works on the existence of this state. However there is not an agreement on the exact position, which ranges between 1.8 and 2.4 MeV, whereas certain theoretical works set it even further, like Fortune [88][89] that places it 2.3 MeV above the first s-state, hence at >2.5 MeV.

The middle-ground resonance between the 0.2-0.5 MeV s-state and the ∼2 MeV d-state has been less investigated. Although older studies using the missing-mass method or Lecouey et al [40] have reported about a state around ∼ 0.8 MeV , but it was usually considered as the ground state (which in our structure is around 0.3 MeV). That is why
Aksyutina et al [43] conclude that the existence of a state below 1 MeV with a $l \neq 0$ character, should not be rejected. At the same time Randisi et al [46] did settled a $5/2^+$ state at 0.85 MeV based on his experimental results and in a theoretical calculus.

To reach a good interpretation of the present results it is also worth taking into account that the previous experiments did use a different projectile from the ^{14}B (^{14}Be is the most common) used in the s393 experiment, except from Lecouey et al [40] and Randisi et al [46] at GANIL. Fortune [89] suggested the existence of two s-states for ^{13}Be, the second around 3 MeV, this idea was followed by Aksyutina to describe their spectrum by fitting it to a model considering interference between these two states, giving good results. The broader low-energy region of the ^{14}B experiments was considered an outcome of a pure s-state.

The relative energy spectrum obtained in this experiment did not show much feature above 2.5 MeV. Although in the previous publications there is an agreement of a state around 5 MeV, whose momentum character is not clear as well as a state close to 3 MeV with $1/2^-$ momentum and therefore not fed by the ^{14}B beam.

The scenarios presented in section 5.2 only agree in the position of the last resonance ∼2.20 MeV. While the first resonance value ranges from 0.214 to 0.54 MeV. The low quality of the first fit (table 5.5) is basically due to the bad representation of the low and middle part of the relative energy spectrum, and thus makes it easy to discard the value at 0.54 MeV, and accept the lower energies.

A quick look at the spectrum may give the impression that the assumption of a resonance at ∼ 0.8 MeV is not realistic, the count increase between the 0.7 MeV and 0.9 MeV bin is clearly within the error bars, al-

though the lowering of the 1.1 MeV bin is noticeable. The fit of figure 5.6, considering a broad non-resonant background describing the middle energy-range is good, although the small width for the d-state would be smaller than the previous measurements, and such a value would not fit to a resonance that is clearly broad in all other measurements. But still there are two main reasons to argue in favour of a middle-range resonance:

- Two protons coincidence

  The coincidences with two protons in Crystal Ball (and the Quasifree conditions) shows a clear resonance in the area, and as stated before, this restrictive condition cleans more the miss-identificated events of a non-resonant background.

- Gamma coincidences

  Figure 4.12 shows that the bin at 0.7 MeV is favoured in coincidence with the 2.1 MeV gamma-ray from the ^{12}Be. Therefore this would indicate the presence of a feature in that area of the relative energy spectrum (a resonance peak). However, in the ^{13}Be structure would be related to a resonance at to $\sim$ 2.1 + 0.7 MeV $\simeq$ 2.8 MeV (see figure 5.14). This will be discussed more afterwards.

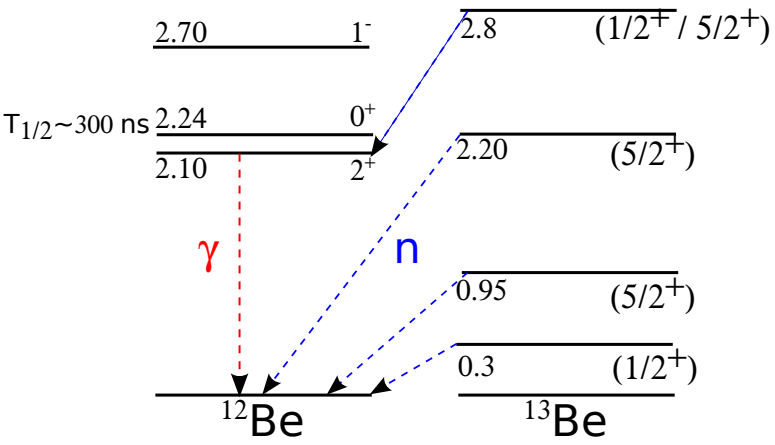

Figure 5.14: ^{13}Be structure proposed by this work. The neutron emissions are indicated in blue, whereas the only gamma-ray detected is indicated in red.

Once the inclusion of a third resonance has been clearly supported, it is worth to aim the discussion to the addition of the non-resonant background. Introducing a non-resonant background clearly complicates the three-resonance fit procedure. As it has been explained in section 5.2, it has not been possible to produce a clean fit without fixing certain parameters of

the Breit Wigner function. Constraining the values for the parameter A_1 to have a small or moderate background, led to more reasonable values of the resonances widths. But there has not been a way to set a definitive value for that parameter, and the method followed to find approximates values of the $A_{2,3}$ parameters is too rough.

Considering three resonances, the necessity of a non-resonant background might not be very relevant due to the tendency of the fitting function to minimize the background to very low values, as well as the cleanliness of the ^{13}Be channel with three coincidences needed: Incoming ^{14}B, outgoing ^{12}Be and one neutron selection. The very mentioned Aksyutina paper [43] neither included such a background reporting on a measurement made with the same setup (although lacking of a gamma detector) for the R3B Collaboration in a previous experiment. It is worth to remember as well, the difficulties to add the non resonant background to the fit of the spectrum in coincidence with the protons in Crystal Ball.

One aspect that the fit performed does not clarify if the l of the second resonance is 0 or 2. Both fits either considering Quasifree scattering coincidence or not have a good χ^2/N_{df}, although the l_2=0 case with χ^2/N_{df}=1.27 has a noticeable difference with the χ^2/N_{df} = 1.57 value for the l_2=2 case. In contrast, the energy value for the first resonance is always lower in the l_1=0 case which makes the result far from the last published results which set the energy value ∼0.4 MeV, at the same time looking at figures 5.9 and 5.11 the low energy resonance seems to be displaced to the left.

The two latest publications considered the possibility of such a state but both the momentum profile analysis performed by Aksyutina[43][45] and the theoretical calculations performed by Randisi [46] do not permit a l_2=0 state. It is also worth considering this state as a mixture of two (further discussion later on this subject).

Despite it has been mentioned before, it is important to remark what has been found in the gamma-ray analysis. The obtained result is quite different from the only work published that has measured gamma-rays in coincidence with the ^{12}Be fragment and one neutron, Kondo et al [42]. In our data we have only found one of the two possible gamma-rays emitted from the excited states of ^{12}Be: 2.1 MeV whereas Kondo et al were capable to find the 2.7 MeV gamma-ray as well. This is due to the lack of statistics. But this is not the only relevant difference between both measurements. The authors of [42] informs that the 2.1 MeV gamma-ray was correlated with events at very low relative energies of ∼0.2 MeV or less, whereas in this work the same gamma-ray has been correlated mainly with the a resonance close to 0.7 MeV (see figure 4.12). The last remark that must be done about the gamma-ray measurement is that the ^{12} Be 2.1 MeV state is a 2^+, therefore feeding this state must be done from a s or d state.

From the previous argumentation the second resonance of the relative energy spectrum could be considered as a mixture of two different

resonances, one at the mean value obtained of $\sim$ 0.95 MeV and another around the 0.7 MeV bin found in coincidence with the 2.1 MeV gamma-ray, thus the ^{13}Be state would be around 0.7 + 2.1 $\simeq$ 2.8 MeV. Such a state would be feeding the 2^+ state of the ^{12}Be by emitting a neutron from a state with $1/2^{+,-}$ or $5/2^+$. As this state would be >2.7 MeV, the excited states of ^{12}Be at 2.24 MeV (0^+) and 2.7 MeV(1^-) would be energetically allowed for feeding, however in our data there is no feature in the relative energy at $\sim$ 0.1 MeV and $\sim$ 0.6MeV, neither a gamma-ray of 2.7 MeV. Assuming J^p=5/2 for this resonance would agree with this since it would make those states almost forbidden. Previous measurements have reported about a $1/2^+$ state close to 2.9 MeV though.

It is worth to note that the resonance around 0.9 MeV can be considered as only one resonance (and not as a mixture of two), there is not enough statistics to know. In this case, this resonance would be located in the ^{13}Be at 0.95 + 2.1 $\simeq$ 3.05 MeV with a momentum character of 1/2 or 5/2.

Figure 5.14 represents the structure suggested by this work, supported by several of the previous fit results and this discussion. The fit closer to this conclusion is the one displayed in figure 5.12 which results are in table 5.8.

5.4 Conclusions and future

In the following I list the main conclusions extracted from this thesis as well as the future improvements one expect to obtain.

- The work reports on several possible resonance states of the unbound nuclei ^{13}Be and confirms some of the previously measured: One at 0.3 MeV with orbital angular momentum *l*=0 and another resonance with *l*=2 around 2.2 MeV. One feature in the area 0.7-0.9 MeV has also been found, although this state leaves a more opened panorama. See figure 5.14 for the proposed ^{13}Be structure. Figure 5.12 and table 5.8 holds the best fit to the proposed values.

- This is the first time that an experiment reports about the measurement of the unbound ^{13}Be nuclear structure using (p,2p) reactions with Quasifree scattering conditions.

- This is the second time that an experiment studying ^{13}Be has included a gamma-ray measurement. The results obtained are quite different from the previous. This time the ^{12}Be + neutron system was only found in coincide with the 2.1 MeV gamma-ray from ^{12}Be, this coincidence shows a resonance favoured at $\sim$ 0.7 MeV.

- The resonance fit around 0.9 MeV in combination with the 2.1 MeV gamma-ray in coincidence with a feature at 0.7 MeV leads us to un-

derstand this relative energy feature as a combination of a resonance around 0.9 and another at 2.1 MeV + 0.7 MeV $\sim$ 2.8 MeV. The state at 0.9 MeV would be $5/2^+$ as has been settled in a previous publication whereas the state at 2.8 MeV could be $1/2$ or $5/2$.

- The lack of statistics as well as the broad relative energy resolution, especially above 3 MeV, has made impossible to extract more definitive conclusions. Despite this problems, this work has been capable of confirming previous results and proposing new resonances using the reaction ^{14}B (p,2p)^{13}Be.

- The non-resonant background has not been found necessary to include in this case.

- An improvement in every part of the setup used is currently under development for the FAIR facility. The gamma measurement will be improved by the new detector CALIFA. The protons coming out from the reaction would be much easily found with the Silicon Tracker as well as CALIFA, improving the efficiency and energy resolution. NeuLAND will take care of the neutrons and will help to improve the angular resolution which is the main constrain for the relative energy determination. These new detectors in combination with far more intense radioactive beams will help to improve the results obtained.

- Besides the resolution, efficiency and beam intensity improvements already planned, there is no information about the possible feeding to the other 0^+ isomeric state of the ^{12}Be at 2.24 MeV. An experiment capable of measuring a long-lived state after producing ^{13}Be would contribute further to the current knowledge about this exotic nuclei.

A Summary

A.1 Introduction

Light nuclei close to the dripline are weakly bound, thus they usually do not have particle-bound excited states, nevertheless it is possible to feed excitations in the continuum. It is even possible to produce and observe certain combinations of protons and neutron that are beyond the dripline, such systems without bound states are known as unbound nuclei.

At the limit of the dripline, new structures like the halo, Borromean nuclei emerges. The Borromean structure is bound while the two possible subsystems, isotope + nucleon or nucleon + nucleon are unbound. Hence, this produces certain pairs of isotopes that the odd neutron-numbered is unbound while the even neutron-numbered is bound. In order to understand this kind of exotic structure, the study of the unbound systems is thus needed.

The theoretical nuclear models, due to the difficulties of the many-body problem, are still not able to describe in a general way the nuclear force. The unbound systems are laboratories to test the theoretical models for the interaction between a core and single neutron above or on the limits of the nuclear force.

The aim of this work is to determine the shell structure of ^{13}Be, a neutron-rich unbound nucleus, using a knockout (p , 2p) reaction. This Beryllium isotope has been controversial over the last years, being the target of several studies. The interest of these nuclei is because is a middle step between the ^{14}Be Borromean nuclei and ^{12}Be. Studying this nuclei have been complicated due to the amount of resonances found in previous studies. It was not possible to set unambiguously the position of certain of those resonances because of the inability of the analysis method (invariant mass) to make a difference between the decays of ^{13}Be to excited states or ground state of the ^{12}Be. In order to avoid these ambiguities is necessary to measure in coincidence the emitted gamma-rays from ^{12}Be excited states. The experiment studied in this work includes a gamma ray detector, unlike all previous experiments except one [42].

The reaction channel used to fed the isotope of interest is ^{14}B(p, 2p)^{13}Be, where the Boron beam is impinged on a CH_2 target and a proton is knocked out from the beam producing ^{13}Be. At the high energies used (490 MeV/u), Quasifree Scattering conditions can be fulfilled for the reaction which can extract out deeper bound protons. Two protons are knocked out very energetically, the rest of the projectile is not involved in the reaction process, acting as a spectator. Therefore the interaction can be considered as Quasifree, in first approximation other kind of interactions does not need to be taken into account. Both protons are emitted in the same plane, and with an opening angle of $\sim$82° in the laboratory frame.

Few previous experiments uses ^{14}B as a beam, most of them have used ^{14}Be, and none of them have included Quasifree scattering conditions in their reaction.

A.2 Experimental setup

The data used in this thesis is coming from the S393 experiment performed in the late summer of 2010 at GSI Helmholtzzentrum für Schwerionen-forschung GmbH by the R3B Collaboration.

At GSI an ion source produce the primary beam which is begin to be accelerated in the linear accelerator (UNILAC) and send to the synchrotron (SIS18) in order to reach higher energies, for the S393 experiment the primary beam of ^{40}Ar was accelerated up to 490 MeV/u. When the beam is extracted from the accelerator it is let to impinge on a light target, this experiment used Beryllium of 4011 mg/cm^2, that produces a cocktail of particles which goes through the Fragment Separator (FRS) that separates the different species before reaching the R3B experimental hall: Cave C, where the detectors are setup.

The main feature of this detector setup is being capable to make complete kinematic measurements, this means that is able to record all the information including energy, mass and charge from the different incoming isotopes and the outgoing reaction products. The setup can be divided in three different stages following the position and purpose of the detectors: Incoming, around the target and outgoing.

- **Incoming beam detectors**

  The goal of this part of the setup is the identification of the different isotopes that are coming in from the Fragment Separator. The PSP detector is a square plate of silicon which measure the energy loss of the nuclei in order to identify the charge. One scintillator in the last section of the FRS (S8) and a another at the entrance of the experimental hall (POS) are in charge of measuring the Time of Flight of the isotopes to distinguish the charge/mass ratio. The combination of both

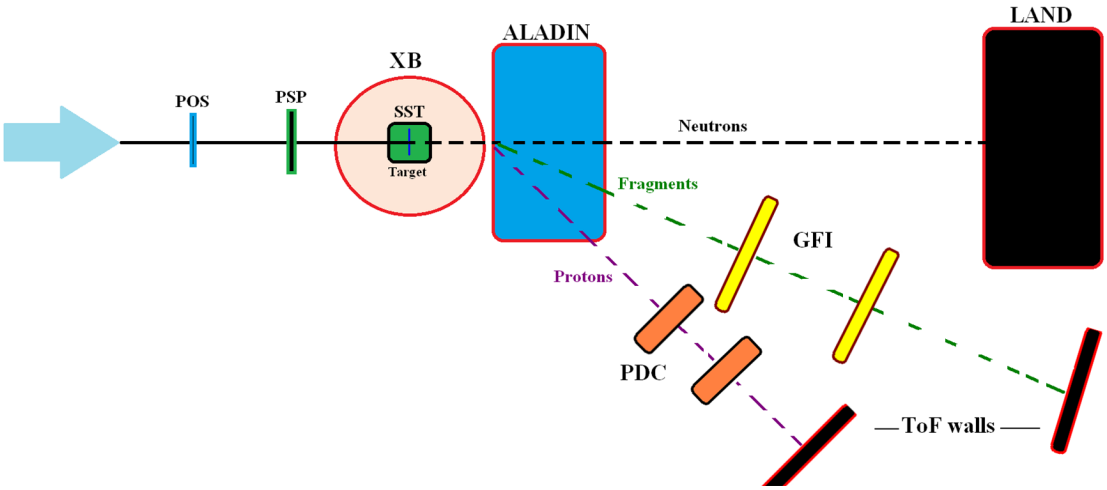

Figure A.1: Simplified scheme of the setup, the figure 2.5 has a more detailed representation. The proton branch after the ALADIN magnet is not used in this work.

measurements allow to identify the incoming nuclei of the beam that reach the R3B setup. In this stage there is also the ROLU which is a combination of four scintillators that can adjusted to the required beam size, if a particle produces a signal in one of the scintillators, the event is discarded.

- **Around the target detectors**

  In the experiment three different targets were used:
  Carbon (935 mg/cm^2), Lead (2145 mg/cm^2) and the most relevant for this thesis, Polyethylene (CH_2 with 922 mg/cm^2). The targets are fixed to a wheel which allow their selection. Close to this target wheel, there are four DSSDs, two in front of the target and two behind. Their purpose is measuring the interaction angle with the target and their outgoing angle. They are also in charge of measuring measuring the energy loss of the outgoing fragments to identify their charge. Surrounding the target and the silicons there is Crystal Ball, an spherical detector of 162 NaI scintillators to detect the gamma rays emitted after the reaction, it is also capable of measuring the two protons knocked out in the (p, 2p) reactions.

- **Outgoing fragments detectors**

  After the target there is a large dipole called ALADIN that bends the trajectories of the charged particles coming out from the reaction. The

nuclei fragments are directed by the magnet through a pair of fiber detectors (GFI) to track them, at the end of the detector branch there is a scintillator wall called TFW to measure the time of flight and the energy loss of each nuclei, which allows to identify the charge. The neutrons trajectory is not bend by the magnet, therefore they continue straight until reaching a bigger scintillator wall (LAND) that measures the time of flight, energy and direction of the emitted neutrons.

A.3 Analysis method

In order to extract information on the structure of ^{13}Be we have followed the invariant mass method. The idea behind is the reconstruction of the energy of the nuclei from the detection of the fragment ^{12}Be and the neutron. However if the ground state mass of the residual nucleus and the neutron is subtracted to the energy they have , a relative energy spectrum is produced which gives information about the resonances fed in the unbound ^{13}Be.

$$E_{rel} = \sqrt{M_{^{12}Be}^2 + m_n^2 + 2 \cdot m_n M_{^{12}Be} \gamma_n \gamma_{^{12}Be} [1 - \beta_n \beta_{^{12}Be} \cdot cos(\theta_{^{12}Be-n})]} - M_{^{12}Be} - m_n$$

The equation shows that only three parameters are relevant; the angle between the outgoing fragment (^{12}Be) and the neutron($\theta_{^{12}Be-n}$), and the velocity of each. The procedure to extract that parameters is the following; from the cocktail beam of the FRS the ^{14}B must be selected avoiding contamination from other isotopes. From the reaction products, it must be selected the Z=4 charge (Beryllium), using the DSSDs behind the target. Using the complete kinematics detection system it is possible to separate the different masses of the reaction products, thus the A=12 mass must be selected. Once the fragment has been isolated, the next step is choosing the events with one neutron in LAND. Therefore the reaction channel is cleaned up and the angle and the velocities can be extracted.

The relative energy spectrum that has been calculated shows several resonances that can be identified as resonances of the ^{13}Be. In order to set their positions and widths they must be fitted using Breit-Wigner functions which are capable to describe this kind of states,

$$\frac{d\sigma}{dE} \sim \frac{\Gamma(E)}{(E_r - E)^2 + \frac{\Gamma(E)^2}{4}}.$$

Where,

$$\Gamma(E) = 2\gamma^2 P_l(\rho, \eta).$$

The Breit-Wigner expression only has two parameters free to be fitted; the reduced width of the resonance γ , and the resonance energy E_r. The function obtained has to be folded with detector resolution.

When the ^{13}Be is produced, several resonant energies can be fed, therefore the neutron decay can populate different states in ^{12}Be. In order to clarify the ^{13}Be structure the invariant mass method is not enough as the spectrum only shows the energy between the neutron and the fragment, but it cannot distinguish between different excitations of the ^{12}Be. Unless the only fed state of the fragment is the ground state, the measurement has to be complemented by gamma detection, otherwise different ^{13}Be resonances decaying to different ^{12}Be states will contribute to the same relative energy peak of the spectrum.

^{12}Be has three possible excited states in the energy range of this analysis, thus two possible gamma-rays at 2.1 and 2.7 MeV can be measured. The third state at 2.24 MeV is an isomeric state with a long lifetime and will escape Crystal Ball before decaying and so avoid detection.

A gamma-ray was found at 2.15$\pm$0.02 MeV which corresponds to the 2.1 MeV gamma-ray. The next step is to find a correlation between this gamma ray and any of the resonances of the ^{12}Be + n relative energy spectrum. The gamma-ray peak has been gated-on and the result is dominated by the uncorrelated counts below it. In order to clean it, the gamma spectrum has been gated off-peak on both sides and a mean of the two relative energy spectra has been performed. This mean spectrum has been subtracted from the on-peak gated spectrum, the result (see figure A.2) shows two favoured bins at 0.3 and 0.7 MeV.

Due to the low statistics is not easy to draw a conclusion from figure A.2. It seems obvious that there is no correlation with any medium or high energy resonance, as the relative energy spectrum seems rather flat above 1 MeV. The two bins at 0.3 and 0.7 MeV are favoured and the bin at 0.5 MeV is suppressed. Hence, it can be understood as both possible resonances located around those bins are partially fed by a ^{13}Be state that decay at the 2.1 MeV ^{12}Be state. However the second bin of the relative energy spectrum at 0.5 MeV is the highest and in figure A.2 is lower than the fourth, as the total amount of counts in the peak area was higher than the amount subtracted from the off-peak events, thus it is possible that this low-energy resonance is still uncorrelated from the gamma ray.

Despite that the previous requirements for the outgoing channel are very selective (incoming ^{14}B + ^{12}Be + n), observing two outgoing high-energy protons with QuasiFree conditions in Crystal Ball would clarify the complete picture of the reaction, however we are limited by the statistics. The angular correlations of the Quasifree scattering are found, although the number of counts for the relative energy spectrum is lowered from 1257 to 487 in coincidence with two protons in Crystal Ball.

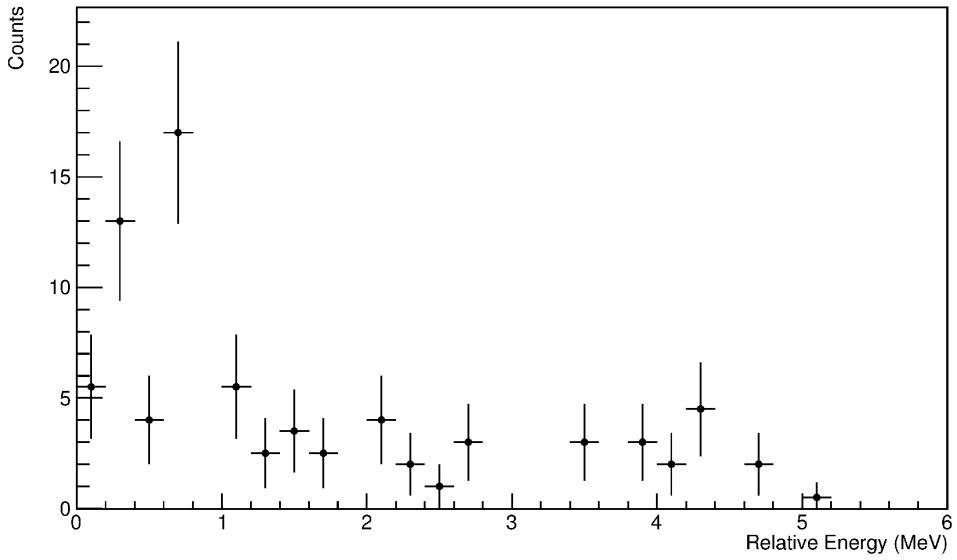

Figure A.2: ^{13}Be Relative energy spectrum after subtraction of the uncorrelated events. The only bins still favoured are the second and the fourth at 0.3 and 0.7 MeV.

A.4 Results

The relative energy of the ^{12}Be + n system has been fitted to several Breit-Wigner functions. The minimization method followed has been the χ^2 approach with the MINUIT tool.

Despite the reaction channel should be rather clean after the previous selections, it is likely that there are events within the spectrum that are the result of a wrong identification either from the incoming or outgoing fragment or the neutron detected. In order to take into account such misidentification a Non-resonant Background has been modeled with the following equation. The model has a negative exponential function and an Error Function with three parameters: $A_{1,2,3}$.

$$E_{NR} = A_1 \cdot e^{-A_2 E} \cdot erf(A_3 E)$$

However the inclusion of this function to the fits had make the results more chaotic and it is not clear that it inclusion made a significant difference to the results.

A.4.1 Considering two resonances

Previous studies have determined only two resonances within the range of 0-2.5 MeV for the ^{13}Be nuclei. Thus, although the fifth bin of the

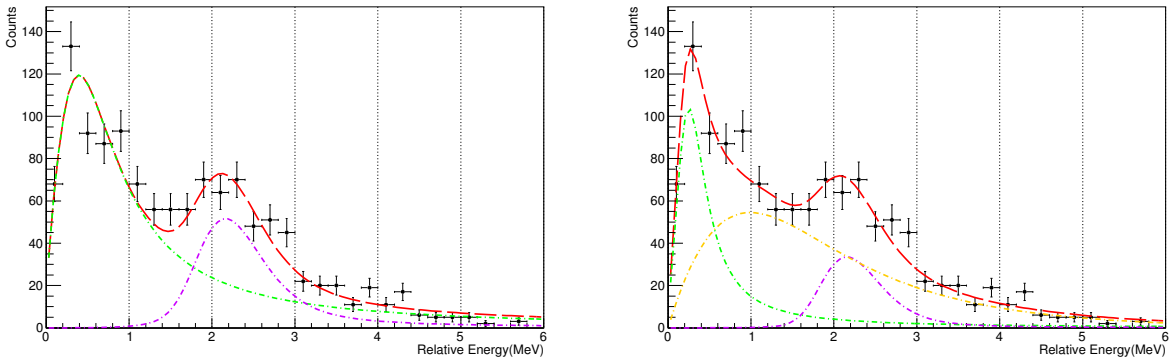

(a) (b)

Figure A.3: Visualization of the fits considering two resonances with l=0 (green) and 2 (purple). (a): Without including Non-Resonant background.(b): Including Non-Resonant background (yellow). The results of the fit can be seen in table A.1

		Not Including NRB		Including NRB	
#	l	E_r(MeV)	Γ (MeV)	E_r(MeV)	Γ (MeV)
1	0	0.54(0.04)	1.185(0.002)	0.287(0.038)	0.411(0.008)
2	2	2.18(0.06)	0.381(0.009)	2.18(fixed)	0.176(0.034)
χ^2		49.2588		29.04	
χ^2/N_{df}		2.23903		1.32	

Table A.1: Table of results considering two resonances with l=0,2. The two cases with and without Non-Resonant Background are included. The visualization of the fit can be seen in figure A.3.

histogram shows an increment and a significant difference with the sixth bin, it should be considered the option of only two open resonances. A low energy state with l=0 and another close to 2 MeV with l=2 are initially considered.

A fit without a non-resonant background has been made,but the result (see figure A.3(a)) shows that the first Breit-Wigner function alone is not capable to make a good approximation for its range. The χ^2/N_{df}= 2.23903 indicates the low-quality of this fit.

In order to improve the fit a non-resonant background has been included,to get a result with physical meaning it has been necessary to fix a parameter, the resonance position of the second curve E_r=2.18±0.06 MeV. It was chosen because it is the least affected by the inclusion of the background. The results of the fit can be seen in table A.1, the value χ^2/N_{df}=1.32

has been improved significantly. Even though the background gives a better description of the area 0.7-1.7 MeV, it almost skip the count increment in the 0.9 MeV bin, as can be seen in figure A.3(b), however the description of the low-energy part of the spectrum has improved.

A.4.2 Considering three resonances

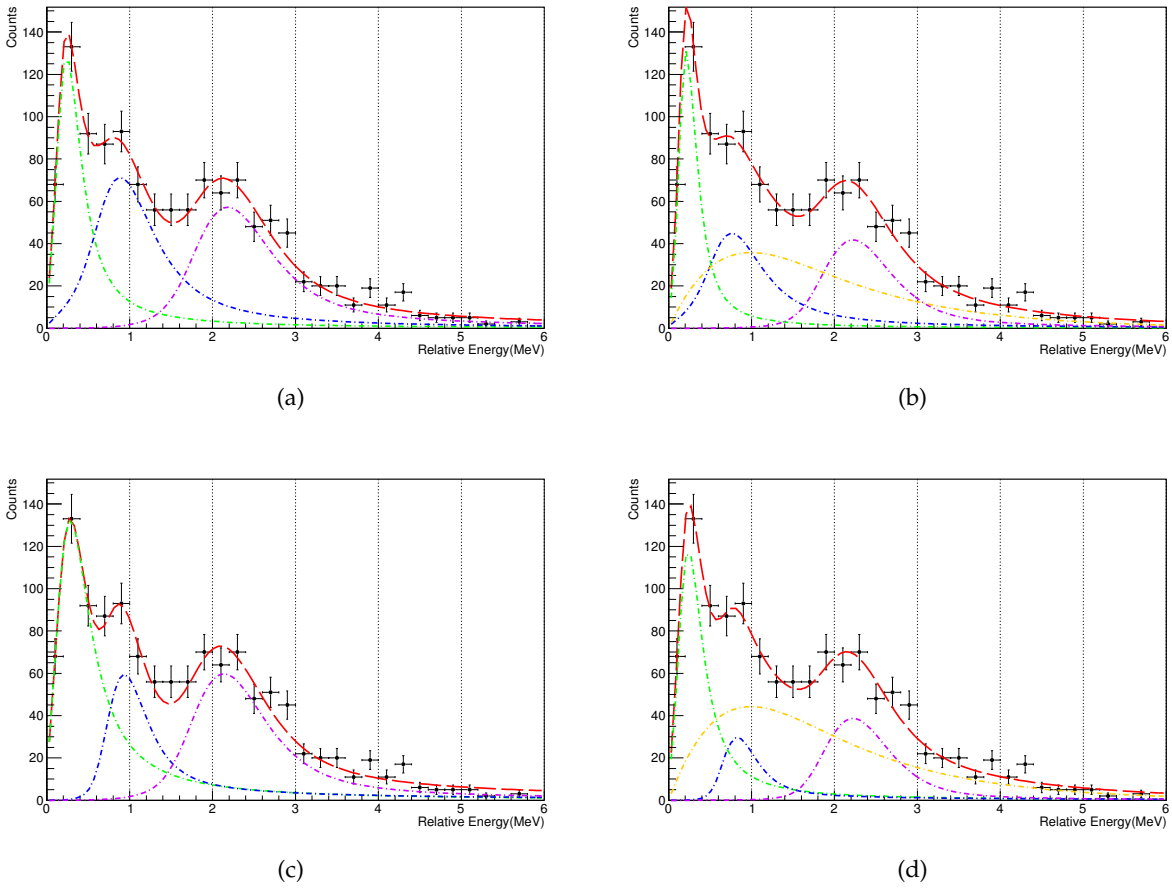

Figure A.4: Visualization of the fits considering three resonances. There are results with two options,considering l_2=0,2, as well as including or not the Non-Resonant background. (a): Without including Non-Resonant background and l=0 (green) , 0 (blue), 2 (purple).(b): Including Non-Resonant background (yellow) and l=0,0,2.(c): Without including Non-Resonant background and l=0,2,2.(d): Including Non-Resonant background and l=0,2,2. The results of the fit can be seen in table A.2.

Previous publications have considered the inclusion of a s-or-p state in the region between the low energy s-state and the d-state at 2 MeV [46].

		Not Including NRB		Including NRB	
#	l	E_r(MeV)	Γ (MeV)	E_r(MeV)	Γ (MeV)
1	0	0.265(0.048)	0.319(0.013)	0.226(0.050)	0.195(0.034)
2	0	0.929(0.080)	0.741(0.029)	0.80(0.16)	0.743(fixed)
3	2	2.209(0.064)	0.635(0.064)	2.240(0.072)	0.383(0.036)
χ^2		24.126		21.89	
χ^2/N_{df}		1.26978		1.15	
#	l	E_r(MeV)	Γ (MeV)	E_r(MeV)	Γ (MeV)
1	0	0.333(0.036)	0.5196(0.0054)	0.262(0.033)	0.312(0.007)
2	2	0.951(0.055)	0.29(0.026)	0.838(0.085)	0.29(fixed)
3	2	2.157(0.058)	0.5845(0.0076)	2.241(0.077)	0.268(0.036)
χ^2		29.9		22.43	
χ^2/N_{df}		1.574		1.180	

Table A.2: Table of results considering three resonances. There are results with two options,considering l_2=0,2, as well as including or not the Non-Resonant background. The visualization of the fit can be seen in figure A.4.

In order to try to reproduce the count increment of the fourth and fifth bin (0.7-0.9 MeV), another Breit-Wigner function has been introduced into the fit, within the energy range 0.6 - 1.2 MeV. The two possible orbital momentum l= 0,2 have been considered.

The non-resonant background has been included in this case as well, despite it seems less necessary than when considering just two resonances. In these cases it leads to either unphysical widths of the resonances, specially for the second, or that the non-resonant background vanishes, being so small that it was unnoticeable. In order to find a physical solution for these two cases the width of the second resonance has been fixed using the values calculated before without the background.

The result obtained did not lead to significant changes in the resonance positions although the widths have noticeable changed.

A.4.3 Considering (p, 2p) reaction and Quasifree Scattering

Despite the low number of counts, the relative energy spectrum of the system ^{12}Be + neutron imposing Quasifree scattering conditions has been studied as well. The angular correlations conditions for the two protons in Crystal Ball has been $60^\circ < \Theta_{Op.Angle} < 110^\circ$ and $\Delta\phi > 110^\circ$, which has lead to an spectrum with only 385 counts.

There are two main features to be pointed out: The resonance around 0.8-0.9 MeV is more evident, which will help to determine a more realistic width for an assigned resonance, and it is also worth to point out the count reduction within the tenth bin at 1.9 MeV, which suggests the possibility

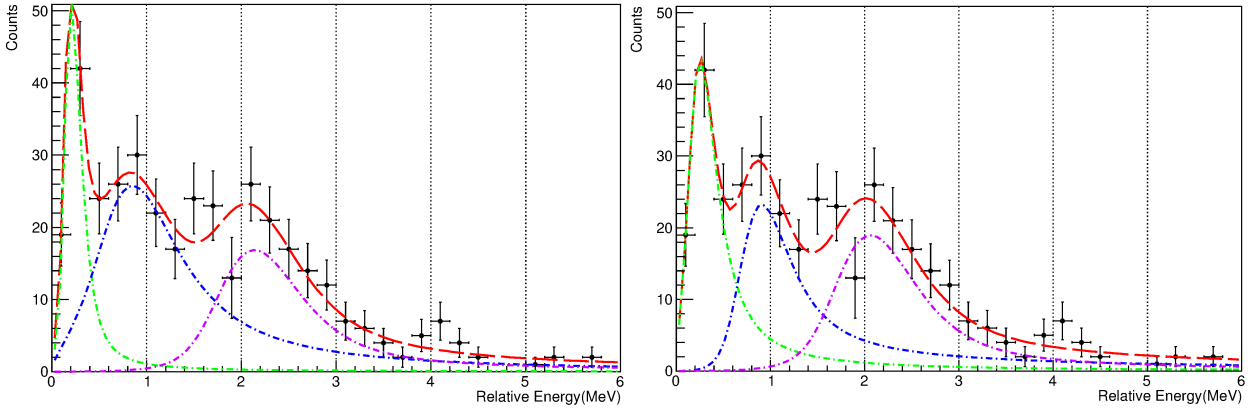

(a) (b)

Figure A.5: Visualization of the fits considering three resonances with QFS conditions and considering the two options of l_2=0,2 . (a):In this case l=0 (green),0 (blue),2(purple).(b):This case considered l=0,2,2. The results of the fit can be seen in table A.3

#	l	E_r(MeV)	Γ (MeV)
1	0	0.214(0.083)	0.12(0.16)
2	0	0.92(0.17)	1.03(0.24)
3	2	2.16(0.21)	0.54(0.20)
χ^2		12.85	
χ^2/N_{df}		0.756	
#	l	E_r(MeV)	Γ (MeV)
1	0	0.279(0.054)	0.322(0.015)
2	2	0.949(0.16)	0.53(0.23)
3	2	2.08(0.17)	0.547(0.087)
χ^2		13.9	
χ^2/N_{df}		0.82	

Table A.3: Table of results considering three resonances with QFS conditions. There are results with two options,considering l_2=0,2. The visualization of the fit is in figure A.5.

of splitting the broad resonance around 2 MeV in two different resonances peaked around 1.6 MeV and 2.2 MeV. However, none of the previous publications have reported two resonances in the area. Thus, in the following this counts suppression will be regarded as a statistical phenomena, and another resonance will not be considered in the fit.

The error bars for the tenth bin has been increased (by two counts), this has been done due to its error is below the errors of the neighbour bins

which produces too big changes in the parameters of the second and third resonance. This was also supported by comparing to the relative energy spectrum obtained requiring two protons in Crystal Ball but no Quasifree scattering conditions.

In this case, including a non-resonant background has been tried but the result has been even more chaotic and is likely to be not necessary after requiring the Quasifree scattering conditions.

A.5 Discussion

In order to start the discussion it is necessary to remember certain assumptions that have been made for the analysis.

Previous studies of the incoming nucleus ^{14}B [86][87] have reported the domination of the components $2s_{1/2}$ and $2d_{5/2}$ on the valence neutron configuration which should be intact after the reaction ^{14}B(p,2p)^{13}Be of this experiment. That is why only s or d states were considered as options for the analysis.

The resonances around 0.4 MeV and 2 MeV with $1/2^+$ and $5/2^+$ character has been found in several previous publications, that is why two resonances with such angular momentum (l=0,2) in those areas has always been considered.

The scenarios presented in the result section are only coincident in the position of the last resonance ∼2.20 MeV. However the first resonance value ranges from 0.214 to 0.54 MeV but the higher values can be discarded.

Other studies have taken into account the possible existence of a state close to or below 1 MeV with $l \neq 0$, whereas other have even reported about one around 0.7-0.85 MeV but it has much less previous investigation.

The assumption of a resonance around 0.8-0.9 MeV is clearly supported after imposing the QuasiFree scattering conditions, where a feature in that position is clearly favoured. The two latest publications considered the possibility of such a state but both the momentum profile analysis performed by Aksyutina[43][45] and the theoretical calculations performed by Randisi [46] do not permit a l_2=0 state.

It is important to remark what has been found in the gamma-ray analysis. The obtained result is quite different from the only work published that has measured gamma-rays in coincidence with the ^{12}Be fragment and one neutron, Kondo et al [42]. In our data we have only found one of the two possible gamma-rays emitted from the excited states of ^{12}Be: 2.1 MeV whereas Kondo et al were capable to find the 2.7 MeV gamma as well. This is due to the lack of statistics. But this is not the only relevant difference between both measurements. The authors of [42] informs that the 2.1 MeV gamma-ray was correlated with events at very low relative energies of ∼0.2 MeV or less, whereas in this work the same gamma-ray has been correlated

mainly with the second resonance close to 0.7 MeV, even though a partial feeding to both energy levels cannot be discarded. The last remark that must be done about the gamma-ray measurement is that the ^{12} Be 2.1 MeV state is a 2^+, therefore feeding this state must be done from a s or d state.

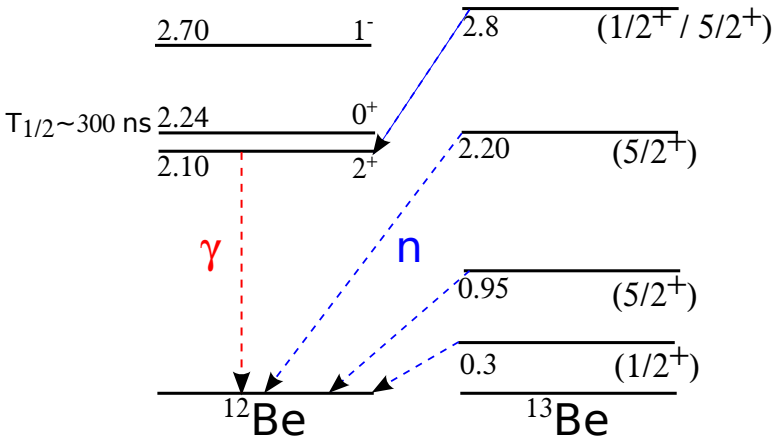

Figure A.6: ^{13}Be structure proposed by this work. The neutron emissions are indicated in blue, whereas the only gamma-ray detected is indicated in red.

From the previous argumentation the second resonance of the relative energy spectrum could be considered as a mixture of two different resonances, one at the mean value obtained of $\sim$ 0.95 MeV and another around the 0.7 MeV bin found in coincidence with the 2.1 MeV gamma-ray, thus the ^{13}Be state would be around 0.7 + 2.1 $\simeq$ 2.8 MeV. Such a state would be feeding the 2^+ state of the ^{12}Be by emitting a neutron from a state with $1/2^{+,-}$ or $5/2^+$. As this state would be >2.7 MeV, the excited states of ^{12}Be at 2.24 MeV (0^+) and 2.7 MeV(1^-) would be energetically allowed for feeding, however in our data there is no feature in the relative energy at $\sim$ 0.1 MeV and $\sim$ 0.6MeV, neither a gamma-ray of 2.7 MeV. Assuming J^p=5/2 for this resonance would agree with this since it would make those states almost forbidden. Previous measurements have reported about a $1/2^+$ state close to 2.9 MeV though.

It is worth to note that the resonance around 0.9 MeV can be considered as only one resonance (and not as a mixture of two), there is not enough statistics to know. In this case, this resonance would be located in the ^{13}Be at 0.95 + 2.1 $\simeq$ 3.05 MeV with a momentum character of 1/2 or 5/2.

Figure A.6 represents the structure suggested by this work, supported by several of the previous fit results and this discussion. The fit closer to this conclusion would be the one showed in figure A.5(b) which results are in table A.3.

A.6 Conclusions

In the following I list the main conclusions extracted from this thesis as well as the future improvements one expect to obtain.

- The work reports on several possible resonance states of the unbound nuclei ^{13}Be and confirms some of the previously measured: One at 0.3 MeV with orbital angular momentum l=0 and another resonance with l=2 around 2.2 MeV. One feature in the area 0.7-0.9 MeV has also been found, although this state leaves a more opened panorama. See figure A.6 for the proposed ^{13}Be structure. Figure A.5 and table A.3 holds the best fit to the proposed values, considering l_2=2.

- This is the first time that an experiment reports about the measurement of the unbound ^{13}Be nuclear structure using (p,2p) reactions with Quasifree scattering conditions.

- This is the second time that an experiment studying ^{13}Be has included a gamma-ray measurement. The results obtained are quite different from the previous. This time the ^{12}Be + neutron system was only found in coincide with the 2.1 MeV gamma-ray from ^{12}Be, this coincidence shows a resonance favoured at $\sim$ 0.7 MeV.

- The resonance fit around 0.9 MeV in combination with the 2.1 MeV gamma-ray in coincidence with a feature at 0.7 MeV leads us to understand this relative energy feature as a combination of a resonance around 0.9 and another at 2.1 MeV + 0.7 MeV $\sim$ 2.8 MeV. The state at 0.9 MeV would be $5/2^+$ as has been settled in a previous publication whereas the state at 2.8 MeV could be $1/2$ or $5/2$.

- The lack of statistics as well as the broad relative energy resolution, especially above 3 MeV, has made impossible to extract more definitive conclusions. Despite this problems, this work has been capable of confirming previous results and proposing new resonances using the reaction ^{14}B (p,2p)^{13}Be.

- The non-resonant background has not been found necessary to include in this case.

- An improvement in every part of the setup used is currently under development for the FAIR facility. The gamma measurement will be improved by the new detector CALIFA. The protons coming out from the reaction would be much easily found with the Silicon Tracker as well as CALIFA, improving the efficiency and energy resolution. NeuLAND will take care of the neutrons and will help to improve the angular resolution which is the main constrain for the relative energy

determination. These new detectors in combination with far more intense radioactive beams will help to improve the results obtained.

- Besides the resolution, efficiency and beam intensity improvements already planned, there is no information about the possible feeding to the other 0^+ isomeric state of the ^{12}Be at 2.24 MeV. An experiment capable of measuring a long-lived state after producing ^{13}Be would contribute further to the current knowledge about this exotic nuclei.

B Resumen en castellano

B.1 Introducción

Los núcleos ligeros cerca de la línea de goteo están muy debilmente ligados, por tanto, por lo general no tienen estados ligados excitados, sin embargo si que es posible poblar excitaciones en el continuo. Incluso es posible producir y observar ciertas combinaciones de protones y neutrones que están más allá de la línea de goteo, tales sistemas que carecen de estados ligados son conocidos como núcleos no-ligados.

En los límites de la línea de goteo, otras estructuras como los núcleos halo Borromeos aparecen. Esta estructura es ligada mientras que los dos subsistemas que lo forman, isótopo + nucleón o nucleón + nucleón son no-ligados. Por lo tanto, esto produce determinados pares de isótopos donde el que tiene un número impar de neutrones no está ligado, mientras que el que tiene un número par, si lo está. Para entender este tipo de estructuras exóticas es por tanto necesario estudiar lo sistemas no-ligados.

Los modelos teóricos nucleares, debido a las dificultades que entraña el problema de muchos-cuerpos, todavia no son capaces de describir de forma general la fuerza nuclear. Los sistemas no-ligados son laboratorios donde probar los modelos teóricos para la interacción entre un núcleo y un solo neutrón en los límites de la fuerza nuclear.

El objetivo de este trabajo es el estudio de la estructura de capas del ^{13}Be, un núcleo no-ligado rico en neutrones, utilizando una reacción (p, 2p) de *knockout*. Este isótopo de Berilio ha sido controvertido a lo largo de los últimos años, lo que le ha convertido en el objetivo de varios estudios. El interés de este núcleo se debe a que, como se explicó antes, es un paso intermedio entre el núcleo Borromeo ^{14}Be y el ^{12}Be. Estudiar este nucleo se ha complicado por la cantidad de resonancias encontradas en los estudios previos. No ha sido posible determinar inequivocamente la posición de algunas de dichas resonancias debido a la incapcidad del método de análsis para diferencias entre el decaimiento del ^{13}Be a estados excitados o el fundamental del ^{12}Be. Para evitar estas ambiguedades es necesario medir en coincidencia los rayos gamma de los estados excitados del ^{12}Be. El experi-

mento que es objeto de estudio en este trabajo incluye un detector de rayos gamma, a diferencia de todos los experimentos previos excepto uno [42].

El canal de reacción utilizado para poblar el isótopo de interes es ^{14}B(p, 2p)^{13}Be, donde el haz de Boro se hace incidir sobre un blanco de polietileno CH_2, provocando la perdida de un proton en el haz y produciendo ^{13}Be. A las altas energías utilizadas (490 MeV / u) las condiciones de dispersión *cuasi-libre* se pueden cumplir y extraer protones de capas más profundamente ligadas. Con estas condiciones dos protones, uno del blanco y otro del haz son emitidos muy energeticamente en la reacción, mientras que el resto del blanco y el proyectil no interaccionan, actuando como espectadores. Por lo tanto la interacción se puede considerar como cuasi-libre. En primera aproximación otras interacciones no necesitan ser tenidas en cuenta. Ambos protones se emiten en el mismo plano, y con un ángulo de apertura de $\sim$82° en el sistema de referencia del laboratorio.

Muy pocos experimentos previos han utilizado ^{14}B como haz, la mayoría han utilizado ^{14}Be y ninguno de ellos ha incluido condiciones de dispersión cuasi-libre en su reaccion.

B.2 Montaje experimental

Los datos utilizados en esta tesis provienen del experimento S393 realizado a finales del verano de 2010 en la instalación GSI Helmholtzzentrum für Schwerionen-Forschung GmbH por la colaboración R3B.

En GSI una fuente de iones produce el haz primario que comienza a acelerarse en el acelerador lineal (UNILAC), tras eso es enviado a un sincrotrón (SIS18) con el fin de llegar a energías más altas, para el experimento S393 el haz primario era de ^{40}Ar alcanzando energías de 490 MeV/u. Al extraer el haz del acelerador, incide sobre un blanco ligero de Berilio de 4011s mg/cm^2, produciendose un cóctel de particulas que pasa a través del separador de fragmentos (FRS) donde las distintas especies son separadas antes de llegar al area experimental de R3B:*Cave C*, donde los detectores están preparados.

La característica principal de este montaje experimental es que es capaz de hacer mediciones de cinemática completa, lo que significa que puede registrar toda la información, incluyendo energía, masa y carga de los isótopos entrantes y los productos de reacción salientes. Los detectores pueden dividirse en tres etapas distintas según su posición y propósito: Detectores de entrada, alrededor del blanco y a la salida.

- **Detectores a la entrada**

  El objetivo de estos detectores es la identificación de los diferentes isótopos que llegan desde el separador de fragmentos. El detector PSP es una placa cuadrada de silicio que se encarga de medir la pérdida

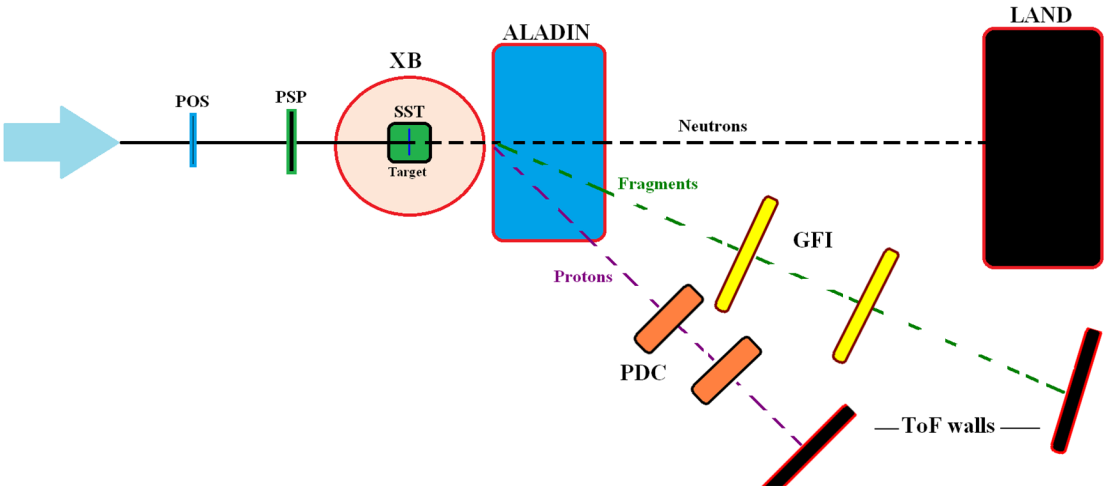

Figure B.1: Esquema simplificado del montaje experimental, la figura 2.5 tiene una representación más detallada. La rama de protones tras el imán ALADIN no se utiliza en este trabajo.

de energía de los nucleos para identificar su carga. Un centelleador en la última sección del FRS (S8) y otro a la entrada del area experimental (POS) se encargan de medir el Tiempo de Vuelo de los isótopos para distinguir la relación de carga/masa. La combinación de ambas mediciones permite identificar los núcleos entrantes. En esta etapa también existe el ROLU que es una combinación de cuatro centelleadores que se pueden ajustar al tamaño requerido del haz, de forma que si una particula produce señal en uno de los centelladores, el evento es descartado.

- **Alrededor del blanco**

  En el experimento se utilizaron tres blancos distintos:
  Carbono (935 mg/cm^2), Plomo (2145 mg/cm^2) y el más relevante para esta tesis, Polietileno (CH_2 con 922 mg/cm^2). Los blancos están fijados a una placa circular que girando, permite escogerlos. Cerca de la misma, hay cuatro detectores de silicio de doble cara (DSSDs), dos delante de los blancos y dos detrás, cuyo propósito es medir el ángulo de interacción de las partículas con el blanco y su ángulo de salida. También se encargan de medir la perdida de energía de los fragmentos salientes para identificar su carga. Alrededor del blanco y los detectores de silicio, está Crystal Ball, un detector esférico consistente en 162 centelleadores de NaI, para detectar los rayos gamma emitidos tras la reacción, también es capaz de medir los protones salientes

de las reacciones (p, 2p).

- **Detectores de salida**

  Tras el blanco hay un gran dipolo magnético llamado ALADIN, que se encarga de curvar las trayectorias de las particulas cargadas que son producto de la reacción. Los fragmentos son dirigidos por el imán a través de un par de detectores de fibras (GFI) para medir dicha trayectoria, al final alcanzan un conjunto de centelladores llamado TFW que se encarga de medir el tiempo de vuelo desde el blanco y la perdida de energia de cada núcleo, permitiendo también identificación de carga. La trayectoria de los neutrones no se curva y continuan en línea recta hasta alcanar un conjunto de centelleadores, LAND, que también mide tiempo de vuelo, energía y la dirección seguida por los neutrones.

B.3 Métodos de análisis

Con el fin de extraer información sobre la estructura de ^{13}Be se ha seguido el método de masa invariante. La idea es la reconstrucción de la energía de los núcleos a partir de la detección del fragmento de ^{12}Be y el neutrón perdido. Sin embargo, si a la energía que llevan se le resta la masa en reposo del fragmento y el neutrón, la resultante es un espectro de energía relativa que da información de las resonancias del núcleo no-ligado ^{13}Be.

$$E_{rel} = \sqrt{M^2_{^{12}Be} + m_n^2 + 2 \cdot m_n M_{^{12}Be} \gamma_n \gamma_{^{12}Be}[1 - \beta_n \beta_{^{12}Be} \cdot cos(\theta_{^{12}Be-n})]} - M_{^{12}Be} - m_n$$

La ecuación muestra que sólo tres parámetros son relevantes; el ángulo entre el fragmento saliente (^{12}Be) y el neutron ($\theta_{^{12}Be-n}$), y la velocidad de cada uno. El procedimiento para obtener dichos parámetros es el siguiente: Del haz entrante a través del FRS debe ser seleccionado el núcleo de ^{14}B, evitando contaminantes de otros isótopos. De los productos de reacción se debe seleccionar la carga Z=4 (Berilio) mediante los silicios DSSDs que hay detrás del blanco. Utilizando el sistema de detectores de cinemática completa es posible separar los fragmentos salientes de reacción según sus masas y de esta forma se debe seleccionar las masas A=12. Una vez el fragmento ha sido aislado debemos escoger los eventos que incluyan un neutron en LAND y por lo tanto el canal de interés estará limpio y podremos medir el ángulo y las velocidades de dichos componentes.

El espectro de energía relativa que hemos calculado muestra un conjunto de picos que pueden ser identificados como resonancias del ^{13}Be.

Para poder fijar sus posiciones y anchuras, estas deben ser ajustadas mediante funciones Breit-Wigner, que son capaces de describir estos estados,

$$\frac{d\sigma}{dE} \sim \frac{\Gamma(E)}{(E_r - E)^2 + \frac{\Gamma(E)^2}{4}}.$$

Donde,

$$\Gamma(E) = 2\gamma^2 P_l(\rho, \eta).$$

La función Breit-Wigner sólo tiene dos parámetros libres para ajustar; la anchura reducida de la resonancia γ y la energía de la resonancia E_r. La función utilizada tiene que introducir la resolución de los detectores.

Al producir el ^{13}Be, se pueblan varias resonancias y por lo tanto el decaimiento del neutron puede poblar distintos estados del ^{12}Be. Para aclarar la estructura del ^{13}Be, el método de la masa invariante no es suficiente, porque el espectro solo muestra la energía entre el fragmento y el neutron, pero no puede distinguir las excitaciones del ^{12}Be. A menos que sólo se haya poblado el estado fundamental del fragmento, la medida debe ser complementada con detección de rayos gamma, sino algunas de las resonancias del ^{13}Be que decaigan a distintos estados del ^{12}Be contribuirán al mismo pico del espectro de energía relativa y se confundirán.

^{12}Be tiene tres estados excitados posibles en el rango de energía de este análisis, por tanto se pueden medir dos rayos gamma a 2.1 y 2.7 MeV. El tercer estado a 2.24 MeV es isomérico y tiene una larga vida-media, por lo que escapará de Crystal Ball antes de emitirse y no puede ser detectado.

Se ha encontrado un rayo gamma a 2.15$\pm$0.02 MeV,que corresponde al rayo gamma de 2.1 MeV. El siguiente paso es encontrar una correlación entre dicho rayo gamma y cualquiera de las resonancias del espectro de energía relativa de ^{12}Be + n. Abriendo una ventana alrededor del rayo gamma en coincidencia con el espectro de energía relativa, el resultado producido está dominado por las cuentas no-correlacionadas presentes. Para poder limpiarlo, se han abierto ventanas de coincidencia a ambos lados del rayo gamma y se ha hecho una media de los espectros de energía relativa que les corresponde, dicha media se ha sustraido de la energía relativa dentro de la ventana de coincidencia con el rayo gamma a 2.1 MeV. El resultado (ver figura B.2) muestra dos divisiones del histograma favorecidos a 0.3 y 0.7 MeV.

Debido a la poca estadística, no es fácil extraer una conclusión de la figura B.2. Parece obvio que no hay correlación con ninguna resonancia a energías altas o medias, puesto que el espectro de energía relativa parece bastante plano por encima de 1 MeV. Las dos divisiones a 0.3 y 0.7 MeV están favorecidas, mientras que la división a 0.5 MeV está suprimida. Por lo tanto, se puede entender que las dos resonancias localizadas en esas divisiones son parcialmente pobladas por alguna resonancia del ^{13}Be que decae

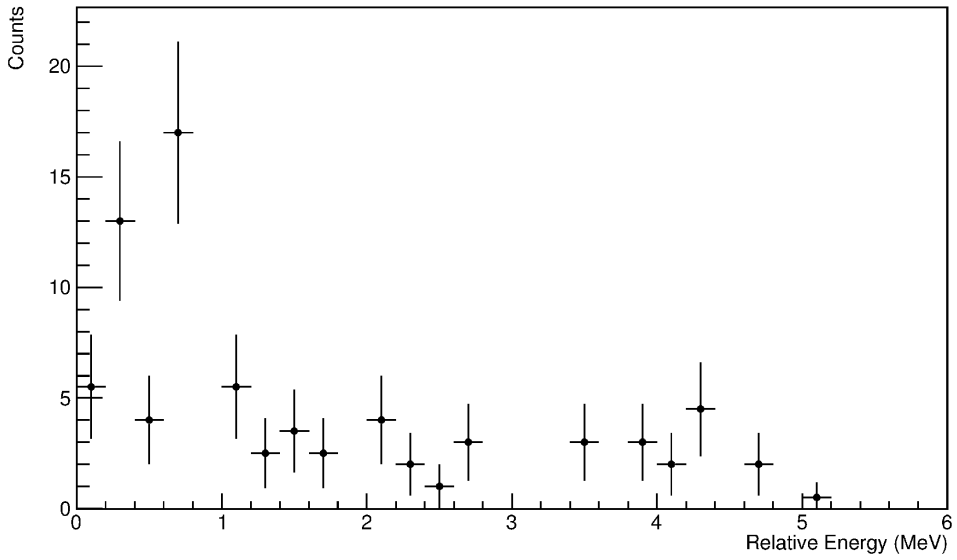

Figure B.2: :Espectro de energía relativa del ^{13}Be tras sustracción de los eventos no correlaccionados con el rayo gamma. Las únicas divisiones que aún están favorecidas son la segunda y la cuarta a 0.3 y 0.7 MeV.

al estado a 2.1 MeV del ^{12}Be. Sin embargo, la segunda división del espectro a 0.5 MeV es normalmente la más alta sin coincidencias y en la figura B.2 es menor que la cuarta división, dado que la cantidad total de cuentas dentro de la ventana de coincidencia con el rayo gamma era mayor que las ventanas a los lados es posible que esta resonancia a baja energia todavía esté descorrelaccionada con el rayo gamma medido.

A pesar de que los requisitos previos para el canal de salida son muy selectivos (^{14}B entrante + ^{12}Be + n), obsevar dos protones salientes de alta energia con condiciones de dispersión cuasi-libre en Crystal Ball, clarificarian la reacción completamente, sin embargo estamos muy limitados por la poca estadísitica. La correlación angular de dispersión cuasi-libre se ha encontrado, aunque el número de cuentas del espectro de energía relativa baja desde 1257 a 487 cuentas en coincidencia con dos protones en Crystal Ball.

B.4 Resultados

El espectro de energía relativa del sistema ^{12}Be + n se ha ajustado a a varias funciones Breit-Wigner usando el metodo de χ^2 con la herramienta MINUIT.

A pesar de que el canal de reacción debe ser bastante limpio tras las condiciones impuestas, es probable que existan eventos en el espectro que sean el resultado de identificaciones inccorrectas, tanto del nucleo de entrada como del fragmento de salida o el neutron. Para tener en cuenta dichos posibles problemas se ha modelizado un fondo no-resonante usando la siguiente ecuación. El modelo tiene una función exponencial y una función Error con tres parametros: $A_{1,2,3}$.

$$E_{NR} = A_1 \cdot e^{-A_2 E} \cdot erf(A_3 E)$$

Sin embargo la inclusión de esta función a los ajustes ha resultado en ajustes más caoticos y no está claro que su inclusión produzca una diferencia significativa en los resultados.

B.4.1 Considerando dos resonancias

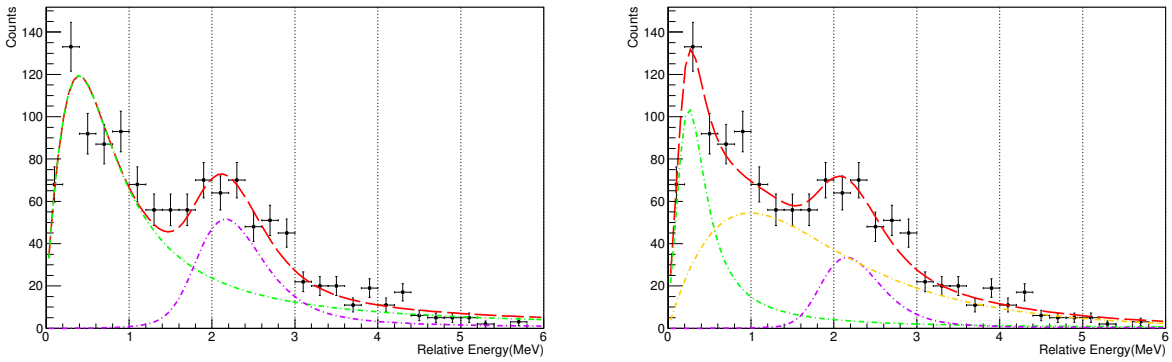

(a) (b)

Figure B.3: Visualización del ajuste considerando dos resonancias con l=0(verde),2(púrpura). (a): Sin considerar fondo no-resonante.(b): Incluyendo fondo no-resonante (amarillo). El resultado de los ajustes se puede ver en la tabla B.1

La mayoría de los estudios previos determinaron sólo dos resonancias en el rango de 0-2.5 MeV para el núcleo de ^{13}Be. Por tanto, aunque la quinta división del histograma muestra un incremento y una diferencia significativa con la división sexta, la opción de sólo dos resonancias debe

		Sin incluir FNR		Incluyendo FNR	
#	l	E_r(MeV)	Γ (MeV)	E_r(MeV)	Γ (MeV)
1	0	0.54(0.04)	1.185(0.002)	0.287(0.038)	0.411(0.008)
2	2	2.18(0.06)	0.381(0.009)	2.18(fijado)	0.176(0.034)
χ^2		49.2588		29.04	
χ^2/N_{df}		2.23903		1.32	

Table B.1: Tabla con los resultados del ajuste considerando dos resonancias con l=0,2. Se incluyen los dos casos con y sin fondo no-resonante. La visualización está en la figura B.3.

ser considerada. Un estado a baja energía con l=0 y otro cerca de 2 MeV con l=2 son considerados inicialmente.

Se ha hecho un ajuste sin el fondo no-resonante pero el resultado (ver la figura B.3(a)) muestra que la primera función Breit-Wigner sola no puede hacer una buena aproximación en su rango. El χ^2/N_{df}= 2.23903 indica la baja calidad de este ajuste.

Para mejorar el ajuste, se ha incluido el fondo no-resonante, para conseguir un resultado con significado fisico ha sido necesario fijar un parametro, la posición de la segunda resonancia E_r=2.18$\pm$0.06 MeV. Esta ha sido escogida porque es la menos afectada por la inclusión del fondo. Los resultados del ajuste están en la tabla B.1, donde se puede ver que el valorχ^2/N_{df}=1.32 ha mejorado significativamente. A pesar de que el fondo da una mejor descripción de la zona entre 0.7-1.7 MeV, este casi ignora el incremento de cuentas de la división de 0.9 MeV, como puede verse en la figura B.3(b), sin embargo la descripción de la parte de baja energía del espectro ha mejorado.

B.4.2 Considerando tres resonancias

Algunas de las publicaciones previas han considerado la inclusión de un estado s o d en la región entre el estado s de baja energía y el estado d alrededor de 2 MeV [46]. Para intentar reproducir el incremento de cuentas de la cuarta y quinta división (0.7-0.9 MeV), se ha introducido otra función Breit-Wigner en el ajuste, en el rango de energías de 0.6-1.2 MeV. Se han considerado los dos momentos orbitales posibles l= 0,2.

El fondo no-resonante se ha incluido también en este caso, a pesar de que parece menos necesario que cuando se han considerado dos resonancias. En estos casos, conduce a anchuras no-fisicas de las resonancias, especialmente en la segunda o bien a que el fondo no-resonante desaparece, siendo tan pequeño que es inapreciable. Para ser capaz de encontrar una solución con significado físico para estos dos casos, se ha fijado el valor de la anchura de la segunda resonancia, usando los valores obtenidos sin el

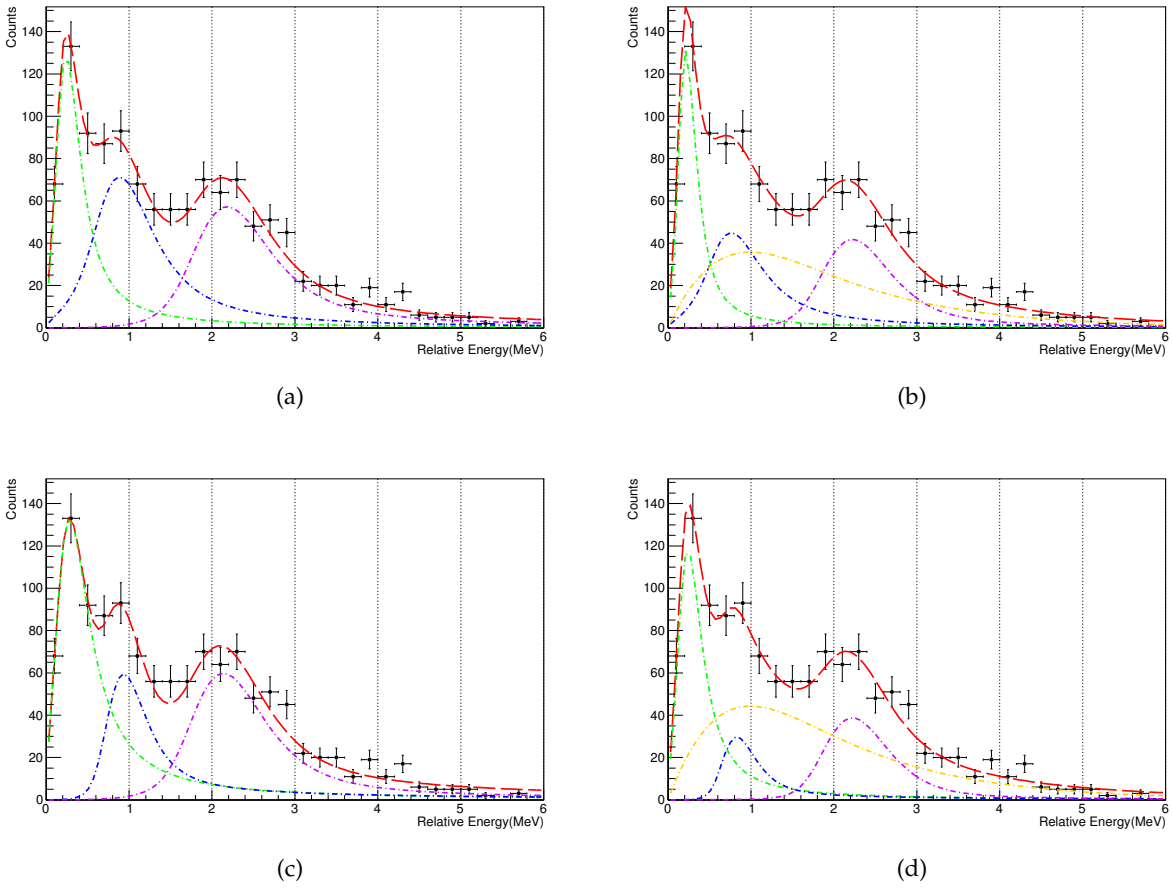

Figure B.4: Visualización del ajuste considerando tres resonancias. Hay resultados con dos opciones, considerando l_2=0,2,así como incluyendo o no el fondo no-resonante. (a): Sin incluir fondo no-resonante y l=0(verde),0(azúl),2(púrpura).(b): Incluyendo un fondo no-resonante (amarillo) y l=0,0,2.(c): Sin incluir fondo no-resonante y l=0,2,2.(d): Incluyendo un fondo no-resonante y l=0,2,2. Los resultados del ajuste pueden encontrarse en la tabla B.2.

fondo no-resonante.

Los resultados obtenidos no han conducido a cambios significativos en la posición de las resonancias, aunque las anchuras si que tienen cambios apreciables.

		Sin incluir FNR		Incluyendo FNR	
#	l	E_r(MeV)	Γ (MeV)	E_r(MeV)	Γ (MeV)
1	0	0.265(0.048)	0.319(0.013)	0.226(0.050)	0.195(0.034)
2	0	0.929(0.080)	0.741(0.029)	0.80(0.16)	0.743(fijado)
3	2	2.209(0.064)	0.635(0.064)	2.240(0.072)	0.383(0.036)
χ^2		24.126		21.89	
χ^2/N_{df}		1.26978		1.15	
#	l	E_r(MeV)	Γ (MeV)	E_r(MeV)	Γ (MeV)
1	0	0.333(0.036)	0.5196(0.0054)	0.262(0.033)	0.312(0.007)
2	2	0.951(0.055)	0.29(0.026)	0.838(0.085)	0.29(fijado)
3	2	2.157(0.058)	0.5845(0.0076)	2.241(0.077)	0.268(0.036)
χ^2		29.9		22.43	
χ^2/N_{df}		1.574		1.180	

Table B.2: Tabla de resultados del ajuste considerando tres resonancias. Hay resultados con las dos opciones, considerando l_2=0,2, así como incluyendo o no un fondo no-resonante. La visualización gráfica del ajuste se puede ver en la figura B.4.

B.4.3 Considerando reacción (p,2p) de dispersión cuasi-libre

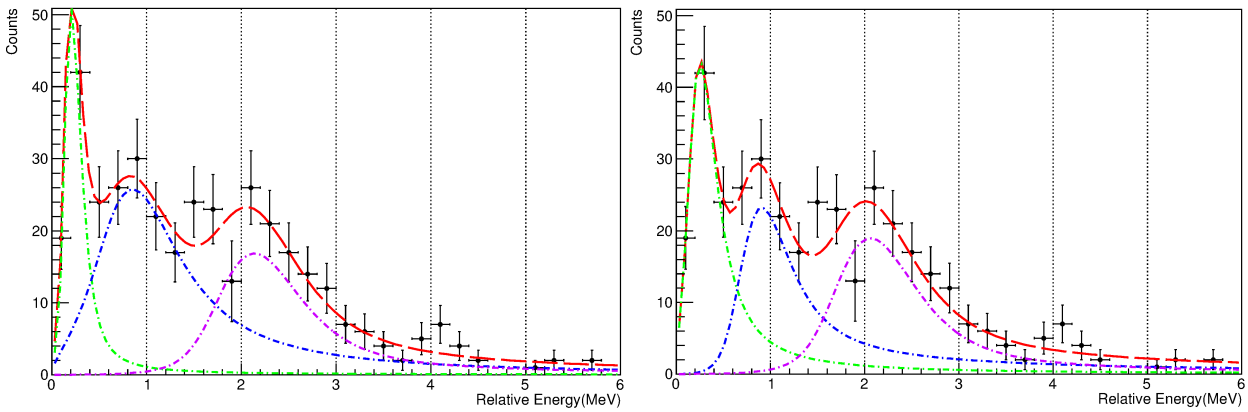

(a) (b)

Figure B.5: Visualización del ajuste considerando tres resonancias con condiciones DCL y considerando las dos opciones de l_2=0,2. (a): En este caso l=0(verde),0(azúl),2(púrpura).(b):En este caso se considera l=0,2,2. Los resultados del ajuste se pueden encontrar en la tabla B.3

A pesar del bajo número de cuentas, el espectro de energía relative del sistema ^{12}Be + neutron imponiendo condiciones de dispersión cuasi-

#	l	E_r(MeV)	Γ (MeV)
1	0	0.214(0.083)	0.12(0.16)
2	0	0.92(0.17)	1.03(0.24)
3	2	2.16(0.21)	0.54(0.20)
χ^2		12.85	
χ^2/N_{df}		0.756	
#	l	E_r(MeV)	Γ (MeV)
1	0	0.279(0.054)	0.322(0.015)
2	2	0.949(0.16)	0.53(0.23)
3	2	2.08(0.17)	0.547(0.087)
χ^2		13.9	
χ^2/N_{df}		0.82	

Table B.3: Tabla de resultados considerando tres resonancias con condiciones DCL. Hay resultados con dos opciones; considerando l_2=0,2. La visualización del ajuste puede encontrarse en la figura B.5.

libre también ha sido estudiado. Las condiciones que se han impuesto en las correlaciones angulares de dos protones en Crystal Ball han sido: 60° $< \Theta_{Op.Angle} <$110° y $\Delta\phi >$110°, conduciendonos a un espectro de de tan solo 385 cuentas.

Hay dos rasgos principales a destacar: La resonancia alrededor de 0.8-0.9 MeV es más evidente, lo que puede ayudar a determinar una anchura más realista para una resonancia en esa posición. También merece la pena mencionar la reducción de cuentas en la décima división a 1.9 MeV, lo que sugiere la posibilidad de dividir la resonancia ancha cerca de 2 MeV en dos resonancias diferentes centradas alrededor de 1.6 MeV y 2.2 MeV. Sin embargo, ninguna de las publicaciones previas han informado acerca de dos resonancias en esa zona. Por lo tanto, a partir de aquí, esta supresión de cuentas será entendido como un fenómeno estadístico y no se considerará otra resonancia en la función de ajuste.

Las barras de error de la décima división se han incrementado (en dos cuentas), esto se ha hecho por varias razones; primero porque los resultados obtenidos estaban demasiado determinados por esa división, debido a que su error está un poco por debajo de los errores de las divisiones vecinas que produce cambios demasiado grandes en los parametros de la segunda y la tercera resonancia. Esto está respaldado también al comparar con el espectro de energía relativa obtenido al requerir dos protones en Crystal Ball pero sin condiciones de dispersión cuasi-libre. El espectro es muy parecido en forma pero tiene alrededor de 100 cuentas menos, en este caso, el peso de esa división es menor y el ajuste produce un buen resultado. Segundo, si consideramos el pequeño tamaño de la división como simplemente un

problema estadísitico, es mejor considerar errores mayores.

En este caso, incluir un fondo no-resonante ha sido probado también pero el resultado ha sido incluso más caótico y es probable que este no sea necesario tras requerir las condiciones de dispersión cuasi-libre.

B.5 Discusión

Para comenzar la discusión es necesario recordar ciertas suposiciones que se han hecho para el análsis.

Los estudios previos del núcleo ^{14}B [86][87] han informado del dominio del componente $2s_{1/2}$ y $2d_{5/2}$ en la configuración de los neutrones de valencia, que debería estar intacto tras la reacción ^{14}B(p,2p)^{13}Be de este experimento. Esta es la razón por la que sólo se han considerado estados s o d como opciones para el análisis.

Las resonancias alrededor de 0.4 MeV y 2 MeV con carácter $1/2^+$ y $5/2^+$ se han encontrado también en varias publicaciones previas, por ello siempre se han considerado dos resonancias con momento angular l=0,2 en esas regiones de energia.

Todos los escenarios presentados en la sección de resultados sólo coinciden en la posición de la última resonancia ∼2.20 MeV. Sin embargo el valor de la primera resonancia oscila desde 0.214 a 0.54 MeV, pero el valor más alto puede descartarse.

Otros estudios han tenido encuenta la posibilidad de la existencia de un estado cerca o por debajo de 1 MeV con $l\neq0$, mientras que otros han informado sobre un estado alrededor de 0.7-0.85 pero hay mucha menos información sobre el.

Asumir una resonancia alrededor de 0.8-0.9 MeV está claramente respaldado tras imponer las condiciones de dispersión cuasi-libre, puesto que un pico en esa zona es mucho más evidente. Las dos últimas publicaciones consideran la posibilidad de un estado en esa región, pero tanto el analisis de perfil de momento realizado por Aksyutina et al [43][45] como el cálculo teórico realizado por Randisi et al [46] no permiten un estado con l_2=0.

Es importante comentar lo que se ha encontrado en el análisis de los rayos gamma. El resultado obtenido es muy distinto respecto al único trabajo publicado que ha medido rayos gamma en coincidencia con el fragmento de ^{12}Be y un neutron, Kondo et al [42]. En nuestros datos sólo hemos encontrado uno de los posibles rayos gamma emitidos desde los estados excitados del ^{12}Be: 2.1 MeV mientras Kondo et al fueron capaces de encontrar también el rayo gamma de 2.7 MeV. Esto es debido a la falta de estadística. Pero esta no es la única diferencia relevante entre las dos medidas. Los autores de [42] informan de que el rayo gamma de 2.1 MeV estaba correlacionado con los eventos a muy baja energía relativa de ∼0.2 MeV o menos, mientras que en este trabajo el mismo rayo gamma se ha cor-

relacionado principalmente con la segunda resonancia cercana a 0.7 MeV, aunque no se puede descartar poblar parcialmente a ambos niveles d energía. El último comentario que debe hacerse sobre la medida de rayos gamma es que el estado a 2.1 MeV del ^{12}Be es un 2^+, por lo tanto este estado debe ser poblado desde un estado s o d.

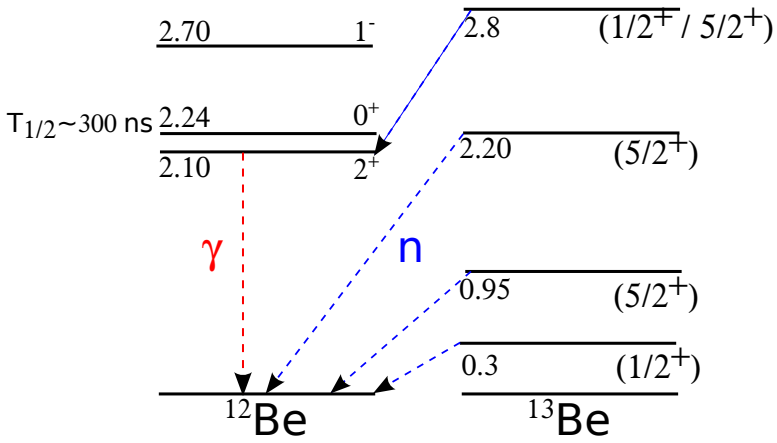

Figure B.6: Estructura del ^{13}Be propuesta por este trabajo. La emisión de neutrones está indicada en azúl, mientras que lós únicos rayos gamma detectados se resaltan en rojo.

De la argumentación previa, la segunda resonancia del espectro de energía relativa puede ser considerado como una mezcla de dos resonancias distintas, una en el valor de la posición obtenido para la resonancia a 0.95 MeV y otra alrededor de la división de 0.7 MeV, encontrada en coincidencia con el rayo gamma de 2.1 MeV, por lo tanto el estado del ^{13}Be estará alrededor de 0.7 + 2.1 $\simeq$ 2.8 MeV. Un estado como este, poblará el estado 2^+ del ^{12}Be emitiendo un neutron desde un estado $1/2^{+,-}$ o $5/2^+$. COmo este estado será >2.7 MeV, tiene permitido energéticamente los otros dos estados excitados del ^{12}Be en 2.24 MeV (0^+) y 2.7 MeV(1^-), sin embargo no hemos encontrados otros picos de energía relativa a $\sim$ 0.1 MeV y $\sim$ 0.6 MeV, ni un rayo gamma a 2.7 MeV. Asumir J^p=5/2 para esta resonancia estaría de acuerdo con esto, puesto que haría que esos estados fuesen casiprohibidos. Sin embargo, algunos de las medidas previas han informado sobre un estado $1/2^+$ cerca de 2.9 MeV.

La figura B.6 representa la estructura sugerida por este trabajo, y respaldada por varios de los resultados de los ajustes previos y esta discusión. El ajuste más cercano a esta conclusión sería el mostrado en la figura B.5(b) cuyos resultados están en la tabla B.3.

B.6 Conclusiones

A continuación, listo las principales conclusiones obtenidas de esta tesis así las mejoras que se van a realizar en el futuro.

- Este trabajo ha encontrado varios posibles estados-resonancia del nucleo no-ligado ^{13}Be, confirmando algunos de los que habian sido medidos previamente: Una resonancia a 0.3 MeV con momento angular orbital l=0 y otra con l=2 cerca de 2.2 MeV. También se ha encontrado una resonancia en la región de 0.7-0.9 MeV, aunque este estado deja un panorama con más opciones abiertas. En la figura B.6 está la estructura propuesta del ^{13}Be. La figura B.5 y la tabla B.3 tiene el mejor ajuste al resultado, considerando l_2=2.

- Esta es la primera vez que un experimento obtiene medidas del núcleo no-ligado ^{13}Be utilizando una reacción (p, 2p) con condiciones de dispersión cuasi-libre.

- Esta es la segunda vez que un experimento estudia ^{13}Be incluyendo medida de rayos gamma. Los resultados obtenidos son muy diferentes a los previos, esta vez, el sistema ^{12}Be + neutrón sólo se ha encontrado en coincidencia con el rayo gamma de 2.1 MeV del ^{12}Be y esta coincidencia muestra una resonancia favorecida a $\sim$ 0.7 MeV.

- La posición de la resonancia alrededor de 0.9 MeV en combinación con el rayo gamma de 2.1 MeV en coincidencia con el pico a 0.7 MeV nos conduce a entender dicha resonancia como una combinación de dos, una a 0.9 y otra a 2.1 MeV + 0.7 MeV $\sim$ 2.8 MeV. El estado a 0.9 MeV sería $5/2^+$ tal y como ha sido establecido en otras publicaciones, mientras que el estado a 2.8 MeV podría ser $1/2$ o $5/2$.

- La baja estadística y la mala resolución de energía relativa,especialmente por encima de 3 MeV, hace imposible extraer conclusiones más definitivas. A pesar de estos problemas, este trabajo ha sido capaz de confirmar resultados previos y proponer nuevas resonancias utilizando la reacción ^{14}B (p,2p)^{13}Be.

- En este caso, no se ha encontrado necesario incluir el fondo no-resonante.

- Actualmente están en desarrollo mejoras en todas las partes del montaje experimental para la futura instalación FAIR. La medida de rayos-gamma será mejorada utilizando el detector CALIFA. Los protones emitidos en la reacción serán encontrados mucho más facilmente utilizando el Silicon Tracker así como CALIFA, mejorando la eficiencia y la resolución energética. NeuLAND se ocupará de los neutrones y ayudará a mejorar la resolución angular, que es la mayor limitación

para la determinación de la energía relativa. La combinación de todos estos detectores con haces radioactivos mucho más intensos facilitará la mejora de los resultados conseguidos.

- Además de la mejora en la resolución, eficiencia e intensidad del haz, que ya han sido planeadas, no hay información teniendo en cuenta la alimentación al otro estado 0^+ isomérico del ^{12}Be a 2.24 MeV. Un experimento capaz de medir un estado de una vida media tan larga tras producir ^{13}Be contribuiria a conocer mejor este nucleo exótico.

Bibliography

[1] Udias Vallina, A. *Historia de la Fisica*. Editorial Sintesis (2004).

[2] Rutherford, E. Phil. Mag., **47**, 284, (1899), 109–163.

[3] Rutherford, E. Phil. Mag., **5**, 26, (1903), 177–187.

[4] Rutherford, E. Phil. Mag., **16**, (1908), 313–317.

[5] Magill, J., Pfenning, G., Dreher, R., and Soti, Z. *Chart of Nuclides*. Nucleonica GmbH (2012).

[6] Geiger, H. and Marsden, E. Phil. Mag., **25**, (1913), 604.

[7] Symons, T. J. M., Viyogi, Y. P., Westfall, G. D., et al. *Observation of New Neutron-Rich Isotopes by Fragmentation of 205-MeV/Nucleon ^{40}Ar ions*. Phys. Rev. Lett., **42**, 1, (1979), 40–43.

[8] Westfall, G. D., Symons, T. J. M., Greiner, D. E., et al. *Production of Neutron-Rich Nuclides by Fragmentation of 212-MeV/u ^{48}Ca*. Phys. Rev. Lett., **43**, 25, (1979), 1859–1862.

[9] Thoennessen, M. *Reaching the limits of nuclear stability*. Reports Prog. Phys., **67**, 7, (2004), 1187–1232. doi:10.1088/0034-4885/67/7/R04. URL http://stacks.iop.org/0034-4885/67/i=7/a=R04?key=crossref.97cd88746048c7f282afda2cdd36205b.

[10] Jonson, B. *Light dripline nuclei*. Phys. Rep., **389**, (2004), 1–59. doi:10.1016/j.physrep.2003.07.004. URL http://linkinghub.elsevier.com/retrieve/pii/S0370157303003259.

[11] Hansen, P. and Tostevin, J. *Direct Reactions with Exotic Nuclei*. Annu. Rev. Nucl. Part. Sci., **53**, 1, (2003), 219–261. doi:10.1146/annurev.nucl.53.041002.110406. URL http://www.annualreviews.org/doi/abs/10.1146/annurev.nucl.53.041002.110406.

[12] Mueller, A. C. and Sherrill, B. M. *Nuclei at the limits of particle stability*. Annu. Rev. Nucl. Part. Sci., **43**, (1993), 529–583.

[13] Simon, H. *Halo nuclei, stepping stones across the drip-lines*. Phys. Scr., **T152**, 014024, (2013), 1–13. doi:10.1088/0031-8949/2013/T152/014024. URL http://stacks.iop.org/1402-4896/2013/i=T152/a=014024?key=crossref.d92b55911899c8393bbcfe80e0798a8b.

[14] Thoennessen, M., Mosby, S., Badger, N., et al. *Observation of a low-lying neutron-unbound state in ^{19}C*. Nucl. Phys. A, **912**, (2013), 1–6. doi:10.1016/j.nuclphysa.2013.05.001. URL http://linkinghub.elsevier.com/retrieve/pii/S0375947413005095.

[15] Wamers, F., Marganiec, J., Aksouh, F., et al. *First observation of the unbound nucleus ^{15}Ne*. Phys. Rev. Lett., **112**, 132502, (2014), 1–5. doi:10.1103/PhysRevLett.112.132502. URL http://journals.aps.org/prl/abstract/10.1103/PhysRevLett.112.132502.

[16] Marganiec, J., Wamers, F., Aksouh, F., et al. *Studies of continuum states in ^{16}Ne using three-body correlation techniques*. Eur. Phys. J. A, **51**, 1, (2015), 1–9. doi:10.1140/epja/i2015-15009-0. URL http://link.springer.com/10.1140/epja/i2015-15009-0.

[17] Caesar, C., Simonis, J., Adachi, T., et al. *Beyond the neutron drip line: The unbound oxygen isotopes ^{25}O and ^{26}O*. Phys. Rev. C, **88**, 034313, (2013), 1–8. doi:10.1103/PhysRevC.88.034313. URL http://link.aps.org/doi/10.1103/PhysRevC.88.034313.

[18] Hoffman, C. R., Baumann, T., Brown, J., et al. *Observation of a two-neutron cascade from a resonance in ^{24}O*. Phys. Rev. C, **83**, 031303, (2011), 1–5. doi:10.1103/PhysRevC.83.031303. URL http://link.aps.org/doi/10.1103/PhysRevC.83.031303.

[19] Tanihata, I., Hamagaki, H., Hashimoto, O., et al. *Measurements of interaction cross sections and radii of He isotopes*. Phys. Lett. B, **160**, 6, (1985), 380–384. doi:10.1016/0370-2693(85)90005-X.

[20] Tanihata, I., Hamagaki, H., Hashimoto, O., et al. *Measurements of Interaction Cross Sections and Nuclear Radii in the Light p-Shell Region*. Phys. Rev. Lett., **55**, 24, (1985), 2676–2679.

[21] Tanihata, I., Kobayashi, T., Yamakawa, O., et al. *Measurement of Interaction Cross Sections using isotope beams of Be and B and isosping dependence of the nuclear radii*. Phys. Lett. B, **206**, 4, (1988), 4–8.

[22] Aumann, T. *Reactions with fast radioactive beams of neutron-rich nuclei*. Eur. Phys. J. A, **26**, 3, (2005), 441–478. doi:10.1140/epja/i2005-10173-4. URL http://www.springerlink.com/index/10.1140/epja/i2005-10173-4.

[23] Hansen, P. and Jonson, B. *The Neutron Halo of Extremely Neutron-Rich Nuclei*. Europhys. Lett., pages 409–414.

[24] Riisager, K. *Halos and related structures*. Phys. Scr., **T152**, 014001, (2013), 1–13. doi:10.1088/0031-8949/2013/T152/014001. URL http://stacks.iop.org/1402-4896/2013/i=T152/a=014001?key=crossref.500f83ab0f70260a97dfff273b9462b7.

[25] Zhukov, M., Danilin, B., Fedorov, D., et al. *Bound state properties of Borromean halo nuclei: ^{6}He and ^{11}Li* . Phys. Rep., **231**, 4, (1993), 151–199. doi:10.1016/0370-1573(93)90141-Y.

[26] Group, I. T. W. Pure Appl. Chem., **83**, (1991), 879.

[27] Williams, J. H., Shepherd, W. G., and Haxby, R. O. *Evidence for the instability of ^{5}He*. Physical Review, **51**, (1937), 888–889. doi:http://dx.doi.org/10.1103/PhysRev.51.888.

[28] Haddock, R. P., Salter, R. M., Zeller, M., Czirr, J. B., and Nygren, D. R. *Measurement of the neutron-neutron s-wave scattering length from the reaccion π^{-}+$d-$ 2n+γ*. Physical Review Letters, **14**, (1965), 318–323. doi:http://dx.doi.org/10.1103/PhysRevLett.14.318.

[29] Tanihata, I., Savajols, H., and Kanungo, R. *Recent experimental progress in nuclear halo structure studies*. Prog. Part. Nucl. Phys., **68**, (2013), 215–313. doi:10.1016/j.ppnp.2012.07.001. URL http://dx.doi.org/10.1016/j.ppnp.2012.07.001.

[30] Baumann, T., Spyrou, A., and Thoennessen, M. Reports Prog. Phys., , 036301, , 1–21. doi:10.1088/0034-4885/75/3/036301.

[31] Johansson, H. T., Aksyutina, Y., Aumann, T., et al. *The unbound isotopes ^{9-10}He*. Nuclear Physics A, **842**, 1-4, (2010), 15–32. doi:10.1016/j.nuclphysa.2010.04.006. URL http://dx.doi.org/10.1016/j.nuclphysa.2010.04.006.

[32] Johansson, H., Aksyutina, Y., Aumann, T., et al. *Three-body correlations in the decay of ^{10}He and ^{13}Li*. Nucl. Phys. A, **847**, 1-2, (2010), 66–88. doi:10.1016/j.nuclphysa.2010.07.002. URL http://linkinghub.elsevier.com/retrieve/pii/S0375947410006044.

[33] Aleksandrov, D. V., Ganza, E. A., Glukhov, Y. A., et al. *Observation ^{13}Be in the reaction $^{14}C(^{7}Li,^{8}B)$*. Sov. J. Nucl. Phys., **37**, (1983), 474–475.

[34] Ostrowski, A. N., Bohlen, H. G., Demyanova, A. S., et al. *Mass spectroscopy of ^{13}Be*. Zeitschrift für Phys. A, **343**, (1992), 489–490.

[35] Korsheninnikov, A., Nikolskii, E., Kobayashi, T., et al. *Spectroscopy of ^{12}Be and ^{13}Be using a ^{12}Be radioactive beam*. Physics Letters B, **343**, (1995), 53–58. doi:10.1016/0370-2693(94)01435-F.

[36] von Oertzen, W., Bohlen, H., Gebauer, B., et al. *Nuclear structure studies of very neutron-rich isotopes of $^{7-10}$He, $^{9-11}$Li and $^{12-14}$Bevia two-body reactions*. Nuclear Physics A, **588**, (1995), 129c–134c. doi:10.1016/0375-9474(95)00111-D.

[37] Belozyorov, A. V., Kalpakchieva, R., Penionzhkevich, Y. E., et al. *Spectroscopy of ^{13}Be*. Nucl. Phys. A, **636**, (1998), 419–426.

[38] Thoennessen, M., Yokoyama, S., and Hansen, P. *First evidence for low lying s-wave strength in ^{13}Be*. Phys. Rev. C, **63**, 014308, (2000), 1–3. doi:10.1103/PhysRevC.63.014308. URL http://link.aps.org/doi/10.1103/PhysRevC.63.014308.

[39] Simon, H., Aumann, T., Borge, M., et al. *Two- and three-body correlations: breakup of halo nuclei*. Nuclear Physics A, **734**, (2004), 323–326. doi:10.1016/j.nuclphysa.2004.01.058.

[40] Lecouey, J. L. *Experimental Studies of Unbound Neutron-Rich Nuclei*. Few-Body-Systems, **34**, (2004), 21–26. doi:10.1007/s00601-004-0029-3. URL http://link.springer.com/10.1007/s00601-004-0029-3.

[41] Simon, H., Meister, M., Aumann, T., et al. *Systematic investigation of the drip-line nuclei ^{11}Li and ^{14}Be and their unbound subsystems ^{10}Li and ^{13}Be*. Nucl. Phys. A, **791**, (2007), 267–302. doi:10.1016/j.nuclphysa.2007.04.021. URL http://linkinghub.elsevier.com/retrieve/pii/S037594740700509X.

[42] Kondo, Y., Nakamura, T., Satou, Y., et al. *Low-lying intruder state of the unbound nucleus ^{13}Be*. Phys. Lett. B, **690**, (2010), 245–249. doi:10.1016/j.physletb.2010.05.031. URL http://linkinghub.elsevier.com/retrieve/pii/S0370269310006234.

[43] Aksyutina, Y., Aumann, T., Boretzky, K., et al. *Structure of the unbound nucleus ^{13}Be: One-neutron knockout reaction data from ^{14}Be analyzed in a holistic approach*. Phys. Rev. C, **87**, 064316, (2013), 1–12. doi:10.1103/PhysRevC.87.064316. URL http://link.aps.org/doi/10.1103/PhysRevC.87.064316.

[44] Guimaraes, V., Kolata, J. J., Bazin, D., et al. *Spectroscopy of ^{13}B,^{14}B via the one-neutron knockout reaction*. Physical Review C, **61**, 064609, (2000), 1–7. doi:10.1103/PhysRevC.61.064609. URL http://arxiv.org/abs/nucl-ex/0001010.

[45] Aksyutina, Y., Aumann, T., Boretzky, K., et al. *Momentum profile analysis in one-neutron knockout from Borromean nuclei*. Phys. Lett. B, **718**, (2013), 1309–1313. doi:10.1016/j.physletb.2012.12.028. URL http://linkinghub.elsevier.com/retrieve/pii/S0370269312012816.

[46] Randisi, G., Leprince, A., Al Falou, H., et al. *Structure of ^{13}Be probed via secondary-beam reactions*. Phys. Rev. C, **89**, 034320, (2014), 1–13. doi:10.1103/PhysRevC.89.034320. URL http://link.aps.org/doi/10.1103/PhysRevC.89.034320.

[47] Bertulani, C. A. *Nuclear Physics in a Nutshell*. Princeton University Press (2007).

[48] Satchler, G. R. *Introduction to Nuclear Reactions*. The Macmillan press LTD (1980).

[49] Wamers, F. *Quasi-free-scattering and one-proton-removal reactions with the proton-dripline nucleus ^{17}ne at relativistic beam energies*. Ph.D. thesis, Technische Universität Darmstadt (2011).

[50] Panin, V. *Fully exclusive measurements of quasi-free single-nucleon knockout reactions in inverse kinematics*. Ph.D. thesis, Technische Universität Darmstadt (2012).

[51] Holl, M. *Quasi-free scattering from relativistic neutron-deficient carbon isotopes*. Ph.D. thesis, Technische Universität Darmstadt (2014).

[52] Díaz, P. *An investigation into quasi-free scattering of light neutron-rich nuclei around N = 14*. Ph.D. thesis, Universidade de Santiago de Compostela (2013).

[53] Aumann, T., Bertulani, C., and Ryckebusch, J. *Quasifree (p,2p) and (p,pn) reactions with unstable nuclei*. Phys. Rev. C, **88**, 064610, (2013), 1–15. doi:10.1103/PhysRevC.88.064610. URL http://link.aps.org/doi/10.1103/PhysRevC.88.064610.

[54] R3B Collaboration, GSI. S393 Experimental Proposal.

[55] *S393 Experiment elog*. URL https://elog.gsi.de/S393/.

[56] *Experimental Analysis elog*. URL https://elog.gsi.de/r3b-analysis/.

[57] *GSI Facility Webpage*. URL https://www.gsi.de/en.htm/.

[58] Barth, W., Bayer, W., Dahl, L., et al. *Upgrade program of the high current heavy ion UNILAC as an injector for FAIR*. Nucl. Instruments Methods Phys. Res. Sect. A Accel. Spectrometers, Detect. Assoc. Equip., **577**,

1-2, (2007), 211–214. doi:10.1016/j.nima.2007.02.054. URL http://linkinghub.elsevier.com/retrieve/pii/S0168900207003518.

[59] Geissel, H., Armbruster, P., Behr, K. H., et al. *The GSI projectile fragment separator (FRS): a versatile magnetic system for relativistic heavy ions*. Nucl. Instruments Methods Phys. Res. Sect. B Beam Interact. with Mater. Atoms, **70**, (1992), 286–2897.

[60] GSI. *Relativistic beams on exotic nuclei: A powerful tool for nuclear structure physics*. GSI-Nachrichten, page GSI.

[61] Altstadt, S. $^{13,14}B$ *(n,*γ*) via coulomb dissociation to constrain the astrophysical r-process.* Ph.D. thesis, Goethe Universität Frankfurt (2014).

[62] Mahata, K., Johansson, H., Paschalis, S., Simon, H., and Aumann, T. *Position reconstruction in large-area scintillating fibre detectors*. Nucl. Instruments Methods Phys. Res. Sect. A Accel. Spectrometers, Detect. Assoc. Equip., **608**, 2, (2009), 331–335. doi:10.1016/j.nima.2009.07.012. URL http://linkinghub.elsevier.com/retrieve/pii/S0168900209014296.

[63] Johansson, H. T. *Hunting tools beyond the driplines, performing large-scale nuclear physics experiments*. Ph.D. thesis, Chalmers University of Technology (2010).

[64] Blaich, T., Elze, T., Emling, H., et al. *A large area detector for high-energy neutrons*. Nucl. Instruments Methods Phys. Res. Sect. A Accel. Spectrometers, Detect. Assoc. Equip., **314**, 1, (1992), 136–154. doi:10.1016/0168-9002(92)90507-Z. URL http://linkinghub.elsevier.com/retrieve/pii/016890029290507Z.

[65] *GSI MBS Webpage*. URL https://www.gsi.de/work/organisation/wissenschaftlich_technologische_abteilungen/experiment_elektronik/datenverarbeitung/datenerfassung/mbs.htm/.

[66] Plag, R. and Johansson, H. T. *Land02 the unofficial guide*. URL http://www-linux.gsi.de/~rplag/land02/.

[67] *ROOT official Webpage*. URL http://root.cern.ch/.

[68] Rossi, D. M. *Investigation of the dipole response of nickel isotopes in the presence of a high-frequency electromagnetic field*. Ph.D. thesis, Johannes Gutenberg-Universität Mainz (2009).

[69] Paschalis, S. *Relativistic one-nucleon removal reactions*. Ph.D. thesis, University of Liverpool (2008).

[70] *SHARP Calculator Webpage*. URL http://www-w2k.gsi.de/frs-setup/Sharp%20Calculator.htm.

[71] Ribeiro Jiménez, G. *Exotic Nuclei and the neutron-dripline limits: S393 Experiment for the R3B collaboration and energy calibration of Crystal Ball*. Master Thesis, Universidad Complutense de Madrid (2011).

[72] Thies, R. *Prototype tests and pilot experiments for the R3B scintillator-based detection systems*. Master Thesis, Chalmers University of Technology (2011).

[73] Lindeberg, S. *Optimisied Use of Detector Systems for Relativistic Radioactive Beams*. Master Thesis in Fundamental Physics, Chalmers University of Technology (2013).

[74] Thies, R. *Across the drip-line and back: examining* ^{16}B. Thesis for Licentiate of Engineering, Chalmers University of Technology (2014).

[75] *ATIMA Webpage*. URL https://web-docs.gsi.de/~weick/atima/.

[76] Plag, R. *Some documentation on Ralf's tracker*. URL http://ralfplag.de/tracker/.

[77] Heine, M. *Measurement of (n, γ)-rates of light neutron-rich nuclei for the r-process nucleosynthesis*. Ph.D. thesis, Technische Universität Darmstadt (2014).

[78] Alpat, B., Ambrosi, G., Balboni, C., et al. *High-precision tracking and charge selection with silicon strip detectors for relativistic ions*. Nucl. Instruments Methods Phys. Res. Sect. A Accel. Spectrometers, Detect. Assoc. Equip., **446**, (2000), 522–535. doi:10.1016/S0168-9002(99)01184-5.

[79] *National Nuclear Data Center Webpage*. URL http://www.nndc.bnl.gov/.

[80] Caesar, C. *Beyond the neutron drip-line: Superheavy oxygen isotopes*. Ph.D. thesis, Technische Universität Darmstadt (2012).

[81] Landau, L. D. and Lifshitz, E. M. *The Classical Theory of Fields*. Spanish Edition, Editorial Reverté (1981).

[82] Shimoura, S., Saito, A., Minemura, T., et al. *Isomeric* 0^+ *state in* ^{12}Be. Phys. Lett. B, **560**, 1-2, (2003), 31–36. doi:10.1016/S0370-2693(03)00341-1. URL http://linkinghub.elsevier.com/retrieve/pii/S0370269303003411.

[83] Johansen, J. G., Bildstein, V., Borge, M. J. G., et al. *Experimental study of bound states in* ^{12}Be *through low-energy* ^{11}Be*(d,p)-transfer reactions*. Phys. Rev. C, **88**, 044619, (2013), 1–10. doi:10.1103/PhysRevC.88.044619. URL http://link.aps.org/doi/10.1103/PhysRevC.88.044619.

[84] Shimoura, S., Ota, S., Demichi, K., et al. *Lifetime of the isomeric 0^+ state in ^{12}Be*. Phys. Lett. B, **654**, 3-4, (2007), 87–91. doi: 10.1016/j.physletb.2007.08.053. URL http://linkinghub.elsevier.com/retrieve/pii/S0370269307010131.

[85] *CERN Minuit Homepage*. URL http://seal.web.cern.ch/seal/snapshot/work-packages/mathlibs/minuit/.

[86] Sauvan, E., Carstoiu, F., Orr, N. a., et al. *One-neutron removal reactions on light neutron-rich nuclei*. Phys. Rev. C - Nucl. Phys., **69**, 044603, (2004), 18–25. doi:10.1103/PhysRevC.69.044603.

[87] Bedoor, S., Wuosmaa, a. H., Lighthall, J. C., et al. *Structure of ^{14}B and the evolution of N=9 single-neutron isotones*. Phys. Rev. C - Nucl. Phys., **88**, 011304, (2013), 1–5. doi:10.1103/PhysRevC.88.011304.

[88] Fortune, H. T. *^{14}Be(g.s.) and single-particle energies in ^{13}Be*. Phys. Rev. C, **90**, 064305, (2014), 1–2. doi:10.1103/PhysRevC.90.064305. URL http://link.aps.org/doi/10.1103/PhysRevC.90.064305.

[89] Fortune, H. T. *Unraveling the structure of ^{13}Be*. Phys. Rev. C, **87**, 014305, (2013), 1–4. doi:10.1103/PhysRevC.87.014305. URL http://link.aps.org/doi/10.1103/PhysRevC.87.014305.